

The evaluation and improvement of the hydrodynamic behaviour of mechanically coupled barges

A novel decommissioning method for oil and gas platforms in the North Sea

R. Feenstra

16 November 2018



© Copyright Allseas Engineering B.V.

This document is property of Allseas and may contain confidential information. It may not be used for any purpose other than for which it is supplied. This document may not be wholly or partly disclosed, copied, duplicated or in any way made use of without prior written approval of Allseas.



THE EVALUATION AND IMPROVEMENT OF THE HYDRODYNAMIC BEHAVIOUR OF MECHANICALLY COUPLED BARGES

A NOVEL DECOMMISSIONING METHOD FOR OIL AND GAS
PLATFORMS IN THE NORTH SEA

by

R. Feenstra

in partial fulfillment of the requirements for the degree of

Master of Science

in Offshore & Dredging Engineering

at the Delft University of Technology,

Supervisors: Prof. Dr. K.A. Riska
Dr. F. Pisanó
M.Sc. C. Keijdener
M.Sc. V. van der Wielen
M.Sc. H. Bailly Guimaraes

PREFACE

Ever since my parents took me with them to watch the ships sail in and out the harbour of our home town I have been interested in the maritime industry. And now, already nine months ago I started my final assignment for the fulfilment of the master Offshore and Dredging Engineering at the Technical University of Delft.

The focus of this final frame of work lies on the decommissioning of offshore structures. I was therefore very happy to write this thesis under the wing of Allseas Engineering, one of the biggest players in this market. Allseas offered me a great working environment, and although I had some stressful times, they always kept me motivated. Special thanks goes out to the colleagues of the tender team, with whom I could always share my problems, every now and then under the pleasure of a cold beverage on the Friday afternoon drink.

I would like to express my gratitude to all the members of my graduation committee, Kaj Riska, Chris Keij-dener, Vincent van der Wielen and Helio Guimaraes, and also Joost den Haan, for supporting and guiding me throughout these nine months. Your helpful contributions were very much appreciated. Vincent I want to thank in particular, by always taking time for me, asking critical questions and having many comments you helped tremendously.

Finally I would like to thank my parents. Thank you for your unwavering support, not only during my thesis, but throughout all my time at the TU Delft.

*R. Feenstra
Delft, November 2018*

ABSTRACT

Allseas' *Pioneering Spirit* is the largest heavy lift vessel in the world. It uses its u-shaped bow to sail around an offshore platform and lift topsides up to $48.000t$ in a single lift. Despite being the largest vessel in the world, platforms exist that are simply too heavy, or too large to fit in between the bows of the vessel. Besides, smaller platforms also offer challenges as the capacity of the lifting beams decreases when the beams are extended towards the platform. This results in a set of platforms that cannot be lifted by the vessel.

To be able to lift this set of platforms, a novel lifting method is proposed based on the twin-barge float-over method, where two separate vessels lift a topsides in a tandem lift. The method offers a solution to the described challenges as the vessels can be moved closer to the platform, resulting in an optimal utilisation of the lifting beam capacity. To improve the hydrodynamic behaviour of the concept, mechanical connections between the barges are incorporated. Allseas is interested in the technical feasibility of this concept in the North Sea. As an effect, the goal of the thesis is to evaluate and improve the hydrodynamic behaviour of mechanically coupled barges. The aim is to assess the motions of the concept using a dynamical model, improve the concept by changing the dimensions and investigate the workability of the concept in the North Sea.

Throughout the decommissioning operation three limits are considered: the impact velocity between the lifting beam and the topsides, the relative pitch between the vessels (leading to stresses in the topsides), and the axial forces in the connection beams. The potential solver ANSYS Aqwa is used to assess the hydrodynamic parameters, after which a Matlab model is created to include the mechanical connections in the model. Since preliminary results showed a standing wave effect between the two vessels for certain frequencies, an additional roll damping of 10% of the critical damping is added and an external damping lid is included.

A sensitivity study is performed to investigate the influence of reconfiguring the dimensions and the gap between the barges on the motions. For an incoming wave spectrum (JONSWAP) with a peak period of $7s$, motions tend to resonate for a certain width over gap ratio. When the peak period is increased to $9s$ this effect becomes invisible and increasing the dimensions results in an improved hydrodynamic behaviour. A final configuration is defined ($L=275$, $B=70$, $T=25m$ and $gap=50m$) to assess the workability of the concept in the North Sea. The linear Matlab model is translated from frequency to time domain to make a probability distribution of the critical limits. The critical incoming wave angle is 120° , where a significant wave height of $1.3m$ with a peak period of $T_p = 9s$ results in an infeasible design due to excessive relative pitch. For other incoming wave angles the workability improves, with the most favourable incoming wave angle being 180° . For the Brent field location in the North Sea, the summer period workability varies between 61% and 88% depending on the incoming wave angle and the orientation of the platform. We can therefore speak of a technical feasible concept that can potentially fortify Allseas' fleet.

GUIDE TO THE READER

In this thesis a novel offshore decommissioning method is presented. Each chapter is part of a step-by-step approach with the goal of evaluating and improving the hydrodynamic behaviour of this method and assessing its technical feasibility.

Chapter I introduces the reader to the offshore decommissioning market and explains the objective of this thesis.

Chapter II is dedicated to the conceptual design of the decommissioning concept and the corresponding critical responses.

Chapter III describes the way of modelling and the derivation of the equations of motion.

Chapter IV discusses the hydrodynamic interaction between the vessels.

Chapter V is a sensitivity study, examining the influence of different parameters on the motions of the vessels. The most optimal dimensions for the concept are chosen.

Chapter VI reviews the limiting sea state of the final configuration. The workability of the concept will be calculated.

Chapter VII gives the final conclusions of the study and commits to giving recommendations for future research.

Information that is considered too detailed to place in the main report can be found in the appendices.

LIST OF FIGURES

1.1	Annual North Sea decommissioning expenditure estimation assuming an oil price of \$70/bbl [3]	4
1.2	Offshore structure installation types in North Sea [30]	5
1.3	Topsides modules build-up [downloaded of the BP website, courtesy of BP]	5
1.4	Different lifting methods for the removal of offshore structures	6
1.5	State of the art single-lift heavy lifting methods	7
1.6	<i>Pioneering Spirit</i> lifting the Brent Delta Platform [downloaded from the Allseas website, courtesy of Allseas]	8
1.7	Lifting configuration of <i>Amazing Grace</i> lifting the Magnus platform [in-house drawing provided by Allseas]	9
1.8	Lifting configuration of <i>Amazing Grace</i> lifting the Troll A platform [in-house drawing provided by Allseas]	10
1.9	Different lifting concepts showing the vessel (in blue) using lifting beams (in red) to lift the topsides structure (in yellow)	11
1.10	Challenges of free floating twin barges lift off system [36]	12
1.11	Coupled barges with hinged linkages [36]	12
2.1	Conceptual design of the starboard vessel	19
2.2	Conceptual design of the connected vessels	19
2.3	Detail of the connection beam	19
2.4	Step-by-step decommissioning operation in birdview. One shows the initial connection of the bow connection beams. Two shows the sail-in around the platform. Three shows the establishing of the aft connections. Four shows the sail-out, the substructure still visible in-situ.	20
2.5	Sail-in and mating phase	20
2.6	Sail-out phase: the aft connection beams fit over the remaining substructure	21
2.7	Drawings of the lifting beams and yokes, note the person in (b) for scale [courtesy of Allseas]	22
2.8	ANSYS FEM model of the Brent Alpha platform showing the vertical displacements in meters	23
2.9	FEM model of the Brent Alpha platform showing von Mises stress kPa as a result of a vertical displacement of the outer legs of $100mm$	24
2.10	Four of the most extreme North Sea platforms	25
2.11	The H851 Barge and The President Hubert Tug Transporting the Tamar Jacket [downloaded free license picture]	26
3.1	Schematic overview of the degrees of freedom	30
3.2	From vessel (a) to free-body diagram (b)	30
3.3	Illustration of connection between time- and frequency domain and wave superposition [16]	32
3.4	Quadrants of the mass-matrix	33
3.5	3D frequency dependent mass-matrix	34
3.6	3D free body diagram of the coupled barges	34
3.7	Elongation of connections	35
4.1	Heave RAO uncoupled barges for beam waves where the right barge first encounters the waves.	41
4.2	Influence of an internal lid on the heave RAO for beam waves.	42
4.3	The effect of an internal lid on the added mass (a), damping (b) and wave force (c) (beam waves) for sway direction. The added mass is normalized by ρ times the volume V , damping is normalized by the ω times ρ times the volume V and the wave force is normalized by ρ , g , the water plane area A_w and the wave amplitude a .	43
4.4	Standing wave in between barges for a wave with $A = 1m$ and $T = 10.3s$, in the environment of ANSYS Aqwa	44
4.5	Sway RAO calculated with Aqwa for the base case, head waves, 10% added roll damping	45

4.6	Heave RAO calculated with Aqwa for the base case, head waves, 10% added roll damping	45
4.7	Damping and added mass for a container vessel next to a quay-side [32]	47
4.8	RAOs OCC experiment vs. HYDROSTAR software for different ϵ . [17]	47
4.9	Sway and heave RAOs calculated with Aqwa, head waves, 10% added roll damping, gap = 50m	48
4.10	The effect of an external lid with different ϵ on the added mass(a), damping(b) and wave force (c) (beam waves) for sway direction for the base case scenario. The added mass is normalized by ρ times the volume V , damping is normalized by the ω times ρ times the volume V and the wave force is normalized by ρ , g , the water plane area A_w and the wave amplitude a	49
4.11	The effect of an external lid with different ϵ on the added mass(a), damping(b) and wave force (c) (beam waves) for heave direction for the base case scenario. The added mass is normalized by ρ times the volume V , damping is normalized by the ω times ρ times the volume V and the wave force is normalized by ρ , g , the water plane area A_w and the wave amplitude a	50
4.12	Heave RAO uncoupled barges for different values of ϵ in beam waves.	51
4.13	Roll RAO uncoupled barges for different values of ϵ in beam waves.	52
4.14	Heave RAO coupled barges for different values of ϵ in beam waves.	53
5.1	Jonswap energy density spectrum for different peak periods T_p and $H_s = 1m$	56
5.2	Wave count Brent Delta annual	57
5.3	Wave count Brent Delta April to September	57
5.4	Ansys Aqwa mesh including damping lid.	58
5.5	MPM vertical lift point motion per wave direction for the coupled barges as function of vessel's width for $T_p = 9s$	60
5.6	MPM vertical lift point motion amplitude per wave direction for the coupled barges as function of vessel's width, distance, length and draught for $T_p = 9s$	61
5.7	MPM relative pitch motion amplitude per wave direction for the coupled barges as function of vessel's width, distance, length and draught for $T_p = 9s$	62
5.8	MPM vertical lift point motion amplitude per wave direction for the coupled barges as function of vessel's width and distance for $T_p = 7s$	63
5.9	MPM vertical lift point motion amplitude per wave direction and as function of vessel's width for $T_p = 9s$	64
5.10	MPM connection force per wave direction and as function of vessel's width and length for $T_p = 9s$	64
5.11	MPM vertical motion lift point as function of barge width and barge distance for different incoming wave angles and $T_p = 9s$	66
5.12	MPM relative pitch as function of barge width and barge distance for different incoming wave angles and $T_p = 9s$	67
6.1	Rayleigh and Weibull probability density functions for different function parameters. The Weibull distribution becomes a Rayleigh distribution for $k = 2$ and $\lambda = \sigma\sqrt{2}$ and reduces to a exponential distribution for $k = 1$	70
6.2	Rayleigh PDF showing the 5% and 95% probability interval	71
6.3	Equal energy discretisation of the RAOs and the wave energy. The figure shows the roll RAO for beam waves together with the energy distribution of a JONSWAP spectrum with $T_p=9s$ and $H_s=2m$	71
6.4	Coupled barges modelled within the environment of Orcaflex	72
6.5	An example of a 100s time simulation of the vertical motion of the lifting point for beam waves with $H_s=5m$ and $T_p=9s$. The red dots indicate the moments that impact takes place. Gap size is taken as 0.1m.	73
6.6	Number of impacts during a three hour beam wave sea state as function of gap size and significant wave height. The number of impacts converges to 900 when the gap size becomes zero. This is a measure for the zero crossing period of the motion.	73
6.7	Impact velocity distribution for $H_s = 1$ (m) and $\alpha = 90^\circ$. Below the QQ-plots are shown for the Rayleigh (left) and Weibull (right) distributions	74
6.8	Impact velocity distribution for $H_s = 1$ (m) and $\alpha = 135^\circ$. Below the QQ-plots are given for the Rayleigh (left) and Weibull (right) distributions	76
6.9	First impact time series for $H_s = 5m$ and beam waves with $T_p = 9s$. The gap limit is decreased to represent the de-ballasting of the vessels	76

6.10	Relative pitch time series, $H_s = 1\text{ m}$, $\alpha = 120^\circ$	78
6.11	Relative pitch distribution and QQ-plots for waves with $H_s = 1\text{ m}$, $T_p = 9\text{ s}$ and an incoming wave angle of $\alpha = 120^\circ$	78
6.12	Time domain simulation of the axial connection force for $H_s = 1\text{ m}$, $T_p = 9\text{ s}$ and $\alpha = 90^\circ$	79
6.13	Filtered extreme values of the time domain simulation of the axial connection force for $H_s = 1\text{ m}$, $T_p = 9\text{ s}$ and $\alpha = 90^\circ$	80
6.14	Axial connection force distribution and QQ-plots for $H_s = 1\text{ (m)}$ and $\alpha = 90^\circ$	80
6.15	Time domain simulation of the axial connection force for $H_s = 1\text{ m}$, $T_p = 9\text{ s}$ and $\alpha = 120^\circ$	81
6.16	Axial connection force distribution and QQ-plots for $H_s = 1\text{ m}$, $T_p = 9\text{ s}$ and $\alpha = 120^\circ$	82
6.17	Summer wave count for the Brent field location and corresponding workabilities for incoming wave angles of $\alpha = 90^\circ$, $\alpha = 120^\circ$, $\alpha = 135^\circ$, $\alpha = 150^\circ$ and $\alpha = 180^\circ$. The values in the workability scatter diagrams represent the rounded percentage of the total number of waves in the corresponding bin.	85
A.1	Simplified model	91
A.2	Elongation of connections	92
A.3	Timeseries roll motion for a wave with an amplitude of 1 m, and a 9 s period	95
A.4	Timeseries heave motion for a wave with an amplitude of 1 m, and a 9 s period	95
A.5	Normalized heave motion for a wave amplitude of 1 m	96
A.6	Normalized roll motion for a wave amplitude of 1 m	96
A.7	$\lambda = 120\text{ m}$	97
A.8	$\lambda = 90\text{ m}$	97
A.9	$\lambda = 240\text{ m}$	97
A.10	Stresses in connections for a wave amplitude of 1 m, a distance of 60 m and a period of 9 s	98
B.1	Vector field illustration [Courtesy of Khan Academy]	100
B.2	Area R, divided in four area's [Courtesy of Khan Academy]	101
B.3	Boundaries of the vessel domain [21]	103
E.1	Schematic side view drawing of the Brent Alpha platform	111

LIST OF TABLES

2.1	Limiting parameters of the operational envelope	22
2.2	Limiting parameters and their magnitude	24
2.3	North Sea Platform Dimensions	25
2.4	Barge dimensions of the Iron lady, H851 and the base case	26
2.5	Limiting parameters and their magnitude	27
2.6	Barge dimensions of the Iron lady, H851 and the base case	27
6.1	Impact velocity distribution parameters as function of significant wave height for beam waves with $T_p = 9s$	75
6.2	Impact velocity distribution parameters as function of the incoming wave angle for $H_s = 1m$ and $T_p = 9s$	75
6.3	Impact velocity distribution parameters as function of significant wave height for beam waves and $T_p = 9s$	77
6.4	Impact velocity distribution parameters as function of the incoming wave angle for $H_s = 1m$ and $T_p = 9s$	77
6.5	Relative pitch distribution parameters as function of incoming wave angle for $H_s = 1m$ and $T_p = 9s$	79
6.6	Axial connection force distribution parameters as function of significant wave height for beam waves with $T_p = 9s$	81
6.7	Connection force distribution parameters as function of incoming wave angle for $H_s = 1m$ and $T_p = 9s$	82
6.8	Values for the impact velocity, the relative pitch and the connection force for different values of ϵ . The values are obtained from a 24-hour simulation with a significant wave height of $H_s = 1m$ and for quartering seas, $\alpha = 135^\circ$	83
6.9	Distribution values of the impact velocity, relative pitch and connection force for quartering seas of $H_s = 1m$ and $H_s = 5m$. The ratio between values is given to give an indication of linearity i.e. if the ratio lies close to five, the limiting parameters are linearly related with the wave height	83
6.10	Limiting significant wave height regarding the impact velocity and relative pitch per incoming wave angle and $T_p = 9s$ based on the Orcaflex time domain simulations and with a probability of failure of one percent	84
7.1	Limiting parameters and their magnitude	88
7.2	Limiting significant wave height regarding the impact velocity and relative pitch per incoming wave angle and $T_p = 9s$ based on the Orcaflex time domain simulations and with a probability of failure of one percent	88
E.1	Brent Alpha static leg forces due to a opposite vertical displacement of the outside legs of $100mm$	111
E.2	Brent Alpha leg forces due to accelerations for different incoming wave angles with $H_s = 1m$ and $T_p = 9s$	111

CONTENTS

List of Figures	ix
List of Tables	xiii
1 Introduction	4
1.1 Decommissioning of oil and gas platforms in the North Sea	4
1.2 Configuration of offshore structures	5
1.3 Decommissioning techniques	6
1.3.1 State of the art single heavy lift methods	7
1.4 Thesis motivation	8
1.4.1 Challenges of a larger single-lift vessel	8
1.4.2 Allseas' novel decommissioning concepts	10
1.4.3 The two-vessel float over method	11
1.5 Thesis objective	13
1.6 Thesis Approach	13
2 Base case design	18
2.1 Design criteria	18
2.2 Conceptual vessel design	18
2.3 Operating envelope	19
2.3.1 Mating and lifting	20
2.3.2 Sail out and offloading	21
2.4 Limiting responses	22
2.4.1 Impact velocity	22
2.4.2 Connection beam forces	22
2.4.3 Topsides forces	22
2.4.4 Overview limits	24
2.5 Dimensions	24
2.5.1 Extreme platforms in the North Sea	25
2.5.2 Base case barge dimensions	25
2.6 Chapter review	26
3 Dynamical model of the coupled barges	30
3.1 Dynamical model	30
3.2 Modelling the vessels	30
3.2.1 The superposition principle	31
3.2.2 Hydrodynamical coupling between the vessels	33
3.2.3 Potential theory	33
3.3 Modelling the connections	34
3.3.1 Derivation of the equations of motion	35
3.3.2 Method of virtual work	36
3.4 Chapter review	37
4 Hydrodynamic interaction	40
4.1 Calculation of the response amplitude operator	40
4.2 Irregular frequencies	41
4.2.1 Internal lid	41
4.3 Additional damping	44
4.3.1 Added roll damping	44
4.3.2 External damping lid	45
4.4 Effect of the damping lid on the uncoupled barges	51

4.5	Effect of the damping lid on the coupled barges.	52
4.6	Discussion external lid	53
4.7	Chapter review	53
5	Parametric sensitivity study	56
5.1	Wave data input.	56
5.2	Barge dimensions.	57
5.2.1	Lifting point	58
5.3	Method of the parametric study.	58
5.4	Vessel response in waves	59
5.5	First stage parametric study: Results	60
5.5.1	First stage parametric study: discussion	65
5.6	Second stage parametric study: results	66
5.6.1	Second stage parametric study: discussion	67
5.7	Chapter review	67
6	Limiting sea state	70
6.1	Probability density functions	70
6.2	Matlab: the frequency domain plus method	71
6.3	Orcaflex.	72
6.4	Impact velocities	73
6.4.1	Number of impacts	73
6.4.2	Impact velocity probability distribution	74
6.4.3	First impact velocity probability distribution	76
6.4.4	Impact velocity section review	77
6.5	Topsides loads	77
6.5.1	Relative pitch probability distribution	78
6.5.2	Topsides loads section review	79
6.6	Connection forces probability distribution	79
6.6.1	Connection forces section review	83
6.7	Damping lid sensitivity	83
6.8	Limiting design wave	83
6.9	Workability	84
6.10	Chapter review	85
7	Conclusion and recommendations	88
7.1	Conclusions.	88
7.2	Recommendations	88
	Bibliography	89
A	Assessment on the influence of nonlinear connection beams	91
A.1	Nonlinearities.	91
A.1.1	Linear case.	92
A.1.2	Nonlinear case	93
A.1.3	Wave pressure integration	93
A.1.4	Damping.	94
A.1.5	Results	94
A.1.6	Discussion	98
B	Potential theory and ANSYS Aqwa	99
B.1	Equations of motion	99
B.2	Green's Theorem	99
B.3	Potential Theory	102
B.3.1	Boundary conditions.	104
B.3.2	Loads	105
B.4	ANSYS Aqwa	106
B.4.1	Meshing	106
C	Metocean data provided by Shell for the Brent Delta location	107

D Iron Lady inclining test	109
E Influence of topsides accelerations on the loads	111
E.1 Topsides acceleration forces	111

LIUBRIFICANTI
5A-77/6/81
FIAT

BRIFICANTE
PER
MISSIONI
SPODRIATE AL CARTELLATO
E O 1190 - I. G. M. - 1990
CONTRATTO N. 770

NETTO KG. 50 LORDO KG. 56
IRANIA 40
HD SAE 3-SAE 40
NA 8/781
FIAT - SEZIONE
LIUBRIFICANTI
oliofiat



SAE 40
LIVELLO MIL.
PER SERVIZI
SUPERIA LE
NETTO KG. 50
FIAT - SEZIONE
oliofiat



OLIO PER MOTORI
A DUE TEMPI
2T
SHELL

ONE

INTRODUCTION

The offshore oil and gas sector is an ever developing market offering business oppertunities to companies worldwide. This chapter starts with an introduction to the decommissioning process of offshore structures in the North Sea. Different methods for removing offshore platforms are explained, identifying the challenges that exist. This results in a thesis motivation, problem statement and thus the main subject of this thesis.

1 | Introduction

1.1. DECOMMISSIONING OF OIL AND GAS PLATFORMS IN THE NORTH SEA

The offshore exploration of oil and gas reserves started in the early 1900s in the United States. First in shallow freshwater lakes and from piers connected to the main land, but soon the exploration expanded to the Gulf of Mexico in 1947, and after that to the North Sea, Brazil, West Africa, the Persian Gulf and South-east Asia [22]. Many of the producing platforms in the North Sea have reached the end of their producing lifetime or will in the coming years. In the past decades the topic of decommissioning offshore oil and gas platforms ascended on the agenda's of governmental institutions. This finally led to the OSPAR (Oslo-Paris) convention in 1992 [30].

The signing of the OSPAR convention resulted in the emerging of the offshore decommissioning market. OSPAR Decision 98/3 prohibits leaving offshore structures wholly or partly in place unless derogation is granted. This derogation applies typically to concrete structures and the footing of large steel jackets weighing more than 10,000t. From the fundamental principle that decommissioning should result in full removal of the installation, derogation is not automatically available and is subject to a detailed assessment and consultation procedure to determine if there are significant reasons to allow the installation (or part thereof) to remain in situ. Furthermore, no derogation is available to steel installations constructed after 9 February 1999 (being the date that Decision 98/3 came into force) [3].

The OSPAR convention is signed only by the following countries: Belgium, Denmark, the European Union, Finland, France, Germany, Iceland, Ireland, the Netherlands, Norway, Portugal, Spain, Sweden and the United Kingdom of Great Britain and Northern Ireland along with Luxembourg and Switzerland, meaning the convention holds around Europe, but not worldwide. This is one of the reasons that the North Sea is the main area of focus for decommissioning contractors. Projected North Sea decommissioning activity estimates vary, with the most conservative estimates predicting the market will require over £30bn of expenditure before 2040 in the UK Continental Shelf (UKCS) alone. As ageing assets reach the end of their economically useful life it is expected that the next five to ten years will see a significant increase in decommissioning activity, increasing up to an estimated annual spend of £2.5bn per annum (Figure 1.1) [29] [24].

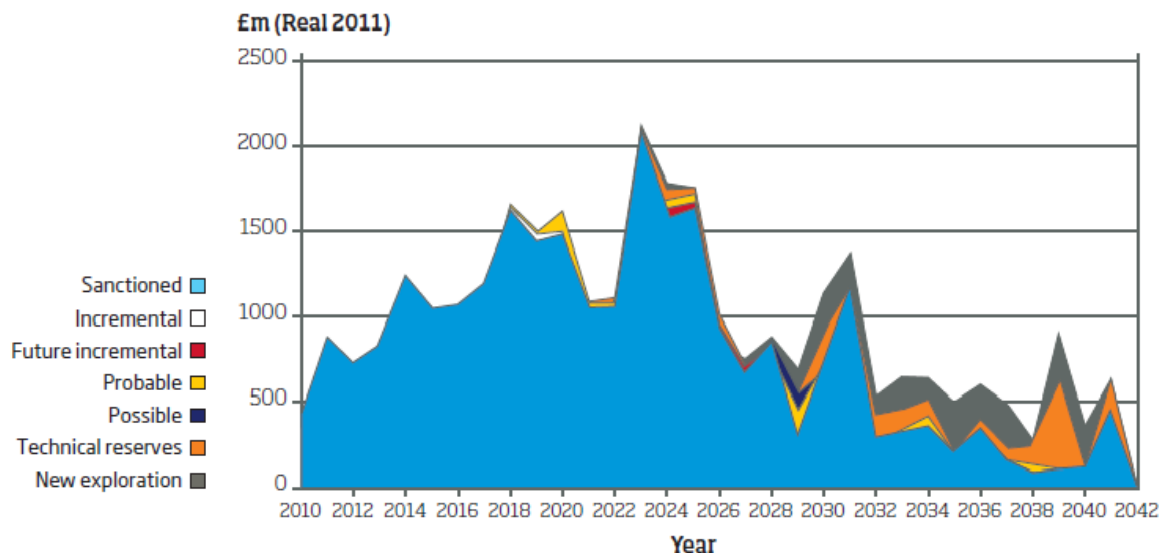


Figure 1.1: Annual North Sea decommissioning expenditure estimation assuming an oil price of \$70/bbl [3]

A more recent study by IHS Markit predicts that global spending on decommissioning will increase from \$2.4bn in 2015 to \$13bn a year by 2040. In the next five years, Europe will account for about 50 percent of global decommissioning spending [19].

1.2. CONFIGURATION OF OFFSHORE STRUCTURES

Offshore structures exist in many sizes and configurations. They consist of a topsides and a substructure which are usually fabricated and installed separately. The general categorization divides the substructures into steel piled jackets, gravity based concrete structures, floating concrete structures and floating steel structures (Figure 1.2). The majority of the structures are steel jackets while the heaviest platforms can be found in the northern North Sea.

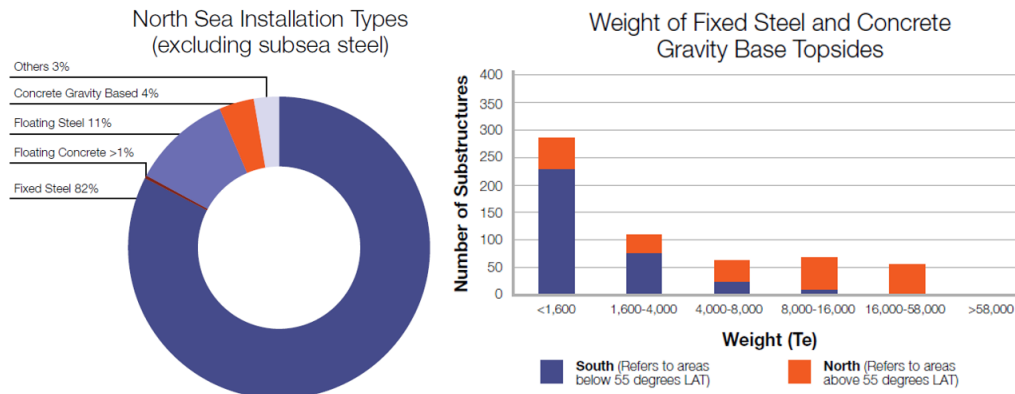


Figure 1.2: Offshore structure installation types in North Sea [30]

The topsides are generally a combination of a modular support frame and topside modules (Figure 1.3). The support frame is placed upon the substructure, where after the different modules can be placed on the support frame.

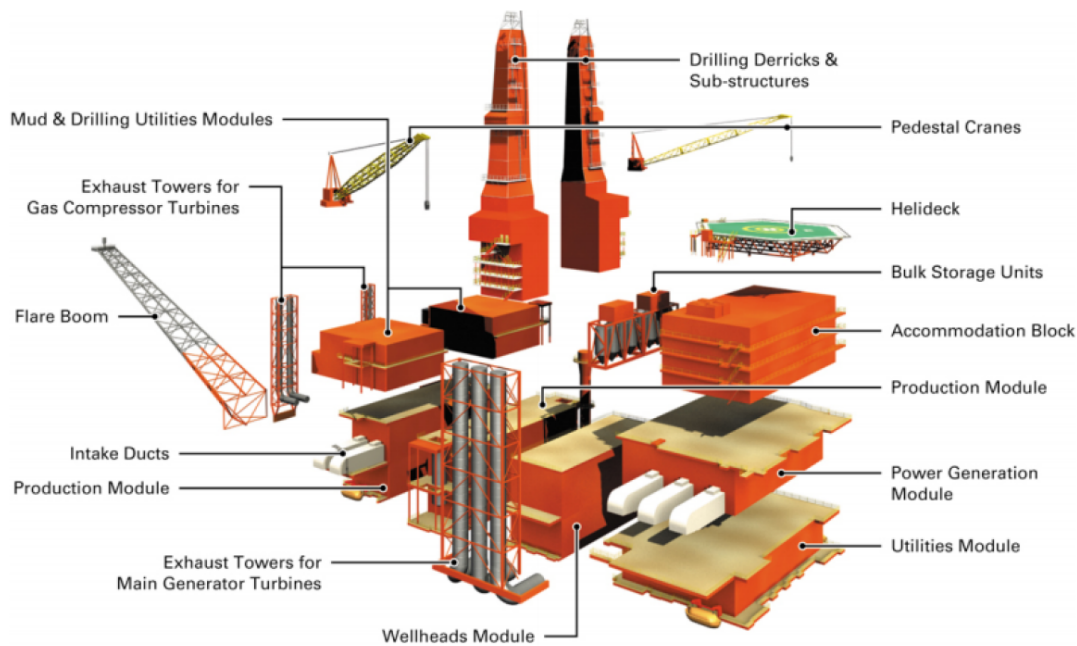


Figure 1.3: Topsides modules build-up [downloaded of the BP website, courtesy of BP]

1.3. DECOMMISSIONING TECHNIQUES

The removal of offshore structures can be performed with different lifting methods. For each structure, depending on size and weight, an optimal decommissioning method exists (Figure 1.4). For the topsides the following lifting methods can be distinguished:

- **The piece-small method** - where modules are cut into small pieces and are collected in containers which are then lifted from the topsides using a crane vessel.
- **The heavy lift method** - where complete modules of the topsides are removed with a large crane vessel.
- **The reverse float-over method** - where the complete topsides is lifted using a barge or multiple barges and is then transported to shore.
- **The single lift method** - the topsides is lifted in a single lift and transported to the decommissioning yard.



(a) Piece small installation of a windturbine [downloaded of the SSP website, courtesy of SSP Technology]



(b) Heavy lift module installation by HMC [downloaded of the HMC website, courtesy of Heerema Marine Contractors]



(c) Float-over installation by Dockwise [downloaded of the Boskalis website, courtesy of Boskalis]



(d) Single lift: *Pioneering Spirit* Lifting Yme [downloaded of the Allseas website, courtesy of Allseas]

Figure 1.4: Different lifting methods for the removal of offshore structures

The removal of the substructure is often a more complicated process. Most of the gravity based structures are too unstable to be safely removed. This is one of the reasons that derogation of the OSPAR convention is often granted to these structures. Steel jackets are easier to remove, often in a single lift using a crane vessel. As derogation does not usually apply to topsides, this will be the most interesting market. The focus in this thesis will therefore lie on the removal of topsides only.

Contractors, such as Allseas, are invited to tender on decommissioning projects. The contractors will assess the best way to remove the platform, taking into account economical, technical, social, environmental and health and safety aspects. After an extensive review of all submitted tenders, a contractor will be chosen to execute the work. One of the biggest drivers for the platform owner ultimately is the price. This price depends mainly on the day rate of the needed vessels times the time needed for the vessels to remove the platform. This means there is a predilection for the single-lift and reverse float-over methods as they need a much smaller time window compared to the piece-small and heavy lift methods. Also the workability of the vessel, i.e. the amount of time per year the vessel is able to perform the activities, plays a big role. Nevertheless a trade off exists for the reason that the day rate of the usually larger single-lift vessels is also higher than the

day rate of smaller lifting vessels [8]. The shorter time window is a motivation for heavy lifting companies to investigate the single-lift approach.

1.3.1. STATE OF THE ART SINGLE HEAVY LIFT METHODS

A novel decommissioning method, recently developed by marine contractor Versabar, uses a multi-body configuration of barges and a lifting frame to lift topsides up to $7.500t$ in a single lift (Figure 1.5a). The Twin-Marine Heavylift is a lifting concept, which uses two $260m$ long and $42m$ wide semi-submersible vessels to lift topsides up to $34.000t$ (Figure 1.5b). A third and similar vessel is used to transport the topsides to shore. The three vessels were ordered by Shandong Twin Marine to be built by the Chinese shipbuilder CIMC Raffles in 2014. It is unclear when and if this concept will be operational.



(a) Versabar lifting solution [downloaded of the Versabar website, courtesy of Versabar]



(b) Twin Marine Heavy Lift concept [downloaded from the heavy lift news website, courtesy of TMHL]

Figure 1.5: State of the art single-lift heavy lifting methods

Another vessel in the single-lift niche is *Pioneering Spirit* (Figure 1.6), owned by Allseas. Measuring 382 meters in length and 124 meters in width it is the biggest vessel in the world. It can lift topsides up to $48.000t$ in a single lift. The vessel has successfully removed the Yme ($13.500t$) and Brent Delta ($24.000t$) platforms and successfully installed the Johan Sverdrup topsides ($22.000t$). The ship uses its catamaran shape to sail around the platform. Sixteen lifting beams equipped with a hydraulic lifting system are then positioned underneath the topsides, after which the topsides is lifted from its substructure in one piece. In sheltered conditions

the topsides is placed on a barge which is used to transport the topsides to the demolition yard. Besides lifting topsides *Pioneering Spirit* is also able to lay pipelines. Additionally a 20.000t jacket lift system is being designed for the vessel, enabling the lifting of complete jackets [1].



Figure 1.6: *Pioneering Spirit* lifting the Brent Delta Platform [downloaded from the Allseas website, courtesy of Allseas]

1.4. THESIS MOTIVATION

Even though Allseas' *Pioneering Spirit* is the largest heavy lifting vessel in the world, the capabilities of the vessel are not unlimited: there are certain topsides that cannot be removed by the vessel. This in combination with the growing decommissioning market has led to the decision to build a bigger single-lift vessel that is capable of lifting the platforms beyond the capacity of *Pioneering Spirit*, named *The Amazing Grace*.

1.4.1. CHALLENGES OF A LARGER SINGLE-LIFT VESSEL

Enlarging the same concept is however not as simple as it may seem. The main reason of this is the fact that offshore platforms greatly differ in size and weight. The major challenges for designing a new bigger vessel can be divided in four parts:

- **Capacity** - the ship should be able to lift the heaviest topsides. To be able to do this a certain amount of buoyancy, ballast and structural strength is needed. The weight of the topsides can be as much as 72.000t.
- **Platform dimensions** - the platform should fit inside the slot of the new vessel. The dimensions of the widest and longest platforms should be taken as criteria for the dimensions of the slot.
- **Width versus weight** - platforms with a small width should also be lifted by the new vessel. This means that the lifting beams have to be extended a certain distance to reach the platform. The combination of this distance and the weight of the platform results in a bending moment in the lifting beams. There are platforms with a weight below the limit of 48.000t that can not be removed by *Pioneering Spirit*

because the lever arm is too large. Building a vessel with an even wider catamaran slot is not going to solve this problem without increasing the dimensions of the lifting beams significantly.

- **Airgap** - the airgap is defined as the distance between the water surface and the lowest deck of the topsides. For certain platforms this distance is rather small due to mild weather conditions. Platforms located in areas with rough weather conditions, like the northern North Sea, usually have a larger airgap. In the first case the ship including the lifting beams should still be able to fit underneath the platform when fully ballasted. In the latter case this means that the ship needs enough buoyancy to lift the topsides, even at high airgaps.

Figures 1.7 and 1.8 show the potential lifting configurations of *The Amazing Grace* for the Magnus and Troll A platforms. It can be seen that different platforms require different lifting configurations. For the Magnus platform the lifting beams have to be extended eight meters, while for the Troll A platform this distance is almost 26m. Besides that, the Troll A platform requires a slot length of at least 155m.

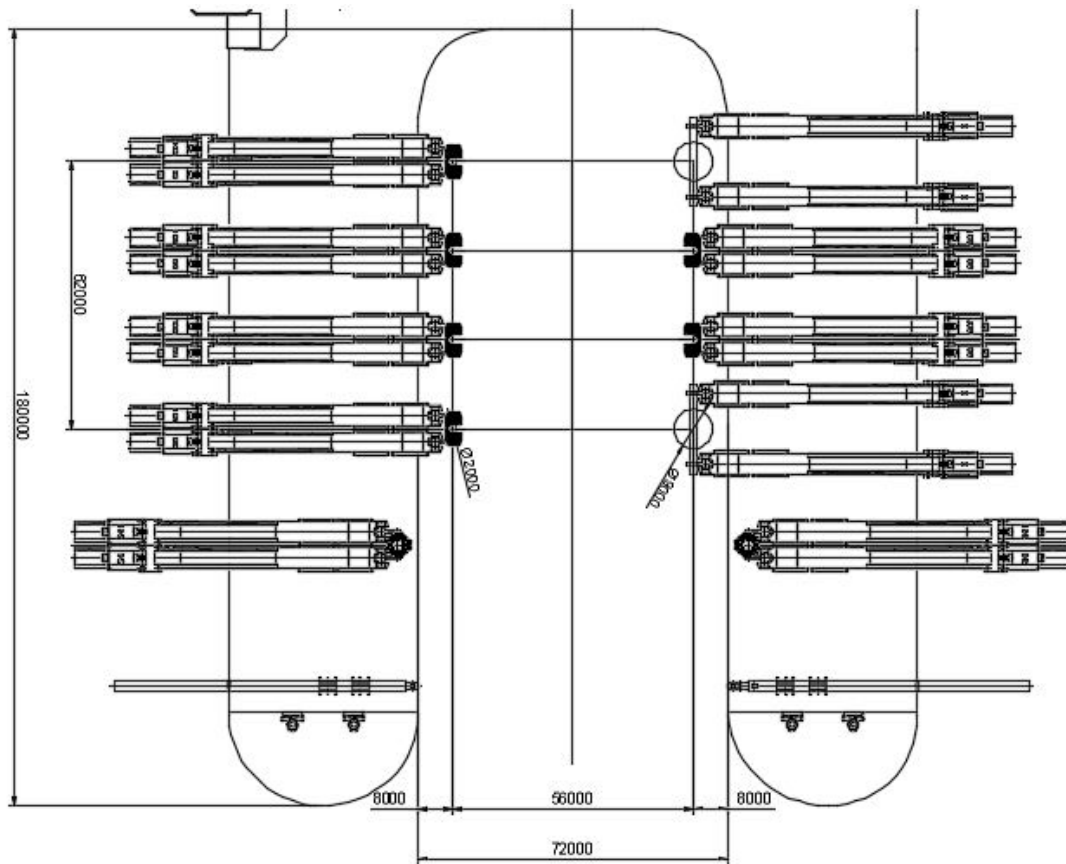


Figure 1.7: Lifting configuration of *Amazing Grace* lifting the Magnus platform [in-house drawing provided by Allseas]

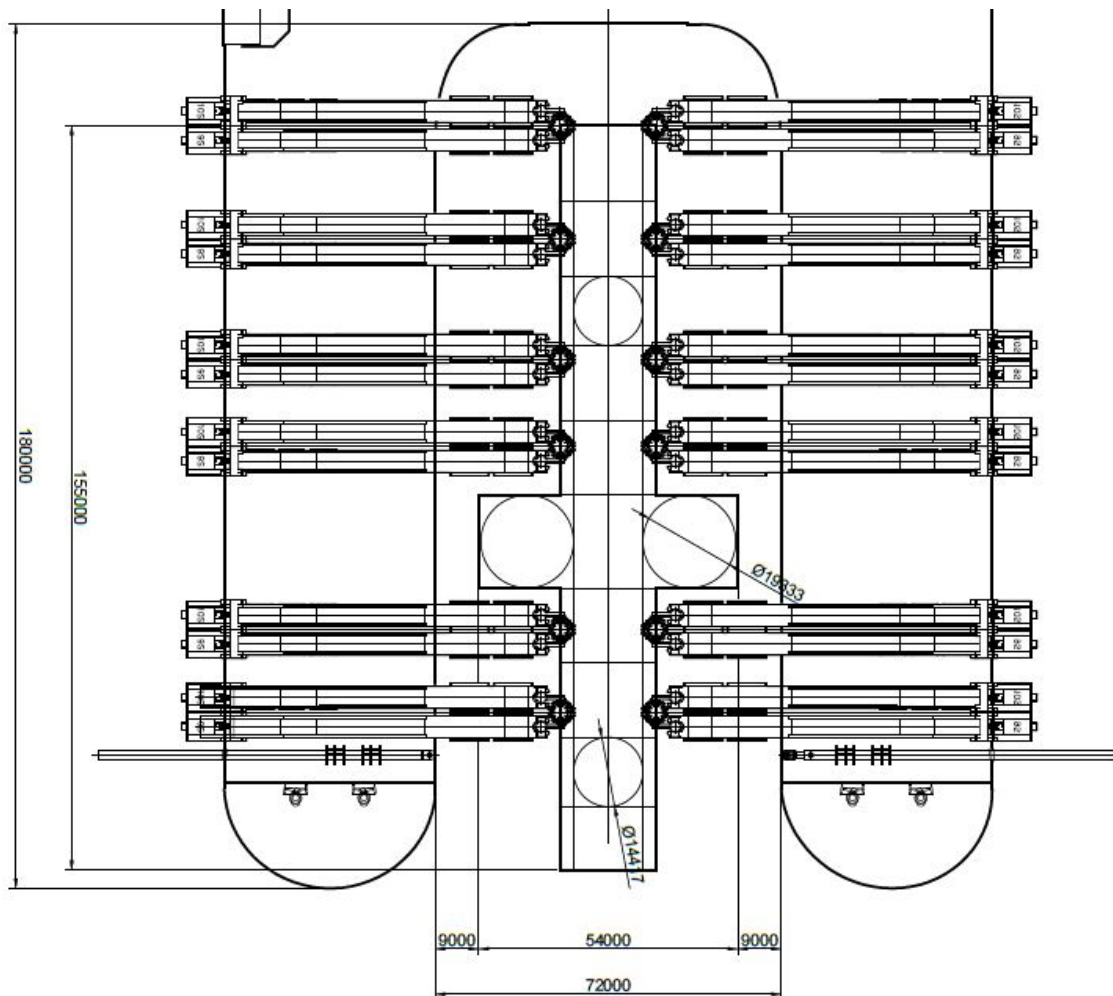


Figure 1.8: Lifting configuration of *Amazing Grace* lifting the Troll A platform [in-house drawing provided by Allseas]

Pioneering Spirit is designed to lift platforms with an airgap between 14 and 33 meters. Many platforms exist with airgaps smaller than this fourteen meters. Additionally, parameters such as maximum water depth and canal or harbour dimensions will bound the geographical position of the vessel. In-house research performed by Allseas concludes that the trade-off between all these parameters makes it impractical or even impossible to design a single vessel that is able to lift all these different platforms.

The design criteria for a new vessel are therefore split up in two categories. The first includes the platforms located in moderate to heavy environmental conditions such as the North Sea. Platforms with a big airgap, heavy topsides and large dimensions. The second category focuses on mild environmental conditions and swell. These platforms typically have small airgaps. With the first category being the most interesting, Allseas decided to design a new vessel that can operate in the North Sea.

1.4.2. ALLSEAS' NOVEL DECOMMISSIONING CONCEPTS

At Allseas several different approaches for large platform decommissioning are under investigation (Figure 1.9). There are the semi-sub and forklift concepts, which have already been found infeasible by an in-house study. The float-over concept is only applicable for structures that have been installed using the same method. A promising concept that has not been investigated in great detail yet is the float-over method using two separate vessels such as the Twin Marine Heavy Lift concept shown in 1.5b or the Aasta Hansteen float-over shown in 1.4c. Allseas is interested in the technical feasibility of this concept and is keen on knowing whether it could be an alternative for the *Amazing Grace*.

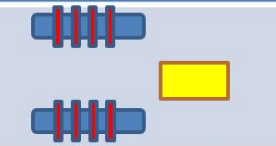
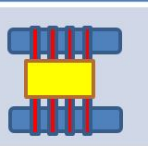
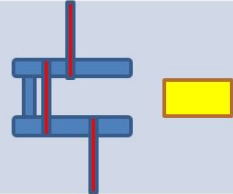
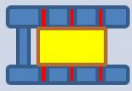
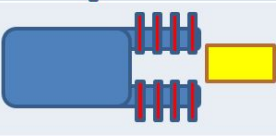
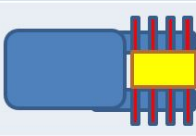
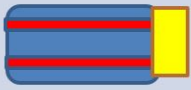
Concept	Sketch	
Two vessels		
Float over		
Semi-sub		
<i>Pioneering Spirit</i> concept		
Forklift		

Figure 1.9: Different lifting concepts showing the vessel (in blue) using lifting beams (in red) to lift the topsides structure (in yellow)

The two vessel float-over method potentially takes away the challenge of lifting platforms with different widths as the distance between the vessels is simply not fixed. The mobility of the concept is increased and the vessels can additionally be used independently in different offshore operations. Also the method is already being used to install the Aasta Hansteen topsides (Figure 1.4c).

1.4.3. THE TWO-VESSEL FLOAT OVER METHOD

The main challenge of the two vessel float-over method, is the vulnerability to the environmental conditions. The relative motions of the vessels can result in large stresses in the topsides. The asymmetric roll and the relative heave and pitch motion of the vessels can quickly result in a infeasible design, even for calm sea states. The interaction between wave excitation and topsides loading can result in rotating barges drifting away from each other (Figure 1.10).

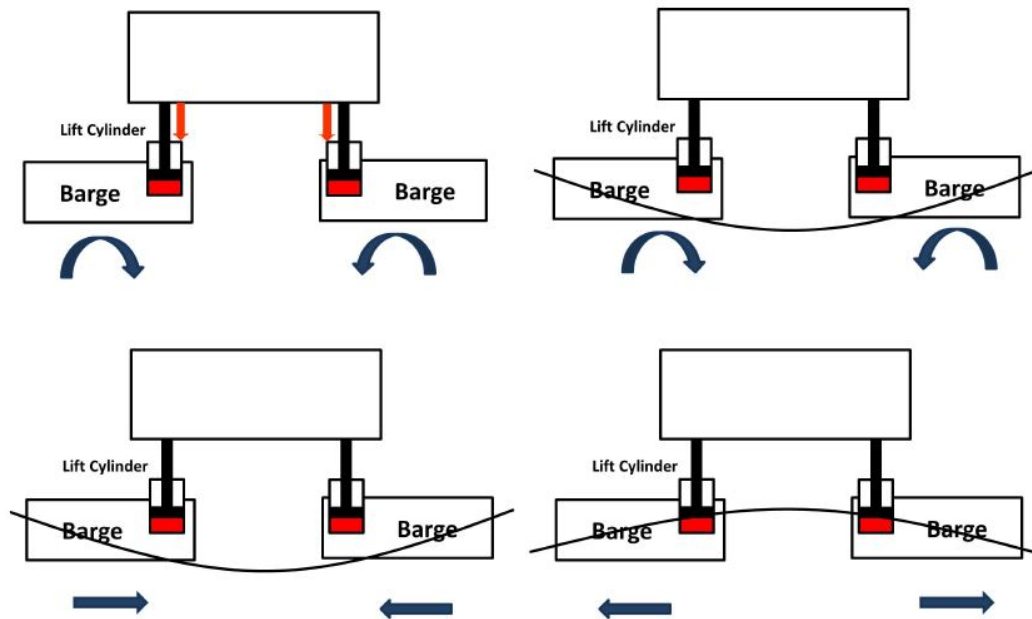


Figure 1.10: Challenges of free floating twin barges lift off system [36]

Mechanically coupling the barges to impede these relative motions offers a potential solution [36]. In order to eliminate the excessive sway and relative roll, hinged linkages are used to connect the barges (Figure 1.11). In this configuration the relative heave and pitch motion are not prohibited. The fact that the connections are hinged theoretically means that only axial forces exist in the connections. This reduces the necessary stiffness of the beams and therefore the amount of steel needed.

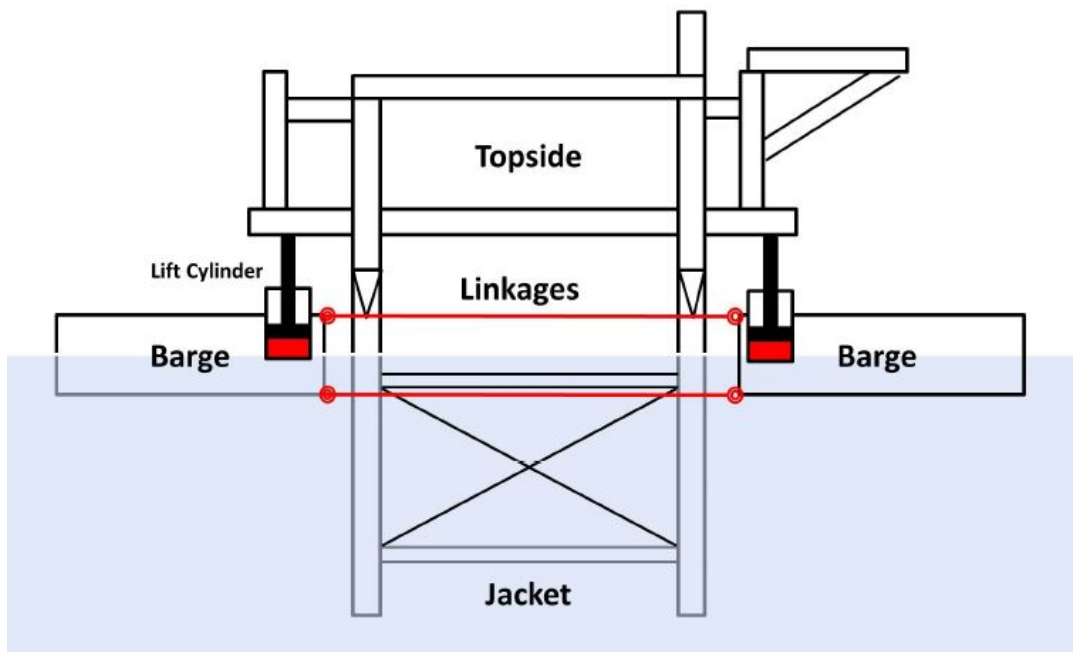


Figure 1.11: Coupled barges with hinged linkages [36]

The linkages between the barges do significantly reduce the roll motion when compared to two free floating barges. Even more important, the peak response is shifted to lower periods and consequently out of the wave

period spectrum for the chosen barge and linkage dimensions [36] [26]. This excludes the possibility of roll resonant responses throughout the operation.

It is expected that different barge dimensions greatly influence the performance of the connected barges concept. The system should be able to lift topsides from different dimensions, meaning that the distance between the barges can vary. The altering distance between the barges can result in different natural frequencies and variable coupled motions. Further improvement of the concept can be achieved by analysing the influence of these dimensions.

1.5. THESIS OBJECTIVE

A decommissioning concept using two separate vessels can potentially offer a solution to the challenges that arise when one wants to decommission different offshore platforms in the North Sea. The method has already been proved to work when installing platforms in mild and sheltered sea states. The motions of the vessel can be decreased by connecting the barges mechanically [36]. The implementation of these mechanical connections is regarded as critical to improve the twin-barge decommissioning concept for the conditions of the North Sea. Nevertheless the vessel motions depend on more parameters than the stiffness of the connections. Different barge dimensions and a variable gap between the vessels will have influence on the motions as well.

As an effect, the goal of this thesis will be:

The evaluation and improvement of the hydrodynamical behaviour of mechanically coupled barges.

The ambition is to study the sensitivity of the barge dimensions on the hydrodynamical performance and use that information to increase the workability of the existing two-vessel float-over method. The aim is to obtain the limiting responses of the concept and calculate the limiting sea state at which these responses will occur.

1.6. THESIS APPROACH

The first step in reaching the goal is defining the conceptual design of the tandem-barge float-over system. For each operational phase the limiting parameters will be determined. The base case dimensions of the barges will be established based on the dimensions of similar vessels and offshore oil and gas platforms in the North Sea.

The next step is creating a dynamical model in Matlab which can evaluate the motions of the base case barge in frequency domain. To construct the equations of motion the hydrodynamic parameters need to be calculated using a diffraction radiation solver. Different computer programs are suitable to do so. One of them is ANSYS Aqwa, a software package that is widely used commercially which is available via a TU Delft license. Therefore this program will be used to determine the hydrodynamic parameters. Additionally the implementation of the connections between the barges will be accounted for. The wave input needed to calculate the motions will be defined so that it represents the rough conditions of the northern North Sea.

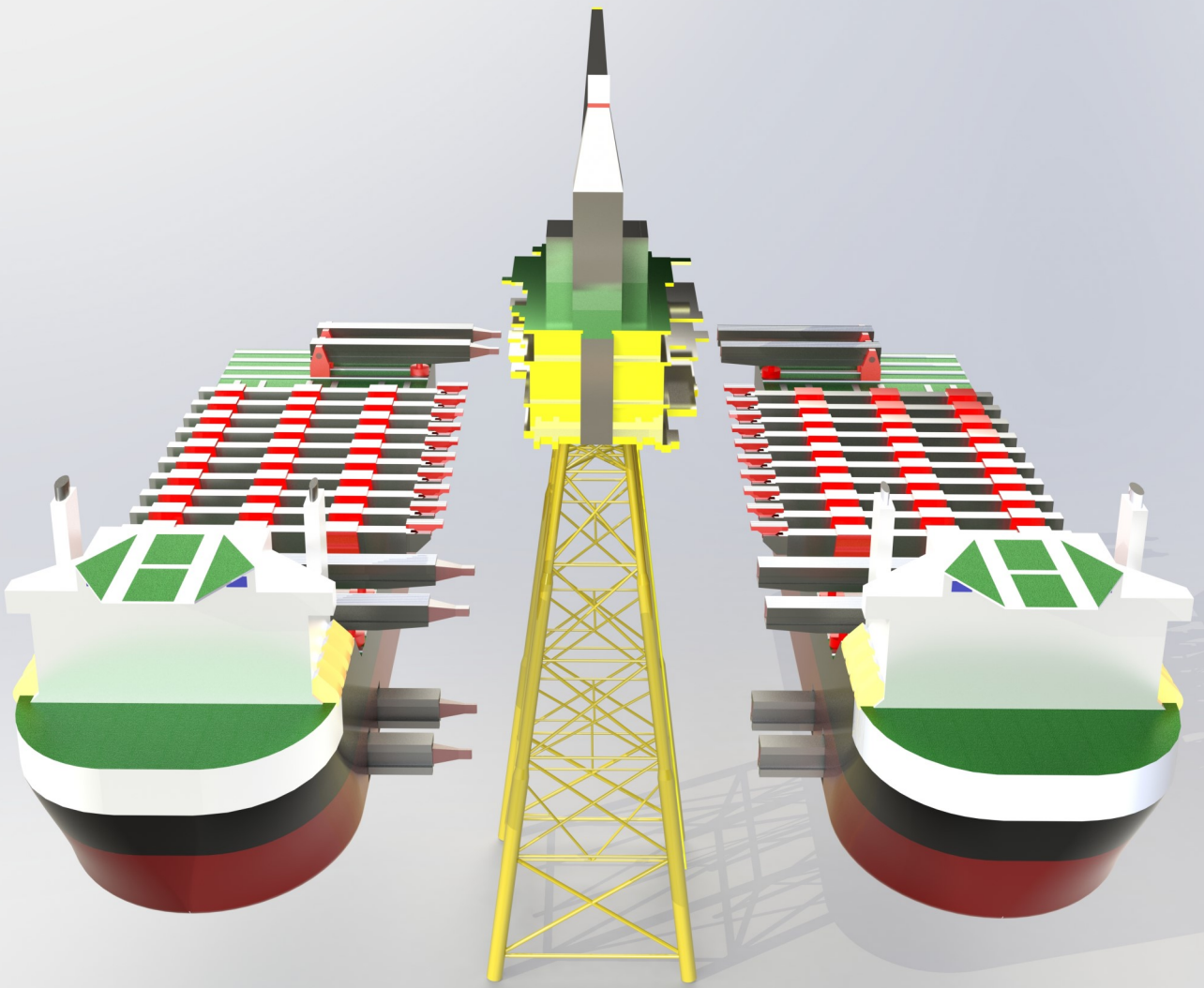
The following objective is the development of a tool that communicates between ANSYS Aqwa and Matlab. This tool will use the potential solving program to calculate the hydrodynamic parameters for different barge dimensions. These parameters are used as input for the dynamical model in Matlab. For each configuration the Matlab software will assess the dynamic behaviour. In completion the output of all different configurations will be compared to come up with the most optimal design parameters. Moreover, this way of modelling makes it possible to say something about the sensitivity of changing the different dimensions with respect to the response of the vessel. This will result in a better understanding of the multi-body dynamics twin-barge decommissioning concept.

Finally the limiting sea state will be evaluated for the final concept. Using time domain calculations a probability distribution can be made of the extreme values of the responses. These extreme values are then compared to the critical responses to say something about the effectiveness of the design and the workability. The results will be validated using Orcaflex, a state-of-the-art software package that can simulate vessel motions.

The approach can be summarized in a ten-step plan.

Approach:

1. Define a base case configuration
2. Define the critical response
3. Build a 3D Matlab model of the multi-body configuration and implement the connections
4. Acquire the added mass and damping matrices using ANSYS Aqwa
5. Define the wave spectrum
6. Design a tool that combines the potential solver and the Matlab model to calculate the responses for many different configurations
7. Post process the data
8. Come up with an optimal design based on the results
9. Find critical sea state and calculate the workability
10. Write the report.



T W O

C O N C E P T D E S I G N

In this chapter the conceptual base case design of the vessels is presented and the operating envelope of the vessels is discussed. The operational phases concerning a decommissioning project are explained. In more detail the implementing of the connection beams during these phases is illustrated. Additionally the operational limits are selected. After this the base case vessel dimensions are defined, based on the dimensions of some of the largest barges available. Additionally the dimensions of the most extreme platforms in the North Sea are used to define the depth and the necessary gap between the vessels.

2 | Base case design

2.1. DESIGN CRITERIA

The design proposed by Mathios[26] and Wang[36] consists of two barges and four connection beams, two at the aft and two at the bow. This design will at first be adopted. However, in order to adjust the vessels to different topsides and make the removal of topsides more practical, some additional design criteria will be set up.

First of all the vessels have to be connected mechanically to prevent the relative sway, yaw and roll motion, as is the case in the design of Wang and Mathios. The beams will be connected by hinges to the vessels in order to reduce the amount of stiffness needed to prevent failure of the connection beams. To be able to sail around the platform, it is evident that the connections require to be disconnectable. Furthermore, when the platform is lifted by the vessels, the vessels should be able to sail away with the connections in place. It is not entirely clear how Mathios and Wang have implemented this criteria in their design.

To keep the vessels in place throughout the operation a mooring or dynamic positioning system is required. Due to increased mobility, the choice is made for the latter. It is expected that a DP3 system is appropriate, as it is used by the *Pioneering Spirit* as well. Also the number of lifting beams is based on the *Pioneering Spirit* (8 per hull), but also on the concept design of the *Amazing Grace* where the number of beams is increased to twelve lifting beams per hull. This results in the following design criteria.

Design criteria:

- The vessels are connected mechanically to prevent the relative sway, yaw and roll motion.
- The connection beams and the vessels are connected via hinges.
- The vessels can be disconnected.
- The connection beams should not interfere with the substructure when sailing out.
- To maintain position, the vessels are equipped with a DP3 system.
- Each vessel is equipped with ten lifting beams.

It has to be clarified that the goal of this thesis is not to design a decommissioning concept vessel on a detailed level. The focus lies on the technical feasibility and the hydrodynamic performance of the concept. The conceptual design is made to illustrate the operational steps involved with the decommissioning of an offshore platform. When found technically feasible, the design can still be changed on a detailed level. There can be thought of a different implementation of the connections, or a different lifting beam layout. These choices do however not influence the hydrodynamic performance of the concept. In the following section the conceptual design is discussed.

2.2. CONCEPTUAL VESSEL DESIGN

Figure 2.1 shows an illustration of the starboard vessel. It is outfitted with six connection beams, of which two are installed below the water level, and ten lifting beams, placed on sliders on the deck. The lifting beams can be moved around the deck on these sliders, making it possible to adjust the lifting configuration for different topsides.

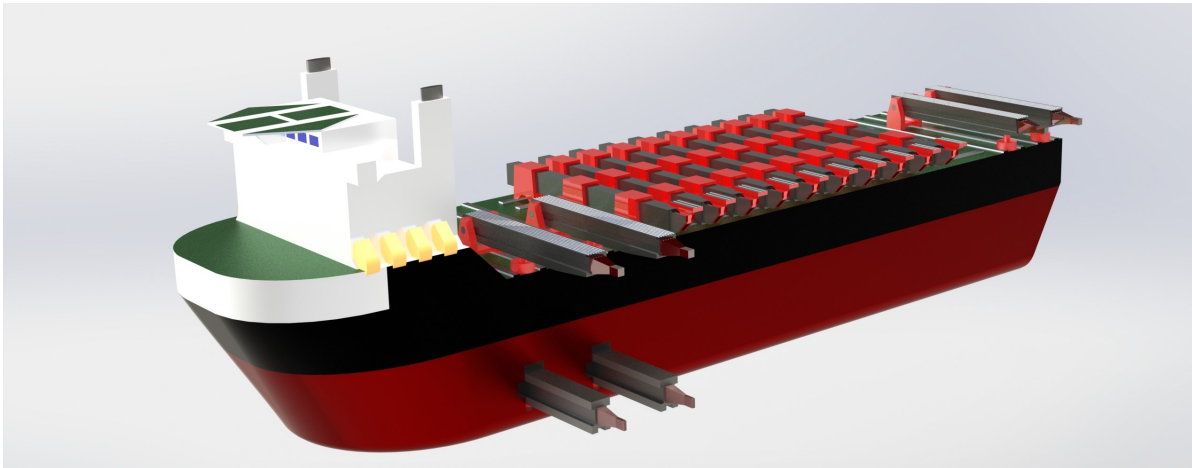


Figure 2.1: Conceptual design of the starboard vessel

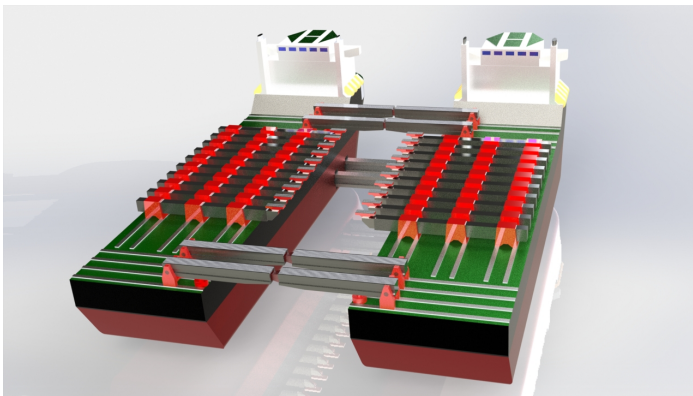


Figure 2.2: Conceptual design of the connected vessels

Connected vessels

Figure 2.2 shows an illustration of the two connected vessels. The connection beams are outfitted as male-female, meaning that the connection beams of the starboard vessel fit into the connection beams of the portside vessel. Once the connection beams are fitted, a hydraulic pin will insure the connection of the beams. Additionally the illustration shows the lifting beam sliders on the deck.

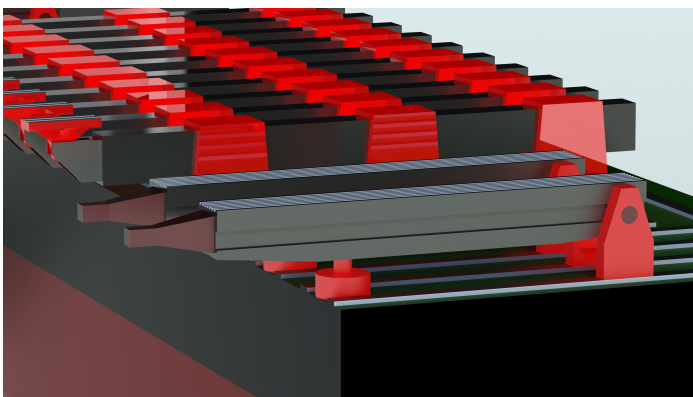


Figure 2.3: Detail of the connection beam

Connection beams

Figure 2.3 shows an illustration of the aft connection beams. The first support structure is a hinged support placed on a slider rail. The second support, illustrated as a red cylinder below the lifting beam, represents a hydraulic cylinder. When the beams are connected, the cylinder can be lowered, meaning only the hinged supports remain. This hydraulic-hinged support combination also exists in the underwater connections.

2.3. OPERATING ENVELOPE

The operating envelope is defined as a limited range of parameters in which operations will result in safe and acceptable equipment performance. These parameters are needed to say something about the workability of the vessel. It is of great interest to the companies involved in the operation to know until which environmental condition the operation can still be performed. The decommissioning operation consists of different phases. For each phase different critical loads may apply. Therefore first these operations will be explained step by step, pointing out where the limiting parameters will occur (Figure 2.4).

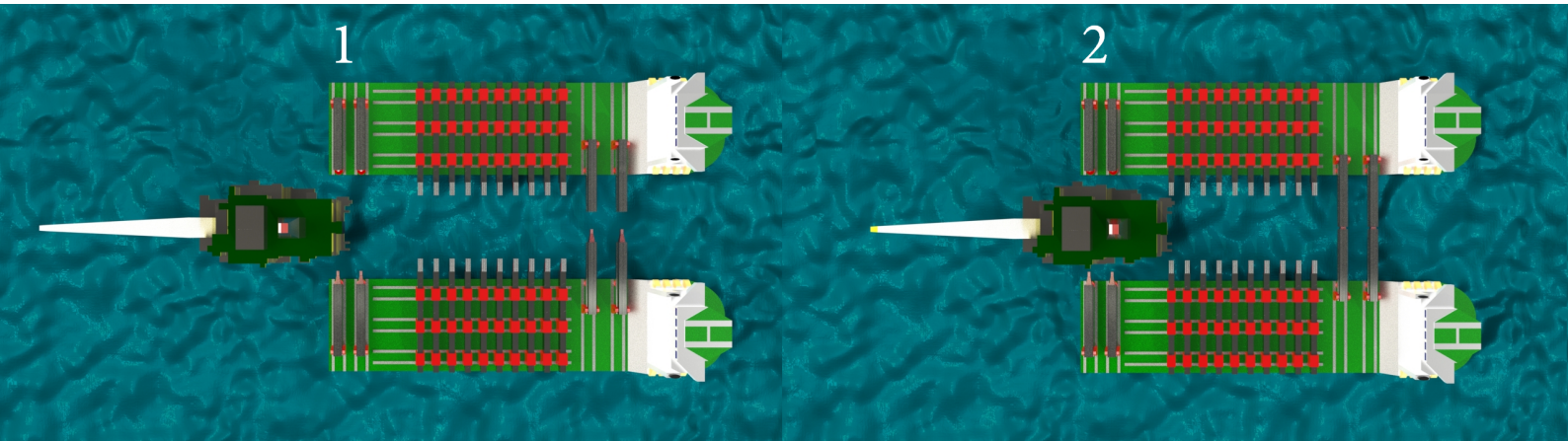


Figure 2.4: Step-by-step decommissioning operation in birdview. One shows the initial connection of the bow connection beams. Two shows the sail-in around the platform. Three shows the establishing of the aft connections. Four shows the sail-out, the substructure still visible in-situ.

2.3.1. MATING AND LIFTING

During the mating phase the vessel is positioned around the structure (Figure 2.5). The lift points will still have some clearance with respect to the topsides' connection points. The vessel will then be de-ballasted so that the lift- and connection point are brought closer together. At some point there will be a moment of impact. This impact should be as small as possible. *Pioneering Spirit* therefore uses a heave compensation system, compensating the vertical motions of the lifting point up to 1.2 meters amplitude. It is assumed that this concept will not use any form of a motion compensation system. The motions and limits will therefore be calculated for the vessel without motion compensation only, the impact velocity being the critical parameter. During the lifting phase the critical loads will be located in the connection beams and in the topsides. For each location the loads will have to be calculated to assess when the limiting load is reached. The weight of the topsides, the distance between the barges and the environmental conditions play a major role.

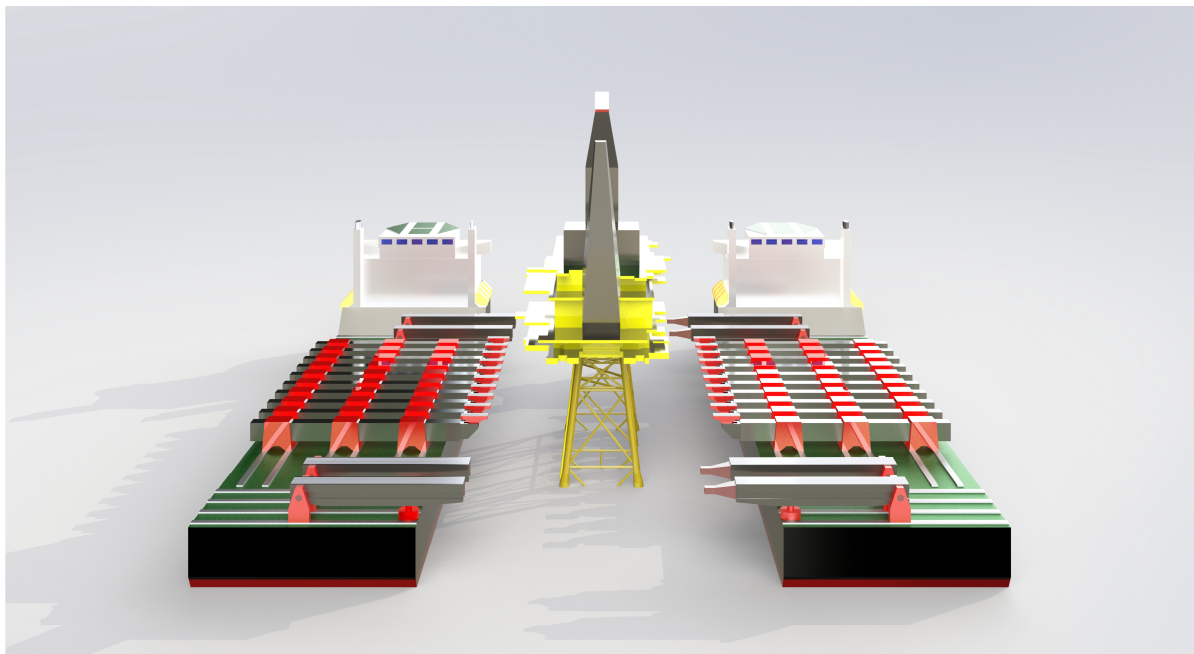
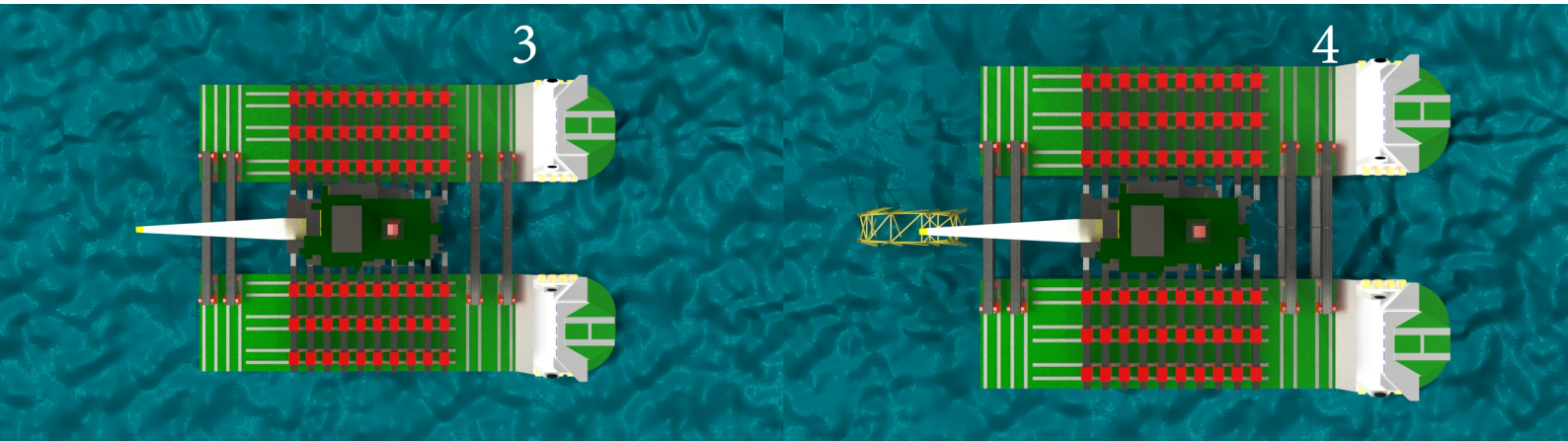


Figure 2.5: Sail-in and mating phase



2.3.2. SAIL OUT AND OFFLOADING

When the vessels are ballasted such that the topsides is lifted to a safe vertical clearance from the jacket, the sail out will take place. The aft connection beams are positioned above the jacket, therefore not obstructing the sail-out (Figure 2.6). When the vessel has sailed to a safe distance from the substructure, all is left is the offload phase. During this phase the topsides will be placed on a barge which will transport the topsides ashore. Alternatively the vessels can transport the topsides to a sheltered location, after which the topsides can be lowered on a barge in sheltered conditions. Once again the impact of the topsides on the grillage of the barge is the governing load. The impact velocity should again be as small as possible.

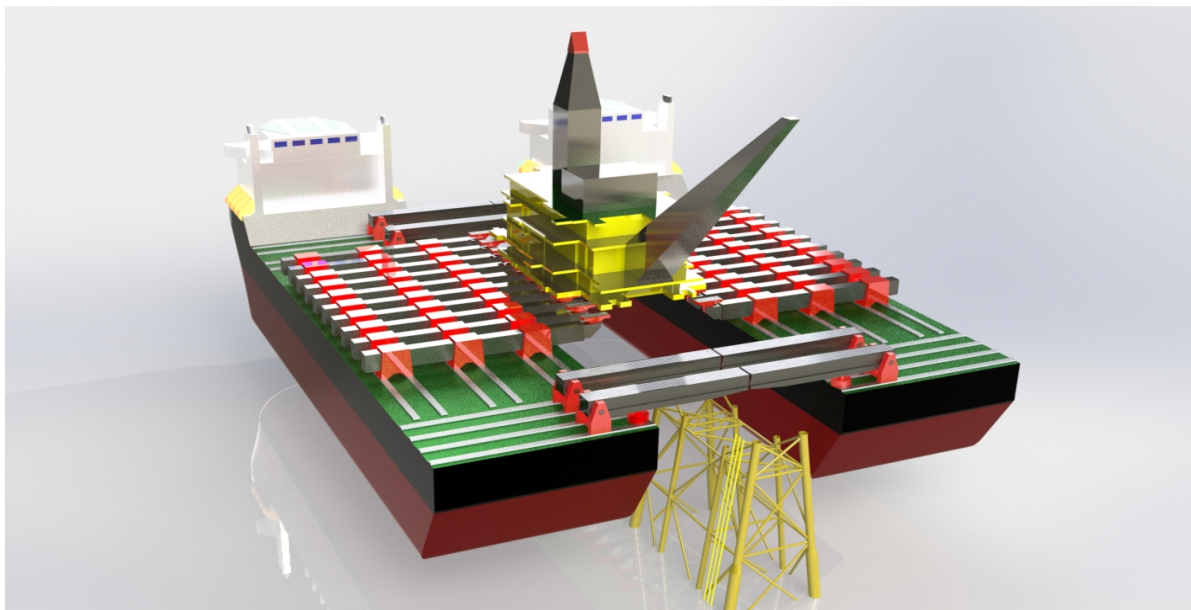


Figure 2.6: Sail-out phase: the aft connection beams fit over the remaining substructure

For each phase in the decommissioning operation limiting motions are obtained. An overview of the limiting parameters and the corresponding phases is given in Table 2.1.

Table 2.1: Limiting parameters of the operational envelope

Limit	Phase of occurrence
Impact velocity	Mating, Offload
Topsides load	Transport, Lifting
Connection load	Transport, Lifting
Topsides accelerations	Transport, Lifting

2.4. LIMITING RESPONSES

The three main limiting responses identified are the impact velocity during mating or installation, the forces in the connection beams and the stresses in the topsides. Throughout the operation none of the limits may be exceeded. In this section the magnitude of the limiting responses will be discussed.

2.4.1. IMPACT VELOCITY

The impact load during installation and mating phase depends on many different aspects. Depending on the ballast conditions, the topsides weight, the topsides strength and the presence of damping systems such as leg mating units (LMU), the maximum impact velocity can differ greatly. A limiting impact velocity of $0.2m/s$ was used to calculate the workability of a crane vessel lowering a cable reel onto another vessel [7]. For the installation of the Johan Sverdrup platform performed by Allseas also a maximum impact velocity of $0.2m/s$ was used. The jacket onto which the topsides was installed was equipped with LMUs to soften the impact. Because a maximum impact velocity of $0.2m/s$ has been used in similar operations, this value will be used as a general maximum impact velocity limit.

2.4.2. CONNECTION BEAM FORCES

The hydrodynamic loading will result in large forces in the connection beams. Not only the beam itself should be able to withstand this loading, also the hinged connection has to function while withstanding these loads. The lifting beams of *Pioneering Spirit* are connected to a hinged transition piece called a yoke (Figure 2.7). These yokes form the connection between the vessel and the topsides and are able to withstand a force of $6000t$ each. To withstand that amount of force a cylindrical axis with a diameter of $900mm$ is used. Because *Pioneering Spirit* is designed to lift extreme loads, the value of $6000t$ will be considered as such and used as maximum load in the connection beams.

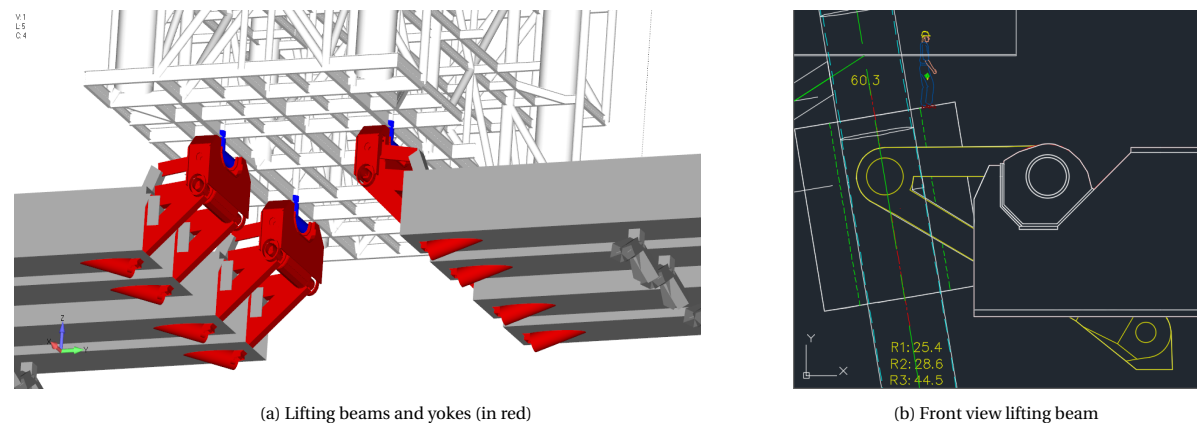


Figure 2.7: Drawings of the lifting beams and yokes, note the person in (b) for scale [courtesy of Allseas]

2.4.3. TOPSIDES FORCES

During the lifting and transit phase, the limiting stresses in the topsides may not be exceeded. When transporting a structure on a single barge, the stresses in the topsides are dominated by the accelerations of the vessel. The translation and rotation of the vessel will result in accelerations and therefore forces in the topsides. DNV states that the acceleration load case consists of either the combined heave and roll accelerations, or the combined heave and pitch accelerations [12, sec 7.9.1].

When using two separate barges different load cases are possible. It can be such that there is a relative pitch angle between the barges. This means that the topsides will be wrenched by the movement of the vessels. It is expected that the relative pitch results in limiting stresses in the topsides much faster than the accelerations will. Therefore a load case is proposed where the barges carrying the topsides are pitched relatively to each other.

To determine the maximum relative pitch angle an in-house FEM model of the Brent Alpha platform is used. The Brent Alpha platform is a jacket based platform with six legs that will be decommissioned by Allseas in the near future. The best lifting option is to place the barges parallel to the jacket in the longitudinal direction. A relative pitch angle will in this case mean that the outside legs are displaced in vertical direction, while the centre legs remain in place. The opposing diagonals are displaced in opposing directions (Figure 2.8).

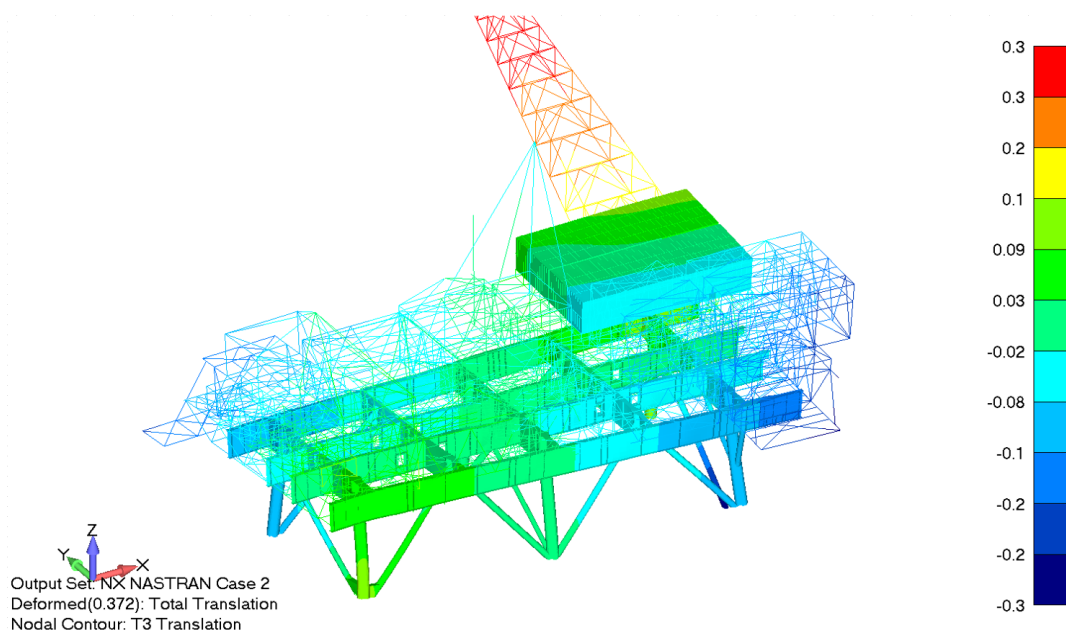


Figure 2.8: ANSYS FEM model of the Brent Alpha platform showing the vertical displacements in meters

As result of the displacements the Von Mises stresses can be calculated using the FEM model. The displacements are then increased until the stress exceeds the yielding stress (Figure 2.9). It is found that the stress limit is exceeded if the outside legs are displaced approximately 100 mm in opposite direction. With a distance between the two outer legs of 60m this results in an angle of:

$$\tan^{-1}\left(\frac{0.2}{60}\right) = 0.19^\circ \quad (2.1)$$

This angle is present at both sides of the platform, meaning that the maximum relative pitch angle that the barges can obtain for the Brent Alpha platform is approximately 0.38° before it fails. It is very well understood that this limit will be different for each platform and for different lifting configurations. Still a maximum relative pitch of 0.38° will be used as a first indicating limiting factor. Additionally the accelerations of the topsides and and the corresponding forces will be calculated as a double check. Regulation rules state that the accelerations can be calculated by making a distribution of the maximum acceleration values [12, p. 122]. The design value is then obtained by calculating the extreme value within the operation time span. The value is compared to the local constraint forces due to the the prescribed relative pitch displacement. It is expected that the force due to the accelerations can be neglected.

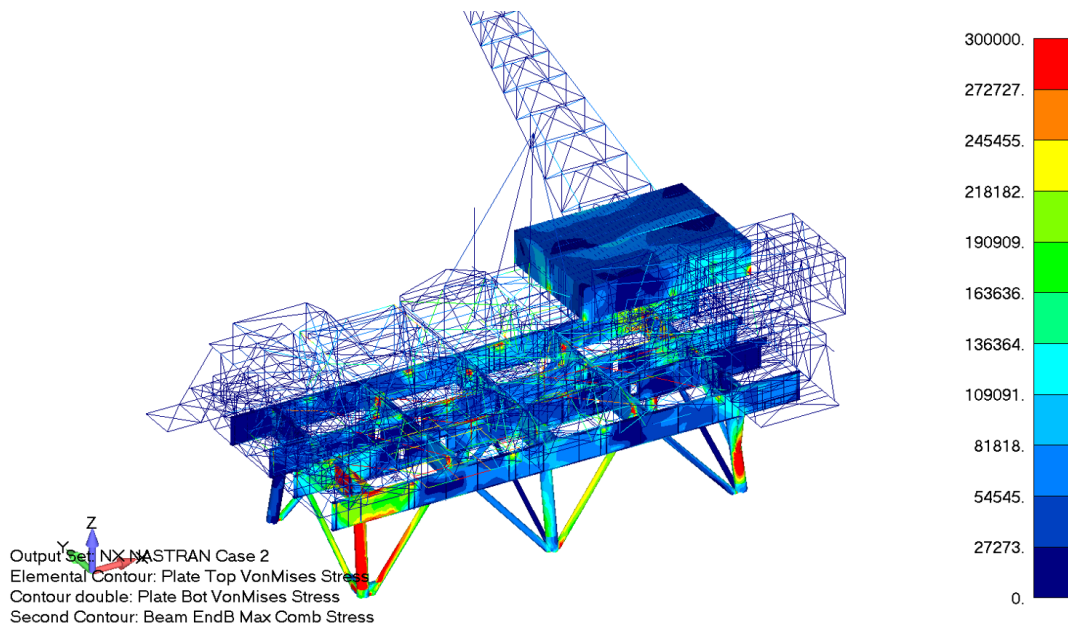


Figure 2.9: FEM model of the Brent Alpha platform showing von Mises stress kPa as a result of a vertical displacement of the outer legs of $100mm$

2.4.4. OVERVIEW LIMITS

Table 2.2 shows an overview of the magnitude of each limit. These limits will be used to calculate the workability of the lifting concept and say something about the most critical load case.

Table 2.2: Limiting parameters and their magnitude

Parameter	Limit	Unit
Impact velocity	0.2	(m/s)
Connection load	6000	(t)
Relative pitch	0.38	(°)

2.5. DIMENSIONS

In this section a base case will be defined. This base case can be seen as the starting position of all the following calculations. The most extreme platforms in the North Sea are discussed to give a feeling on the magnitude of the structures. Additionally existing barges are compared to define the base case barge dimensions.

2.5.1. EXTREME PLATFORMS IN THE NORTH SEA



Figure 2.10: Four of the most extreme North Sea platforms

The barge dimensions will be adapted for lifting the extreme platforms in the North Sea within the scope of the vessel (Figure 2.10). The most important parameters are the weight, water depth, airgap, width and length. The topsides dimensions are given in Table 2.3. These dimensions are used to define an upper and lower limit for each of the barge dimensions.

Table 2.3: North Sea Platform Dimensions

	Minimal platforms			Maximum platforms		
	Platform dimensions					
Weight	Armada	10,500	(t)	Gulfaks C	52,000	(t)
Water depth	Tyra	35	(m)	Troll A	303	(m)
Airgap	Thistle A	23	(m)	Gulfaks C	32	(m)
Width	Ekofisk 2/4J	20	(m)	Magnus	66.5	(m)
Length	Dunbar	26	(m)	Sleipner A	150	(m)

2.5.2. BASE CASE BARGE DIMENSIONS

As Allseas' focus lies on removing the larger topsides, large barges will have to be used. The initial barge dimensions will therefore be based on two of the largest barges available on the offshore market. These are the H851 owned by Heerema Marine Contractors [35], and the Iron Lady owned by Allseas. The relations between barge volume, weight, and ballast capacity of these barges are used to determine the properties of the base case barge.

For the sake of simplicity the base case barge design will measure 200m in length, 50m in width and will have a draught of 15m. These values are chosen as such because they are in the same order of magnitude as the Iron Lady and H851. The barge dimensions will be varied later on, therefore at this point it is only of importance that the base case dimensions are in the correct order of magnitude.



Figure 2.11: The H851 Barge and The President Hubert Tug Transporting the Tamar Jacket [downloaded free license picture]

To determine the structural properties of the base case barge information on the Iron Lady and H851 is used and interpolated. The weight is therefore determined as approximately 16% of the moulded volume of the barge. The ballast capacity is found to be approximately 98% of the maximum displacement. The radii of gyration k_{xx} , k_{yy} and k_{zz} , were found to be close to $0.35B$, $0.25L$ and $0.25L$ respectively [11, Pt. 3 Ch.1 Sec.4] [14] [20]. The barges are assumed to be symmetrical, meaning the x and y coordinates of the centre of gravity lie in the middle of the barges. The z coordinate of the centre of gravity is calculated with the following formula:

$$CoG_z = \frac{M_{barge} \cdot Z_{barge} + M_{ballast} \cdot Z_{ballast}}{M_{tot}} \quad (2.2)$$

Where Z_{barge} is the distance from the keel to the centre of gravity of the barge and is approximated to be 55% of the depth, which is approximately the same value as for the Iron Lady. This value is based on the inclination report of the Iron Lady, which can be found in Appendix E. Additionally $Z_{ballast}$ is the distance from the keel to the centre of gravity of the ballast. Table 2.4 shows the barge properties of both the Iron Lady and H851 as well as the properties of the base case barge.

Table 2.4: Barge dimensions of the Iron lady, H851 and the base case

	Iron Lady	H851	Base Case	
	Barge properties			
Weight	24.000	40.000	48.000	(t)
Length	200	260	200	(m)
Width	57	63	50	(m)
Depth	13	15	30	(m)
Draught	10.5	12	15	(m)
Ballast	120.000	205.000	142.500	(t)

Note that the moulded depth of the base case barge is increased to account for the large airgaps of the platforms in the North Sea. It is expected that the main deck should be at least fifteen meters above the water level when at maximum draught. The additional structure of the lifting beams is used to bridge the final five meters to the bottom of the topsides.

2.6. CHAPTER REVIEW

In this chapter the design proposed by Mathios and Wang is adapted and illustrated. The decommissioning operation is discussed step-by-step, pointing out the critical limits of the vessel. The stresses in the topsides,

the impact load from the vessel to the topsides and the stresses in the connection beams are considered as the main governing limits. Previous studies are used to determine the limiting impact velocity and connection loads. The maximum topsides stresses are expected to occur during the transport phase, when the vessels pitch relatively from each other. An in-house FEM model of the Brent Alpha platform is used to calculate the maximum relative pitch. Additionally the topsides acceleration will be considered in a later stadium of this thesis. The operational limits are given by Table 2.5.

Table 2.5: Limiting parameters and their magnitude

Parameter	Limit	Unit
Impact velocity	0.2	(m/s)
Connection load	6000	(t)
Relative pitch	0.38	(°)

Using the dimensions of the most extreme platforms in the North Sea a base case design is proposed. Two of the largest barges used in the offshore industry, the H851 and the Iron Lady, are used to calculate the properties of the base case design. These properties are found in Table 2.6.

Table 2.6: Barge dimensions of the Iron lady, H851 and the base case

	Iron Lady	H851	Base Case	
Barge properties				
Weight	24.000	40.000	48.000	(t)
Length	200	260	200	(m)
Width	57	63	50	(m)
Depth	13	15	30	(m)
Draught	10.5	12	15	(m)
Ballast	120.000	205.000	142.500	(t)

T H R E E

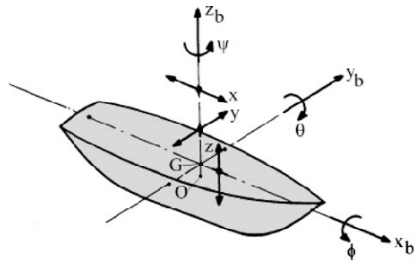
D Y N A M I C A L M O D E L

In this chapter the focus will lie on the dynamics of the coupled barges. The radiation diffraction software ANSYS Aqwa will be used to assess the hydrodynamic coefficients of the barges without connections. The influence of the connections will be added to this hydrodynamic assessment in Matlab to derive a linear dynamical model of the complete system. The assumption of linearity is substantiated in an additional evaluation of the influence of linearity on the motions of the vessels.

3 | Dynamical model of the coupled barges

3.1. DYNAMICAL MODEL

For every vessel six main degrees of freedom exist (Figure 3.1). The twin-barge lifting concept consists of two vessels and therefore has 12 degrees of freedom, namely $[x_1, y_1, z_1, \phi_1, \theta_1, \psi_1, x_2, y_2, z_2, \phi_2, \theta_2, \psi_2]$, representing the surge, sway, heave, roll, pitch and yaw for both barges. It is assumed that the motions of the vessels are small and can therefore be linearized. Linearizing the motions means that the position of a point P with coordinates $[x_p, y_p, z_p]$ after a vessel motion of $[x, y, z, \phi, \theta, \psi]$ is given by formula 3.1, 3.2 and 3.3.



$$P_x = x - y_p * \psi + z_p * \theta \quad (3.1)$$

$$P_y = y + x_p * \psi - z_p * \phi \quad (3.2)$$

$$P_z = z - x_p * \theta + y_p * \phi \quad (3.3)$$

Figure 3.1: Schematic overview of the degrees of freedom

3.2. MODELLING THE VESSELS

The modelling of the total system will be split up into two parts; the motions of the vessels and the influence of the connections. First the equations of motion of the system without connections will be calculated. Thereafter the stiffness of the connections will be added to the system. Figure ?? shows how the concept design is translated to simplified model containing two rectangular barges and a number of springs.

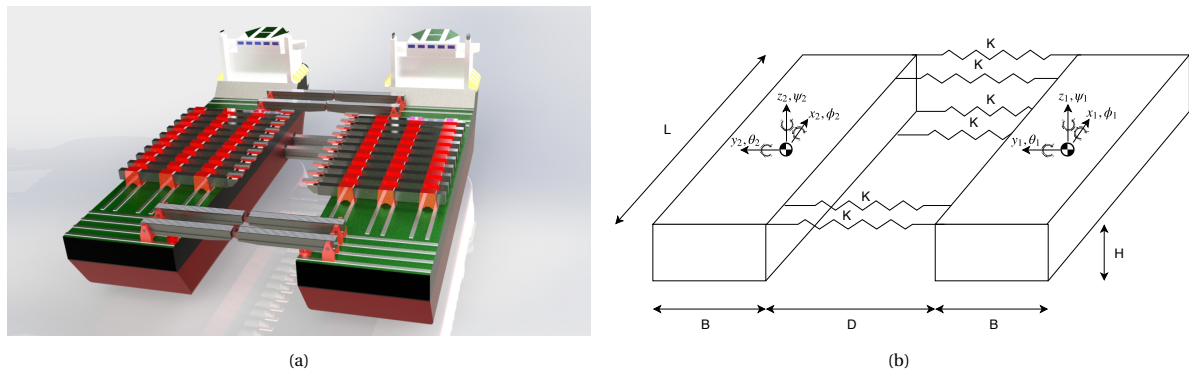


Figure 3.2: From vessel (a) to free-body diagram (b)

The equations of motion of the dynamical model will be of the following form:

$$\begin{bmatrix} M_{1,1} & \cdots & M_{1,6} & \vdots & M_{1,7} & \cdots & M_{1,12} \\ \vdots & \ddots & \vdots & \vdots & \vdots & \ddots & \vdots \\ M_{6,1} & \cdots & M_{6,6} & \vdots & M_{6,7} & \cdots & M_{6,12} \\ \cdots & \cdots & \cdots & \vdots & \cdots & \cdots & \cdots \\ M_{7,1} & \cdots & M_{7,6} & \vdots & M_{7,7} & \cdots & M_{7,12} \\ \vdots & \ddots & \vdots & \vdots & \vdots & \ddots & \vdots \\ M_{12,1} & \cdots & M_{12,6} & \vdots & M_{12,7} & \cdots & M_{12,12} \end{bmatrix} \cdot [\ddot{q}] + \begin{bmatrix} B_{1,1} & \cdots & B_{1,6} & \vdots & B_{1,7} & \cdots & B_{1,12} \\ \vdots & \ddots & \vdots & \vdots & \vdots & \ddots & \vdots \\ B_{6,1} & \cdots & B_{6,6} & \vdots & B_{6,7} & \cdots & B_{6,12} \\ \cdots & \cdots & \cdots & \vdots & \cdots & \cdots & \cdots \\ B_{7,1} & \cdots & B_{7,6} & \vdots & B_{7,7} & \cdots & B_{7,12} \\ \vdots & \ddots & \vdots & \vdots & \vdots & \ddots & \vdots \\ B_{12,1} & \cdots & B_{12,6} & \vdots & B_{12,7} & \cdots & B_{12,12} \end{bmatrix} \cdot [\dot{q}] + \cdots \\
\begin{bmatrix} K_{1,1} & \cdots & K_{1,6} & \vdots & K_{1,7} & \cdots & K_{1,12} \\ \vdots & \ddots & \vdots & \vdots & \vdots & \ddots & \vdots \\ K_{6,1} & \cdots & K_{6,6} & \vdots & K_{6,7} & \cdots & K_{6,12} \\ \cdots & \cdots & \cdots & \vdots & \cdots & \cdots & \cdots \\ K_{7,1} & \cdots & K_{7,6} & \vdots & K_{7,7} & \cdots & K_{7,12} \\ \vdots & \ddots & \vdots & \vdots & \vdots & \ddots & \vdots \\ K_{12,1} & \cdots & K_{12,6} & \vdots & K_{12,7} & \cdots & K_{12,12} \end{bmatrix} \cdot [q] = \begin{bmatrix} F_1 \\ \vdots \\ \vdots \\ \vdots \\ \vdots \\ \vdots \\ F_{12} \end{bmatrix}$$

where M represents the mass and added mass ($M = M + A$), B represents the damping, K the stiffness, F represents the wave force and q is a vector containing the motions in all 12 degrees of freedom. To calculate the wave forcing, added mass and damping the potential solver ANSYS Aqwa is used. The system above is a well known solvable system of differential equations, is it not that the added mass and damping are frequency dependent. This means that for each forcing frequency a different set of motion equations exists. The general way of coping with this is the frequency domain approach which uses the superposition principle.

3.2.1. THE SUPERPOSITION PRINCIPLE

To calculate the motions of the vessels the superposition principle is used. This principle states that a wave spectrum is a superposition of a large number of waves with different frequencies, amplitudes and phases [21, sec. 5-27] [16, p. 18-34]. For each frequency a different set of differential equations can be solved to calculate the vessel motions. This calculation is repeated for all the frequencies available in the wave spectrum separately. The actual motion is then the summation of all the separate motions. The connection between superposition, time domain and frequency domain is illustrated in Figure 3.3.

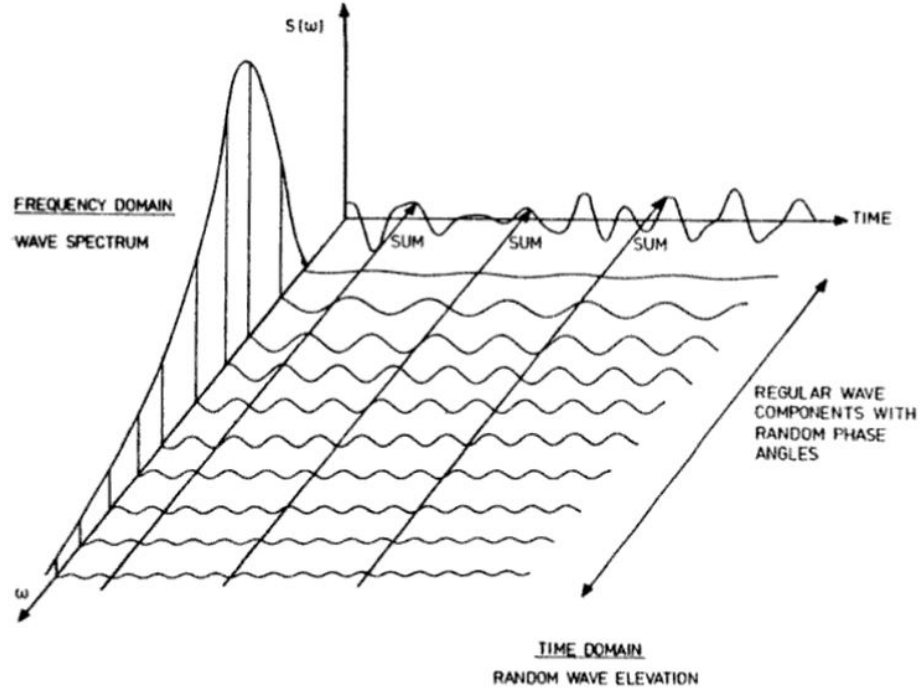


Figure 3.3: Illustration of connection between time- and frequency domain and wave superposition [16]

The superposition principle is only possible because the following assumptions are made:

1. All body motions are harmonic.
2. The motions are to a first order and hence must be of a small amplitude.
3. The equations of motion have to be linear, that means no (nonlinear) viscous damping.

When M , A , B , K and F are known, one can see that the displacement, velocity, accelerations and phase difference are the only unknowns.

$$(\bar{M} + \bar{A})\ddot{q} + \bar{B}\dot{q} + \bar{K}q = \bar{F}e^{-i\omega t} \quad (3.4)$$

Assuming that the body motions are harmonic one can say that for the displacement, velocity and acceleration the following holds:

$$q = H_f e^{-i\omega t + \zeta} \quad (3.5)$$

$$\dot{q} = -i\omega H_f e^{-i\omega t + \zeta} \quad (3.6)$$

$$\ddot{q} = -\omega^2 H_f e^{-i\omega t + \zeta} \quad (3.7)$$

Where H_f represents the transfer function from the force amplitude to the amplitude of the displacement. By substituting equations 3.5, 3.6 and 3.7 into equation 3.4, only two unknowns remain: H_f and ζ . By choosing t such that $(i\omega t + \zeta) = 0$ and $(i\omega t + \zeta) = \frac{1}{2}\pi$, both unknowns can be determined. If the transfer function is somehow dependent on the displacement itself, the motions will not be linearly correlated with the force amplitude. This means that the foundation of the superposition principle, linearity, does not hold anymore.

A time domain approach is then needed. To come up with the motions of the vessels the transfer function is used to transfer the wave motions to the vessel motions.

3.2.2. HYDRODYNAMICAL COUPLING BETWEEN THE VESSELS

Focussing on the mass and added mass matrix, one can see that the matrix can be split up in four quadrants (Figure 3.4). The upper left and lower right quadrants represent the masses of the first and second barge respectively. The masses and moments of inertia of the two barges will be inserted on the diagonals of these quadrants. Outside the diagonals coupling terms will appear as a result of interaction between the motions of a *single barge*. One example of such a term can be the motion of centre of gravity in heave direction due to a pitch motion. For the first barge this coupling term will be located on the [3, 5] and [5, 3] position. Different coupling terms can be imagined.

$$\begin{bmatrix} M_{1,1} & \cdots & M_{1,6} & | & M_{1,7} & \cdots & M_{1,12} \\ \vdots & \ddots & \vdots & & \vdots & \ddots & \vdots \\ M_{6,1} & \cdots & M_{6,6} & | & M_{6,7} & \cdots & M_{6,12} \\ \hline M_{7,1} & \cdots & M_{7,6} & | & M_{7,7} & \cdots & M_{7,12} \\ \vdots & \ddots & \vdots & & \vdots & \ddots & \vdots \\ M_{12,1} & \cdots & M_{12,6} & | & M_{12,7} & \cdots & M_{12,12} \end{bmatrix}$$

Figure 3.4: Quadrants of the mass-matrix

The interaction between the two barges is represented by the upper right and lower left quadrant. This interaction will be the consequence of the waves that are radiated and diffracted by one barge, and encountered by the other barge. These coupling terms are also to be calculated with the potential solver. For the damping and force matrices the same coupling terms exist. Now only the added mass, damping and wave forces have to be determined. To determine the missing terms in the set of differential equations potential theory is used.

3.2.3. POTENTIAL THEORY

The structural mass, and the stiffness are properties belonging to the structure itself. The added mass, damping and wave force however, are properties that are different for each frequency. Additionally, the wave force depends also on the wave direction. To derive these properties potential theory will be used. Different commercial computer programs exist that use this potential theory to calculate these properties of the vessel. One of which is ANSYS Aqwa-line which will be used in this case. An explanation on potential theory and how ANSYS Aqwa uses it is given in Appendix B.

The outcome of the potential solver will be a system of matrices; the mass, damping, stiffness and force matrices. Because the added-mass and damping are frequency dependent, these matrices will be three dimensional and of the size $[Dof, Dof, \omega]$. The wave force additionally depends on the wave direction and will be of the size $[\theta, Dof, \omega]$, where θ is the number of different wave directions and ω is the number of different frequencies. In Figure 3.5 the mass matrix is given as an example of what such a matrix will look like. The number of frequencies depend on the frequencies occurring in the wave spectrum and the desired accuracy of the calculation.

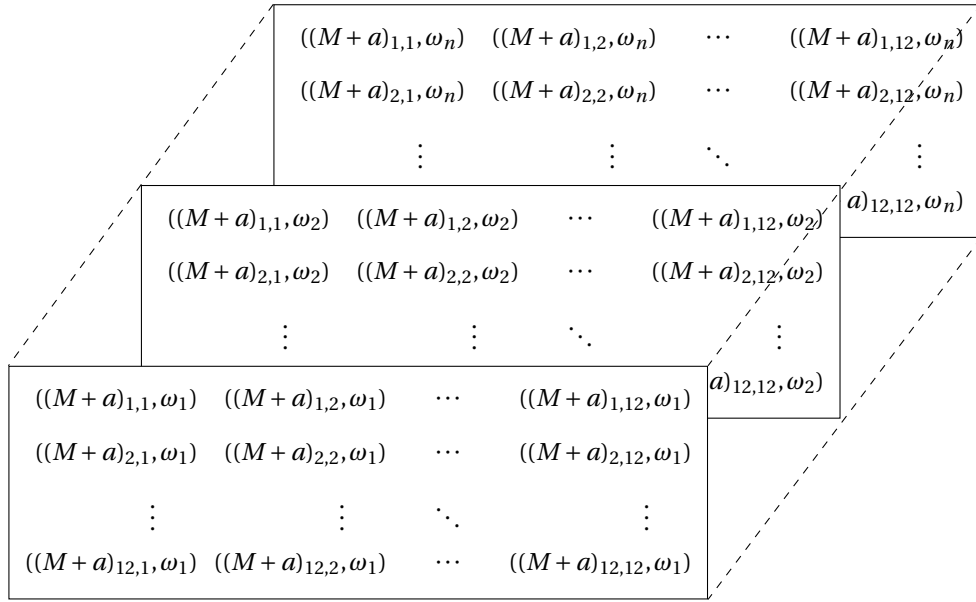


Figure 3.5: 3D frequency dependent mass-matrix

3.3. MODELLING THE CONNECTIONS

The barges are connected with six rigid connections which will be represented by springs with stiffness k (Figure 3.6). The rigid connections can be simulated by increasing this stiffness to a very high value. To determine the equations of motion the force and virtual work methods are used. These methods use the change in kinetic and potential energy to calculate the equations of motion. The main challenge here is to decide in what detail the vessels' motions result in spring elongation and therefore change in force or potential energy. When we linearize the system only the sway, roll and yaw motion of the barges will result in elongation of the springs. When the left barge will roll, so will the right barge and the same holds for the sway and yaw motion.

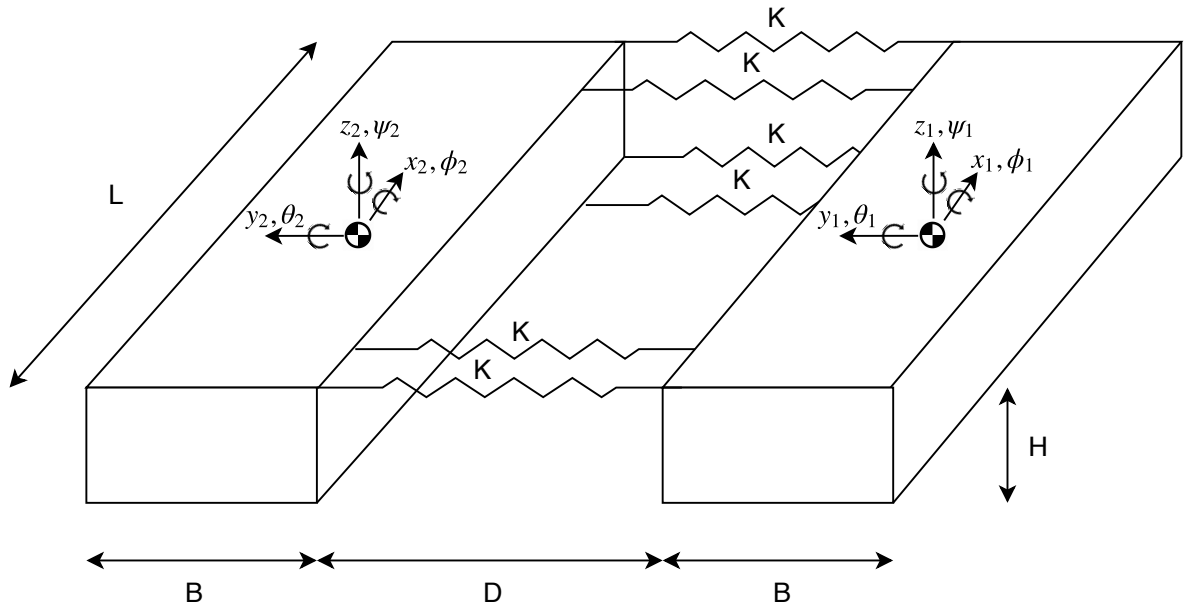


Figure 3.6: 3D free body diagram of the coupled barges

One can argue that in reality the positive heave motion of the left barge will result in a negative sway motion

of the right barge. Other motions of the barges will be coupled in the same way (Figure 3.7). Linearizing the system will mean that this coupling is not taken into account. In other words: the barges can freely, independently heave without influencing each other through the connections, when the connections are linearized. However, when this coupling *is* taken into account, nonlinear terms will be included in the equations of motion. This will mean that the superposition principle in the frequency domain does not hold any more. A time domain approach is needed in that case. To assess what the influence of linearising the connections is, two simplified 2D models of the system are made. One using linearised connections, and one using the nonlinear connections. The outcome of both models is compared to see whether there is a significant difference between both models. This assessment can be found in Appendix A. The outcome of the assessment shows that for wave amplitudes of around 1m, no significant differences are observed. Therefore the connections are linearised. The results of the linearized model will later on be compared with a nonlinear time domain model of the system in Orcaflex to validate the results.

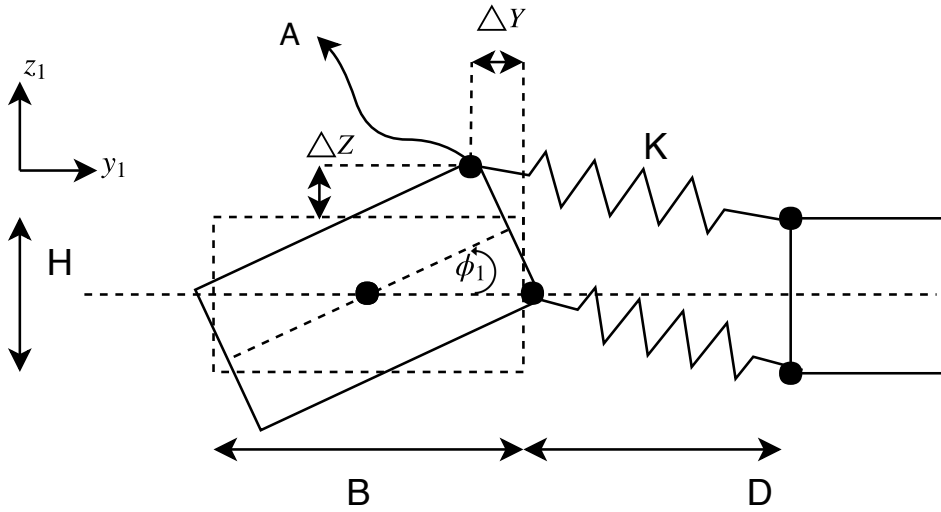


Figure 3.7: Elongation of connections

3.3.1. DERIVATION OF THE EQUATIONS OF MOTION

ANSYS Aqwa is used to determine the hydromechanic part of the equations of motion, consisting of the mass, added mass, damping, hydromechanic stiffness and wave excitation force. The stiffness of the connections still has to be added to these equations. In this section the latter part of the equations of motion is derived. For each degree of freedom the forces and moments exerted by each spring in that degree of freedom can be calculated using the free-body-diagram in Figure 3.6. Due to the assumption of linear springs only motions in sway (y), roll (ϕ) and yaw (ψ) result in elongation of the springs. To come up with the stiffness matrix of the connection only these degrees of freedom have to be discussed.

The forces and moments exerted on the barges by the first spring are given by the following set of equations:

$$\begin{aligned}
 F_{y1} &= k_1(y_1 - y_2) - k_1 H_1(\phi_1 - \phi_2) + k_1 L_1(\psi_1 - \psi_2) \\
 M_{\phi 1} &= -k_1 H_1(y_1 - y_2) + k_1 H_1^2(\phi_1 - \phi_2) - k_1 H_1 L_1(\psi_1 - \psi_2) \\
 M_{\psi 1} &= k_1 L_1(y_1 - y_2) - k_1 H_1 L_1(\phi_1 - \phi_2) + k_1 L_1^2(\psi_1 - \psi_2) \\
 F_{y2} &= k_1(y_2 - y_1) - k_1 H_1(\phi_2 - \phi_1) + k_1 L_1(\psi_2 - \psi_1) \\
 M_{\phi 2} &= -k_1 H_1(y_2 - y_1) + k_1 H_1^2(\phi_2 - \phi_1) - k_1 H_1 L_1(\psi_2 - \psi_1) \\
 M_{\psi 2} &= k_1 L_1(y_2 - y_1) - k_1 H_1 L_1(\phi_2 - \phi_1) + k_1 L_1^2(\psi_2 - \psi_1)
 \end{aligned} \tag{3.8}$$

where L_1 and H_1 are the x- and z- coordinates of the connection point with respect to the point of rotation of the barge. In the case of the first spring, both L_1 and H_1 are positive. Per spring the values for L_1 and H_1 , until L_6 and H_6 , change. The equations 3.8 however stay the same.

The set of equations of each of the springs can be transformed into a stiffness matrix of the given spring. For the first spring this results in the following set of equations:

$$\begin{bmatrix} k_1 & -k_1 H_1 & k_1 L_1 & -k_2 & k_1 H_1 & -k_1 L_1 \\ -k_1 H_1 & k_1 H_1^2 & -k_1 H_1 L_1 & k_1 H_1 & -k_1 H_1^2 & k_1 H_1 L_1 \\ k_1 L_1 & -k_1 H_1 L_1 & k_1 L_1^2 & -k_1 L_1 & k_1 H_1 L_1 & -k_1 L_1^2 \\ -k_1 & k_1 H_1 & -k_1 L_1 & k_2 & -k_1 H_1 & k_1 L_1 \\ k_1 H_1 & -k_1 H_1^2 & k_1 H_1 L_1 & -k_1 H_1 & k_1 H_1^2 & -k_1 H_1 L_1 \\ -k_1 L_1 & k_1 H_1 L_1 & -k_1 L_1^2 & k_1 L_1 & -k_1 H_1 L_1 & k_1 L_1^2 \end{bmatrix} \cdot \begin{bmatrix} y_1 \\ \phi_1 \\ \psi_1 \\ y_2 \\ \phi_2 \\ \psi_2 \end{bmatrix} = \begin{bmatrix} F_{y_1} \\ M_{\phi_1} \\ M_{\psi_1} \\ F_{y_2} \\ M_{\phi_2} \\ M_{\psi_2} \end{bmatrix}$$

In the same way the equations of motion can be derived with the method of virtual work.

3.3.2. METHOD OF VIRTUAL WORK

A different way of deriving the equations of motion is the method of virtual work. This method states that:

$$\delta T + \delta V = \delta W \quad (3.9)$$

where,

$$\begin{aligned} \delta T &= \text{Virtual kinetic energy} \\ \delta V &= \text{Virtual potential energy} \\ \delta W &= \text{Virtual work} \end{aligned} \quad (3.10)$$

Only springs are concerned here, meaning only the potential energy needs to be determined. For a spring holds:

$$\delta V = \delta \left(\frac{1}{2} k x^2 \right) = \delta x k x \quad (3.11)$$

Here, δx is the virtual displacement, k is the stiffness of the spring and so kx is the force in the spring. And indeed, a (virtual) displacement times a force results in (virtual) work. In the case of the linear coupled barges, again only motions in sway (y), roll (ϕ) and yaw (ψ) result in elongation of the springs. Equation 3.11 translates into:

$$\delta V = \delta (y_2 - y_1 + H_1 \phi_1 - H_1 \phi_2 - L_1 \psi_1 + L_1 \psi_2) k_1 (y_2 - y_1 + H_1 \phi_1 - H_1 \phi_2 - L_1 \psi_1 + L_1 \psi_2) \quad (3.12)$$

For each degree of freedom, δDoF can be taken as 1, while the other degrees of freedom are taken to be zero. So first:

$$[\delta y_1 = 1, \delta y_2 = 0, \delta \phi_1 = 0, \delta \phi_2 = 0, \delta \psi_1 = 0, \delta \psi_2 = 0] \quad (3.13)$$

then:

$$[\delta y_1 = 0, \delta y_2 = 1, \delta \phi_1 = 0, \delta \phi_2 = 0, \delta \psi_1 = 0, \delta \psi_2 = 0] \quad (3.14)$$

and so on. Substituting these input variables in equation 3.12 for each degree of freedom results in the following set of equations:

$$\begin{aligned}
\delta y_1 &: k_1(y_1 - y_2) - k_1 H_1(\phi_1 - \phi_2) + k_1 L_1(\psi_1 - \psi_2) \\
\delta \phi_1 &: -k_1 H_1(y_1 - y_2) + k_1 H_1^2(\phi_1 - \phi_2) - k_1 H_1 L_1(\psi_1 - \psi_2) \\
\delta \psi_1 &: k_1 L_1(y_1 - y_2) - k_1 H_1 L_1(\phi_1 - \phi_2) + k_1 L_1^2(\psi_1 - \psi_2) \\
\delta y_2 &: k_1(y_2 - y_1) - k_1 H_1(\phi_2 - \phi_1) + k_1 L_1(\psi_2 - \psi_1) \\
\delta \phi_2 &: -k_1 H_1(y_2 - y_1) + k_1 H_1^2(\phi_2 - \phi_1) - k_1 H_1 L_1(\psi_2 - \psi_1) \\
\delta \psi_2 &: k_1 L_1(y_2 - y_1) - k_1 H_1 L_1(\phi_2 - \phi_1) + k_1 L_1^2(\psi_2 - \psi_1)
\end{aligned} \tag{3.15}$$

And in fact these equations are the same as equations 3.8 and will result in the same stiffness matrix. So again, but now for all twelve degrees of freedom:

$$\begin{bmatrix}
0 & 0 & 0 & 0 & 0 & 0 & 0 & 0 & 0 & 0 & 0 & 0 \\
0 & k_1 & 0 & -k_1 H_1 & 0 & k_1 L_1 & 0 & -k_1 & 0 & k_1 H_1 & 0 & -k_1 L_1 \\
0 & 0 & 0 & 0 & 0 & 0 & 0 & 0 & 0 & 0 & 0 & 0 \\
0 & -k_1 H_1 & 0 & k_1 H_1^2 & 0 & -k_1 H_1 L_1 & 0 & k_1 H_1 & 0 & -k_1 H_1^2 & 0 & k_1 H_1 L_1 \\
0 & 0 & 0 & 0 & 0 & 0 & 0 & 0 & 0 & 0 & 0 & 0 \\
0 & k_1 L_1 & 0 & -k_1 H_1 L_1 & 0 & k_1 L_1^2 & 0 & -k_1 L_1 & 0 & k_1 H_1 L_1 & 0 & -k_1 L_1^2 \\
0 & 0 & 0 & 0 & 0 & 0 & 0 & 0 & 0 & 0 & 0 & 0 \\
0 & -k_1 & 0 & k_1 H_1 & 0 & -k_1 L_1 & 0 & k_1 & 0 & -k_1 H_1 & 0 & k_1 L_1 \\
0 & 0 & 0 & 0 & 0 & 0 & 0 & 0 & 0 & 0 & 0 & 0 \\
0 & k_1 H_1 & 0 & -k_1 H_1^2 & 0 & k_1 H_1 L_1 & 0 & -k_1 H_1 & 0 & k_1 H_1^2 & 0 & -k_1 H_1 L_1 \\
0 & 0 & 0 & 0 & 0 & 0 & 0 & 0 & 0 & 0 & 0 & 0 \\
0 & -k_1 L_1 & 0 & k_1 H_1 L_1 & 0 & -k_1 L_1^2 & 0 & k_1 L_1 & 0 & -k_1 H_1 L_1 & 0 & k_1 L_1^2
\end{bmatrix} \cdot \begin{bmatrix} x_1 \\ y_1 \\ z_1 \\ \phi_1 \\ \theta_1 \\ \psi_1 \\ x_2 \\ y_2 \\ z_2 \\ \phi_2 \\ \theta_2 \\ \psi_2 \end{bmatrix} = \begin{bmatrix} F_{x_1} \\ F_{y_1} \\ F_{z_1} \\ M_{\phi_1} \\ M_{\theta_1} \\ M_{\psi_1} \\ F_{x_2} \\ F_{y_2} \\ F_{z_2} \\ M_{\phi_2} \\ M_{\theta_2} \\ M_{\psi_2} \end{bmatrix}$$

It has to be noted that this is the system of equations for one connection only. The stiffness matrices of the other connections still have to be added to the total system. This makes it easier to add more connections, or change the locations of each connection separately. Additionally the total stiffness matrix of all connections has to be added to the system of hydrodynamic equations which are calculated using ANSYS Aqwa. It was shown in Appendix A that the motions of the barges are coupled successfully when using a connection stiffness of $K = 10^9 N/m$. For a lifting beam of $100m$ in length with a Young's modulus of $E = 200GPa$ the cross sectional area of the beam can be calculated as:

$$A = \frac{kL}{E} = 0.5m^2 \tag{3.16}$$

assuming that the stress is linearly proportional to strain below the yield strength. Lifting beams of this size can very well be designed and produced.

3.4. CHAPTER REVIEW

This chapter gives insight in the dynamical model of the coupled barges. Twelve degrees of freedom exist, meaning the system of motion equations exist of twelve-by-twelve matrices. The added mass, damping and wave excitation force matrices are determined using potential theory. Because these hydrodynamic parameters are frequency dependent the frequency domain approach is adopted, which makes use of the superposition principle. An important condition of this principle is that system has to be linear. Thereafter the influence of the connections is included in the stiffness matrix. This influence is linearised to meet the term of linearity. The consequences of this linearisation are assessed in Appendix A, showing no significant differences between linear and nonlinear connections for small incoming wave amplitudes.



F O U R

H Y D R O D Y N A M I C I N T E R A C T I O N

In this chapter the outcome of the first ANSYS Aqwa calculations are presented and discussed. The assumptions made within potential theory compels one to carefully interpret these results. The outcome is compared to experimental results of previous studies on the topic of side-by-side moored vessels. Based on these previous studies, damping is added to the model to adjust for the nonlinear damping that ANSYS Aqwa does not include.

4 | Hydrodynamic interaction

4.1. CALCULATION OF THE RESPONSE AMPLITUDE OPERATOR

After the Aqwa calculation the hydrodynamic properties of the configuration are loaded into Matlab. These are then used to calculate the response amplitude operator or RAO. These RAO's are technically a linear transfer function between the incoming waves and the vessel motions. The set of equations that is obtained is as follows:

$$M(s)\ddot{X} + M(a)\dot{X} + C\dot{X} + K(s)X = F \quad (4.1)$$

Where:

- $M(s)$ is the size [12, 12] structural mass matrix.
- $M(a)$ is the size [12, 12, ω] added mass matrix.
- C is the size [12, 12, ω] potential damping matrix.
- $K(s)$ is the size [12,12] stiffness matrix.
- F is the size [θ , 12, ω] complex force vector.
- X is the size [12, ω] displacement vector.

AQWA assumes X and F to be of the form

$$X = X_0 e^{-i\omega t} \quad \text{and} \quad F = F_0 e^{-i\omega t} \quad (4.2)$$

Where ω is the wave frequency. The complex transfer function will then become:

$$H = \frac{X}{Z} = \frac{F_0}{(K(s) - [M(s) + M(a)]\omega^2 - iC\omega)} \quad (4.3)$$

The RAO can now finally be calculated by taking the absolute value of the complex transfer function. The phase can be obtained by taking the angle of the complex transfer function.

To calculate the RAO of a certain point at the vessel one can simply multiply the RAO at the centre of gravity with a translation matrix to the point of interest. The RAO at a defined point p are then given by the following formula:

$$X_p = T \cdot X_g \quad (4.4)$$

where T represents the translation matrix of point p . Using this relation the complex transfer function of two separate points, p_1 on the portside barge and p_2 on the starboard barge, can be evaluated. Still containing the phase information, the transfer functions can be used to determine the relative distance between both points as well. When p_1 and p_2 represent the locations of the connection points of the connection beams, the relative distance between the two points can be used to calculate the elongation and thus the force in the beams.

Additionally the complex transfer functions of both barges can be used to calculate the relative pitch between the barges in the same way.

4.2. IRREGULAR FREQUENCIES

As discussed in Appendix B certain assumptions are made within ANSYS Aqwa to simplify the calculations. Vorticity and viscosity are absent in the calculation. Additionally, ANSYS Awqa calculates the hydrodynamic parameters numerically, meaning that also numerical errors might occur. The results therefore have to be interpreted carefully. This is directly evident when looked at the heave RAO obtained with ANSYS Aqwa.

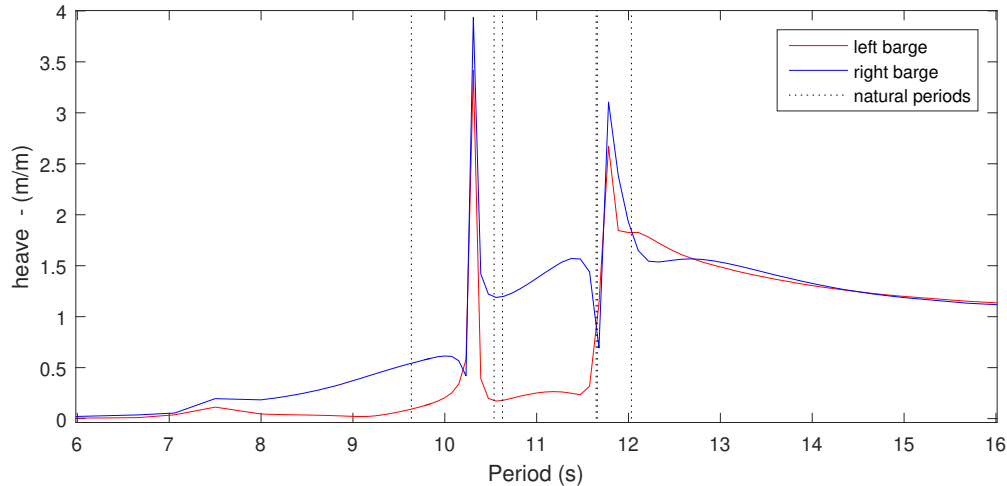


Figure 4.1: Heave RAO uncoupled barges for beam waves where the right barge first encounters the waves.

In Figure 4.1 some remarkable peaks are visible in the heave RAO for the uncoupled barges base case configuration: ($L = 200m$, $B = 50m$, $T = 15m$, $D = 50m$). It is difficult to imagine a heave motion of almost 4 meters for a 1 meter incoming wave at one certain frequency that is not even a natural frequency. The first possible explanation of this effect is the occurrence of irregular frequencies. About this subject C.H. Lee and P.D. Sclavounos state the following: "Irregular frequencies arise in boundary-integral formulations of wave problems, notably exterior problems in acoustics and surface-wave-body interactions. At the irregular frequencies the integral equations either possess no solutions, or if solutions exist they are not unique" [25]. Another way of thinking of these effects is the occurrence of wave resonance *inside* the floating body. In the software the waves are reflected inside the floating body and standing waves occur. This may result in peaks in the RAO's.

4.2.1. INTERNAL LID

The solution to this problem adopted by ANSYS Aqwa is the implementation of an internal lid. It is modelled as a surface inside the floating body, prohibiting wave elevations inside the barges.

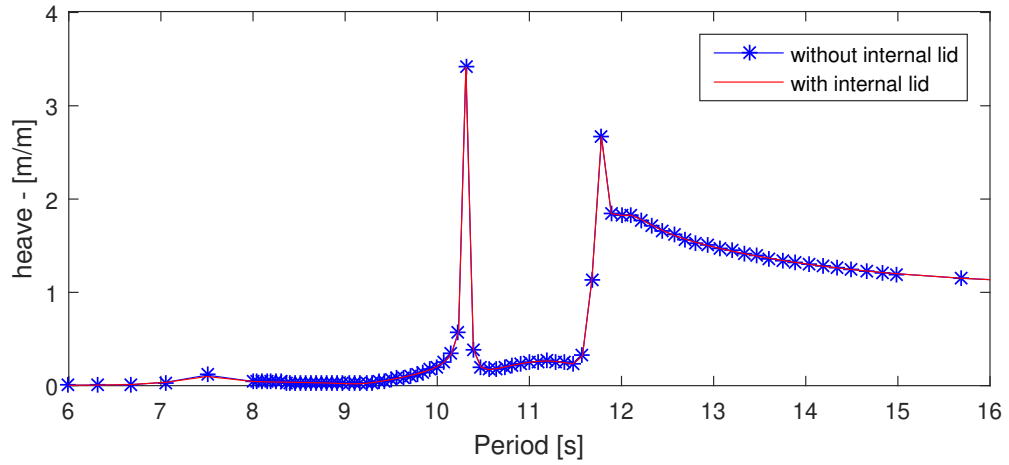


Figure 4.2: Influence of an internal lid on the heave RAO for beam waves.

The implementation of an internal lid has no effect on the peaks found in the heave RAOs (Figure 4.2). Additionally the influence of an internal lid on the added mass and damping is examined. For heave no change is observed for the added mass and damping when applying a lid. For the sway motion the influence of a lid is visible to some extent (Figure 4.3).

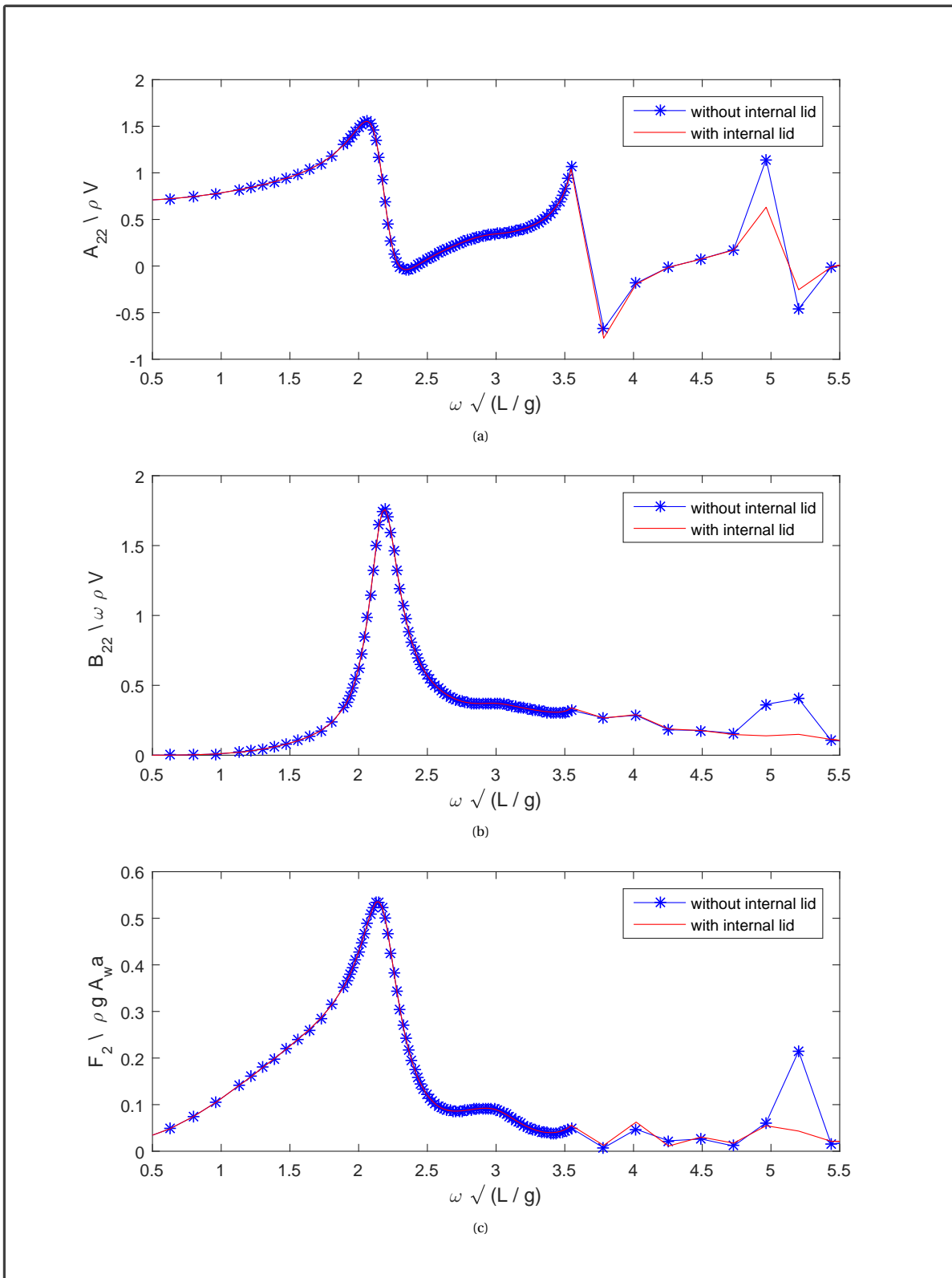


Figure 4.3: The effect of an internal lid on the added mass (a), damping (b) and wave force (c) (beam waves) for sway direction. The added mass is normalized by ρ times the volume V , damping is normalized by the ω times ρ times the volume V and the wave force is normalized by ρ, g , the water plane area A_w and the wave amplitude a .

For the higher frequencies some effects of the internal lid are visible. These higher frequencies are however

not the frequencies where the peaks in the RAOs are occurring. It also should be noted that the added mass becomes negative at different frequencies throughout the graph. This will mean that in some way energy is added to the system at these frequencies, which is not physically possible. In time domain simulations it could lead to an unstable system. That the internal lid does not change these effects means that the problem can not be explained by the presence of resonance inside the floating bodies. The peaks should be interpreted in a different way. No internal lid will therefore be included in the ANSYS Aqwa model.

4.3. ADDITIONAL DAMPING

The second possible explanation is that this peak at $T = 10.32s$ can be explained by the presence of standing waves *in between* the barges. Fournier discusses this effect in a paper on the hydrodynamics of two side-by-side vessels [17]. He compares experimental results of two side-by-side LNG Carriers (a distance of 25 meters) with numerical findings. One of the main findings is that due to the lack of viscous damping in the radiation/diffraction software wave elevations are greatly overestimated by the software for certain frequencies. The wave elevation resonance has an influence on the 1st order wave forces, and therefore also on the vessel motions. Peña and McDougall also discuss the limitations of diffraction theory when it comes to interacting effects between fixed and floating structures [32]. They model a vessel floating next to a quay-side for different distances up to 54 meters. The focus of the research lies more on the calculated damping and added mass. Results show that even for a distance of 54 meters substantial variations in added mass and damping occur for certain frequencies. For some frequencies the added mass even becomes negative on the diagonal terms. According to Peña this did not present a problem when performing spectral analysis. However, when a dynamic analysis was conducted the simulations could become unstable. The vessel seemed to generate energy with an increasing motion as result. This discussed effect is also visible for the side-by-side barges configuration in this thesis (Figure 4.4). An incoming wave with a period of 10.3s and an amplitude of one meter results in a standing wave of almost eighteen (!) meters in between the barges. The main reason of the standing wave effect is the negligence of certain forms of nonlinear damping by the linear potential theory. Damping sources such as viscous damping are not taken into account for this reason.

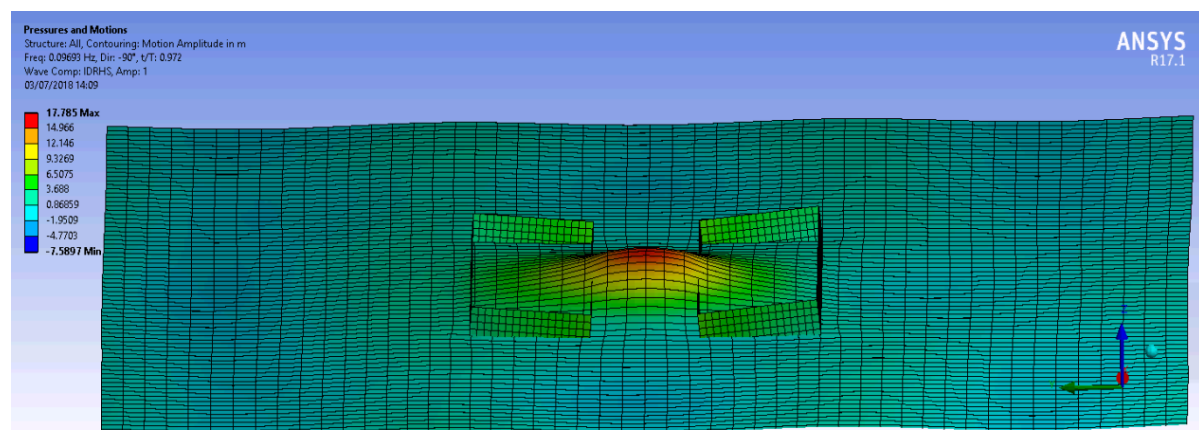


Figure 4.4: Standing wave in between barges for a wave with $A = 1m$ and $T = 10.3s$, in the environment of ANSYS Aqwa

4.3.1. ADDED ROLL DAMPING

The damping calculated within potential theory represents the energy that is dissipated by the system in the form of radiated waves. Other ways of energy dissipation, such as viscosity or eddy shredding, is neglected. In general the radiation damping is sufficient to determine the body motions of the vessel. For the roll motion this radiation damping nonetheless does not capture the actual roll damping [38]. The first step to a better approximation of reality is therefore to manually add roll damping to the system. Values for the roll damping were found using empirical and numerical models. For a container ship, the added roll damping factor is found to be approximately 5% of the critical damping [5]. This damping factor is also used for the configuration used by Peña, also concerning a container ship. For a typical derrick barge without bilge keels, a total damping factor of approximately 17% was found for zero forward speed. A different estimation of the roll damping for different barges found an additional damping value between 8% and 11% of the critical damp-

ing [13]. It is expected that a square-shaped barge will require more additional damping than a container vessel. Based on these previous studies an additional roll damping value of 10% the critical roll damping will be added to the system. The sway and heave RAOs including this 10% added roll damping are given in Figure 4.5 and 4.6 for head waves and different barge distances.

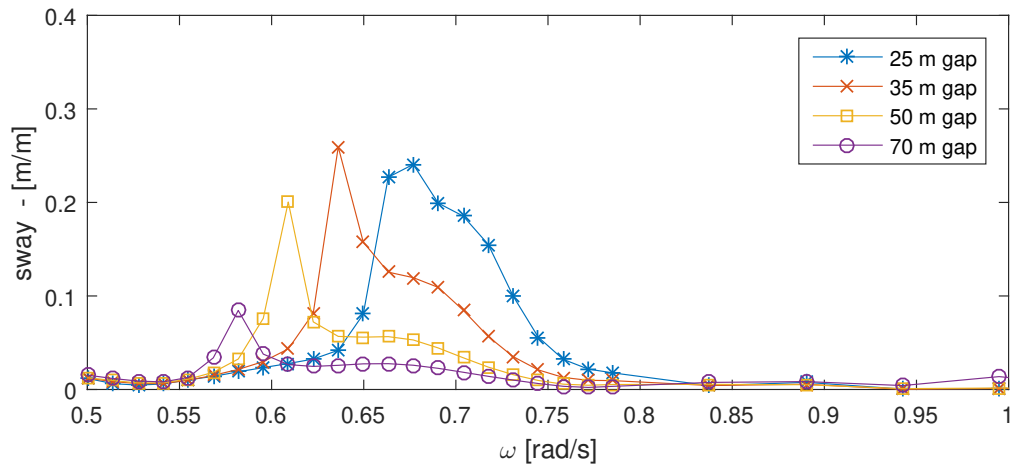


Figure 4.5: Sway RAO calculated with Aqwa for the base case, head waves, 10% added roll damping

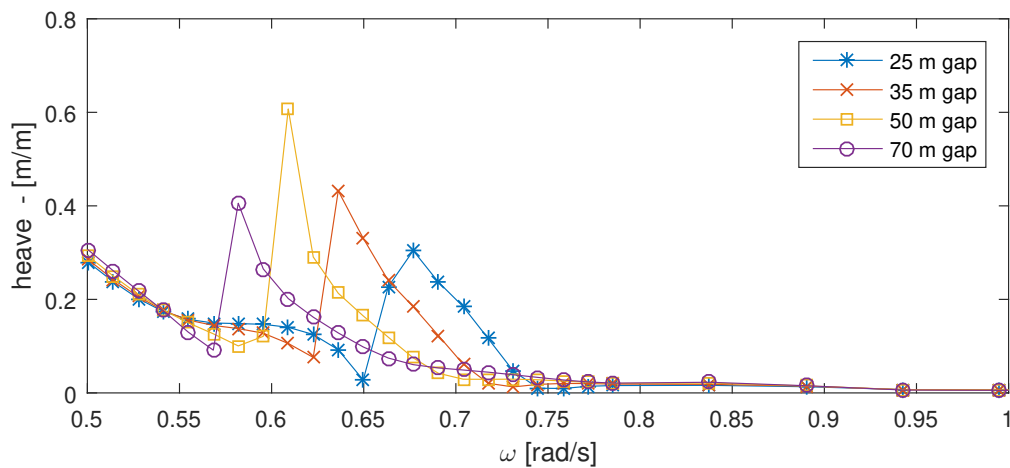


Figure 4.6: Heave RAO calculated with Aqwa for the base case, head waves, 10% added roll damping

It can be seen that the peaks in the RAO's are reduced due to the added roll damping. The peaks yet remain visible, even for gap sizes up to 70m. It is expected that this will not be the case in reality, as the viscous effects would damp out standing waves for such a distance between the vessels. Therefore another method is proposed to deal with these effects.

4.3.2. EXTERNAL DAMPING LID

The additional roll damping already results in a decrease of the standing wave effect and thus the peaks in the RAOs. Still the peaks remain visible at the resonance frequency. The method used by Fournier and Peña to cope with the remaining effects of the standing waves is the implementation of a flexible external damping lid. CHEN introduced a flexible lid by including a damping term in the free surface boundary conditions [6]. The free surface boundary condition used in potential theory as discussed in Appendix B without damping lid is given as:

$$-\omega^2\Phi + g\frac{\partial\Phi}{\partial z} = 0 \quad \text{for } z = 0 \quad (4.5)$$

With damping lid method of Chen this equations changes into:

$$(i\epsilon - 1)\omega^2\Phi + g\frac{\partial\Phi}{\partial z} = 0 \quad \text{for } z = 0 \quad (4.6)$$

ANSYS Aqwa has the option to define such a damping lid using a variation on the method proposed by Chen [2]. The method used within Aqwa also takes into account the gap size, which it uses to calculate the first sloshing mode ω_0 . In this way more damping is applied at the sloshing mode frequency. The method used by Aqwa is given by equation 4.7.

$$\frac{\omega^2}{g} \left[\epsilon^2 F\left(\frac{\omega}{\omega_0}\right) - 1 \right] \Phi - 2i \frac{\omega^2}{g} \epsilon F\left(\frac{\omega}{\omega_0}\right) \Phi + \frac{\partial\Phi}{\partial n} \quad (4.7)$$

with

$$\omega_0 = \sqrt{\frac{\pi \cdot g}{GAP}} \quad (4.8)$$

Furthermore $F(x)$ represents an attenuation function of the damping which reaches its maximum value of 1 at $\frac{\omega}{\omega_0} = 1$. The Aqwa reference manual suggest a damping ratio ϵ between 0 and 0.2; 0 meaning no damping, 0.2 meaning a lot of damping [2]. Peña calculated the added mass and damping for different values of ϵ (Figure 4.7). For the gap of 36m, it can be seen that the added mass becomes highly negative around a frequency of approximately 1.35rad/s. For the same frequency the damping shows an extraordinary increase. The increase of the damping factor ϵ results in a decrease in this peak. Besides that the 54m gap also shows significant variations in the added mass and damping. Increasing the gap width does not necessarily decrease these resonance effects. The question remains what the 'correct' damping factor should be. One of the findings is that there is no rational visible when changing the damping factor or the gap distance. The best way to determine the damping factor therefore is to compare the numerical findings with experiments.

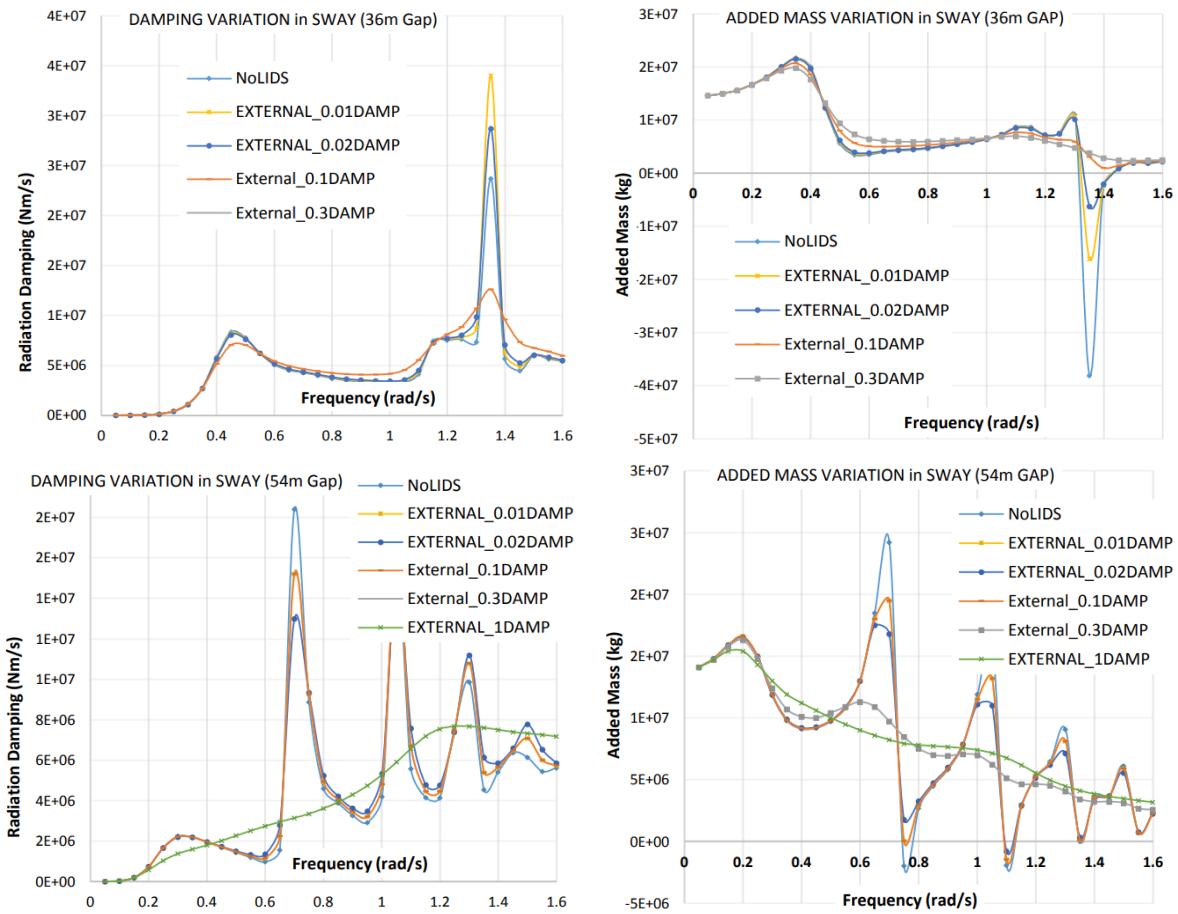


Figure 4.7: Damping and added mass for a container vessel next to a quay-side [32]

Supplementary to Peña, Fournier therefore includes experimental results to his research. He then tunes the value of ϵ to let the numerical results agree with the experimental results. His research concludes that for his side-by-side LNG Carrier configuration with a gap of $25m$, $\epsilon = 0.1$ gives good results (Figure 4.8).

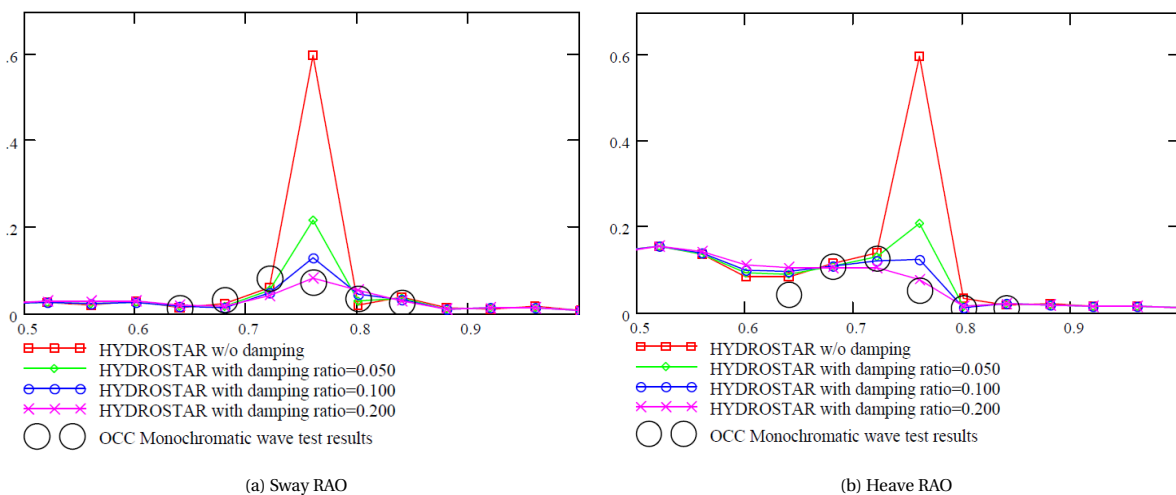


Figure 4.8: RAOs OCC experiment vs. HYDROSTAR software for different ϵ . [17]

Note the similarities of the RAOs with $\epsilon = 0$ with respect to Figures 4.5 and 4.6. In those graphs a similar resonance behaviour is visible in comparison with the values found by Fournier. The scaled model tests performed by him show that these numerically calculated peak values are much smaller in reality. The method proposed by Peña and Fournier is therefore adopted; a damping lid will be added to the system.

As there are no experimental results available, the damping factor will be chosen such that the results are similar to the experimental results of Fournier. The damping value ϵ will therefore be increased until the resonance peaks are filtered out. The results of that exercise are shown in Figure 4.9a and 4.9b.

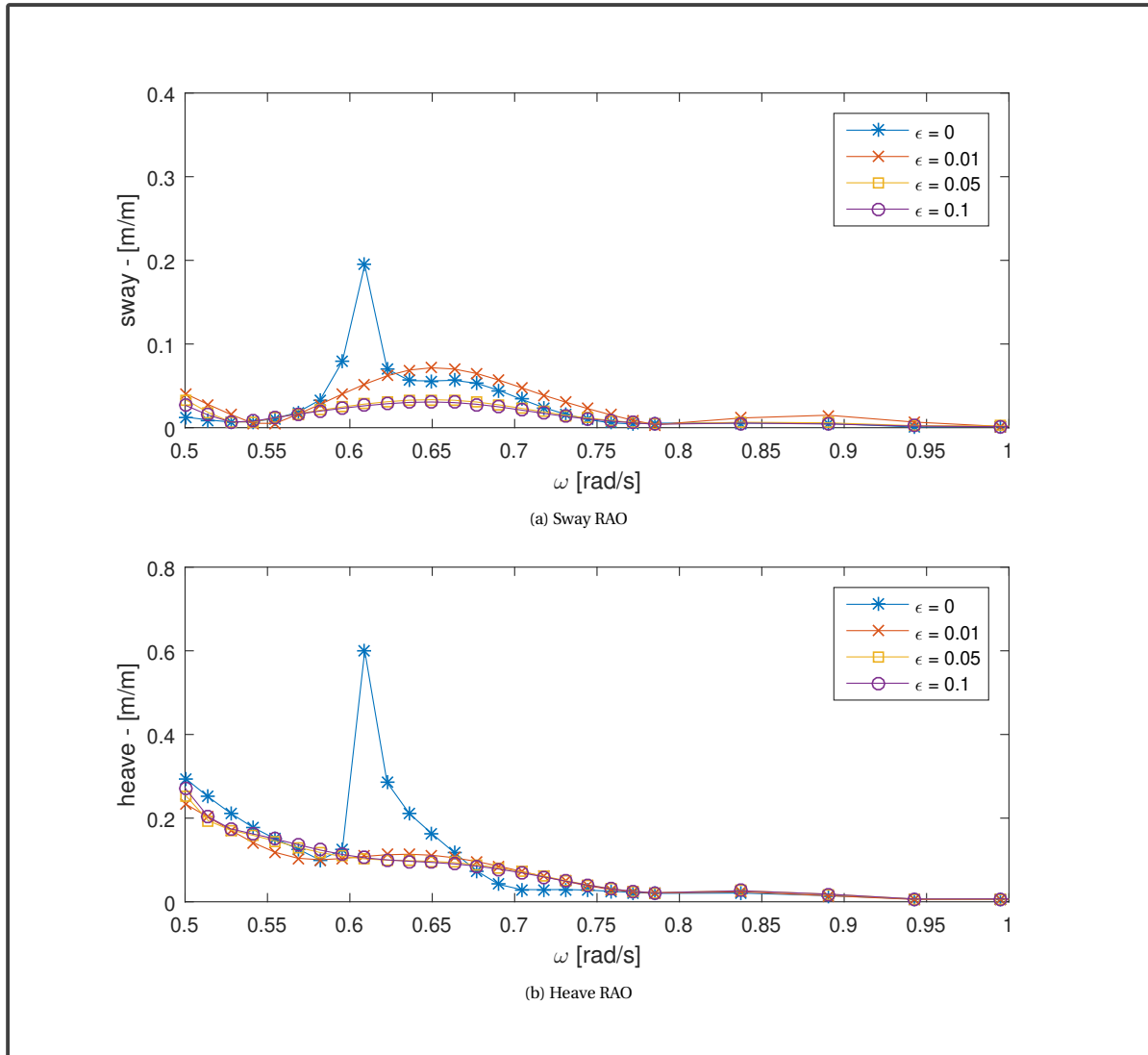


Figure 4.9: Sway and heave RAOs calculated with Aqwa, head waves, 10% added roll damping, gap = 50m

Additionally, the added mass and damping are shown in Figure 4.10 and 4.11 for different damping factors ϵ . The added mass and damping in sway direction shows big variations without damping lid. The lid seems to suppress these variations resulting in a more continuous development of added mass, damping and wave force, certainly for $\epsilon = 0.05$ and $\epsilon = 0.1$. An unexpected finding that the heave damping including the damping lid is much smaller than without damping lid for the lower frequencies (Figure 4.11). This happens while the added mass and wave force do not change for these lower frequencies.

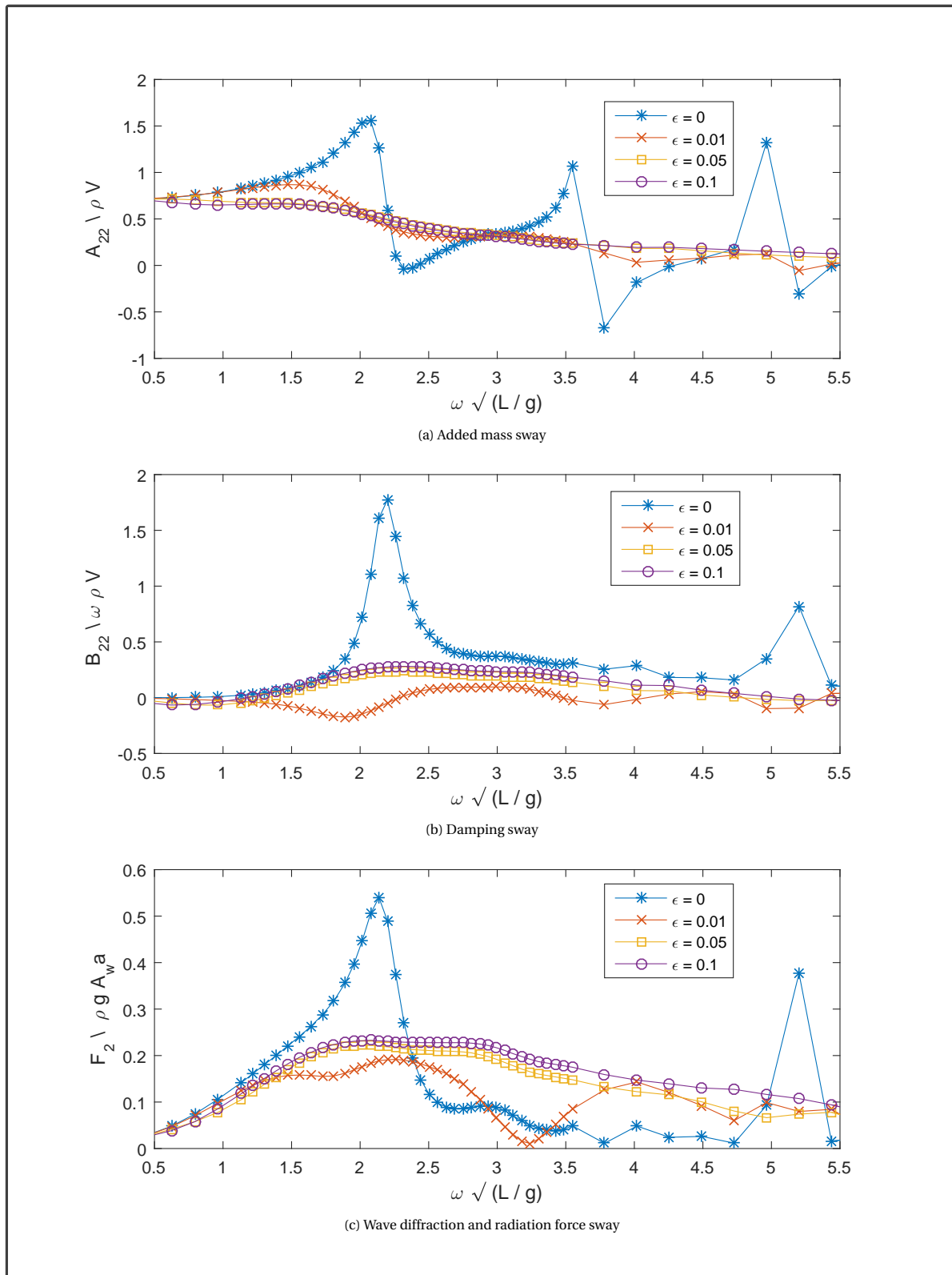


Figure 4.10: The effect of an external lid with different ϵ on the added mass(a), damping(b) and wave force (c) (beam waves) for sway direction for the base case scenario. The added mass is normalized by ρ times the volume V , damping is normalized by the ω times ρ times the volume V and the wave force is normalized by ρ, g , the water plane area A_w and the wave amplitude a .

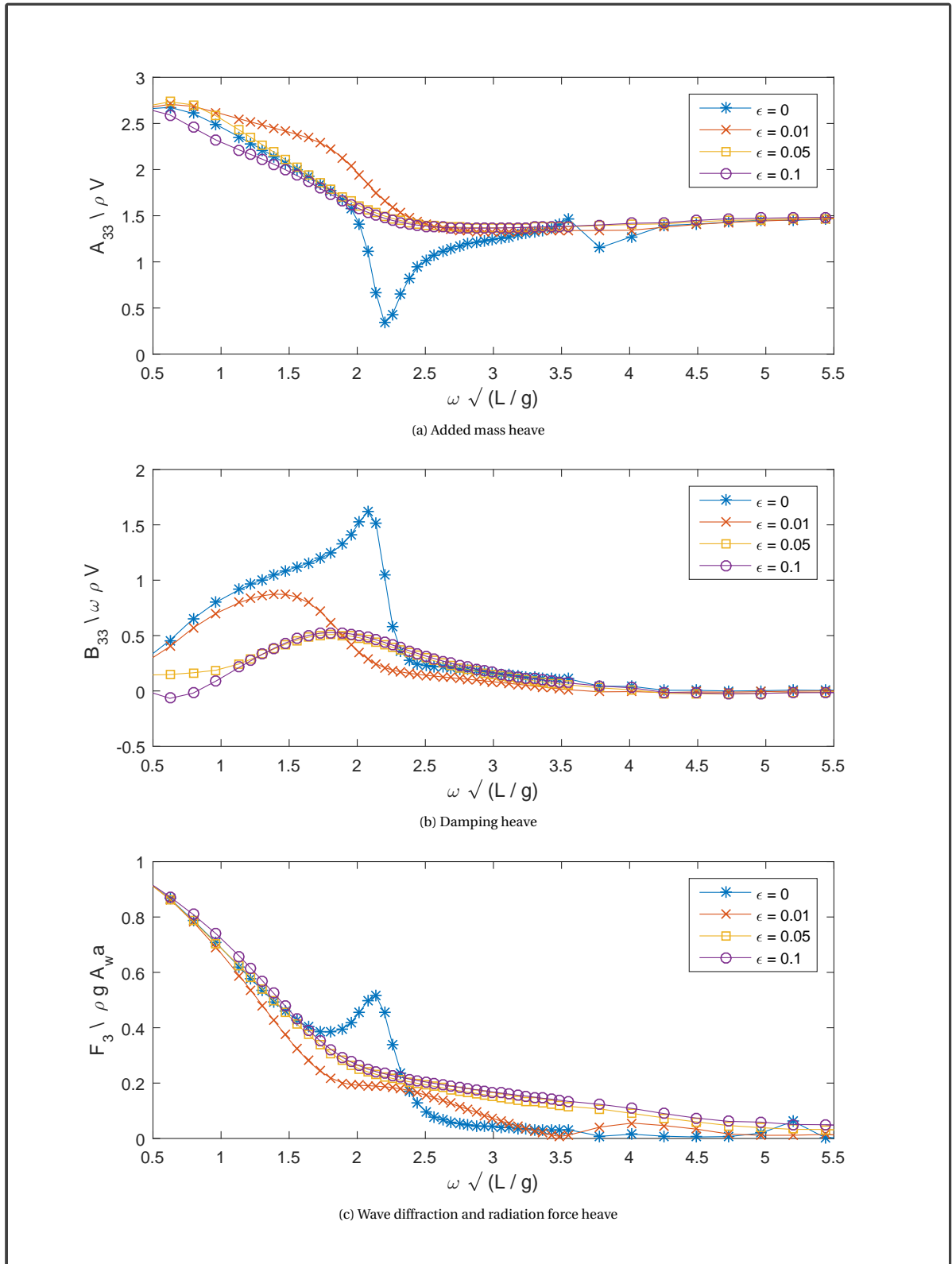


Figure 4.11: The effect of an external lid with different ϵ on the added mass(a), damping(b) and wave force (c) (beam waves) for heave direction for the base case scenario. The added mass is normalized by ρ times the volume V , damping is normalized by the ω times ρ times the volume V and the wave force is normalized by ρ , g , the water plane area A_w and the wave amplitude a .

Note also the negative damping occurring in Figure 4.10b and Figure 4.11b for the damping values of $\epsilon = 0.01$

and 0.1 respectively.

4.4. EFFECT OF THE DAMPING LID ON THE UNCOUPLED BARGES

The inclusion of additional damping results in the smoothing of the RAOs at the frequency of the standing waves. Additionally changes in the RAOs are observed away from these frequencies that are of interest. Figure 4.12a shows the heave RAO for the barge first encountering the beam waves for different ϵ . The results are as expected; the resonance peak is filtered out by the damping lid and the heave RAO decreases slightly with increasing ϵ . Figure 4.12b shows the same information but now for the other barge, shielded by the first barge. The graph shows an increased heave RAO for increased ϵ .

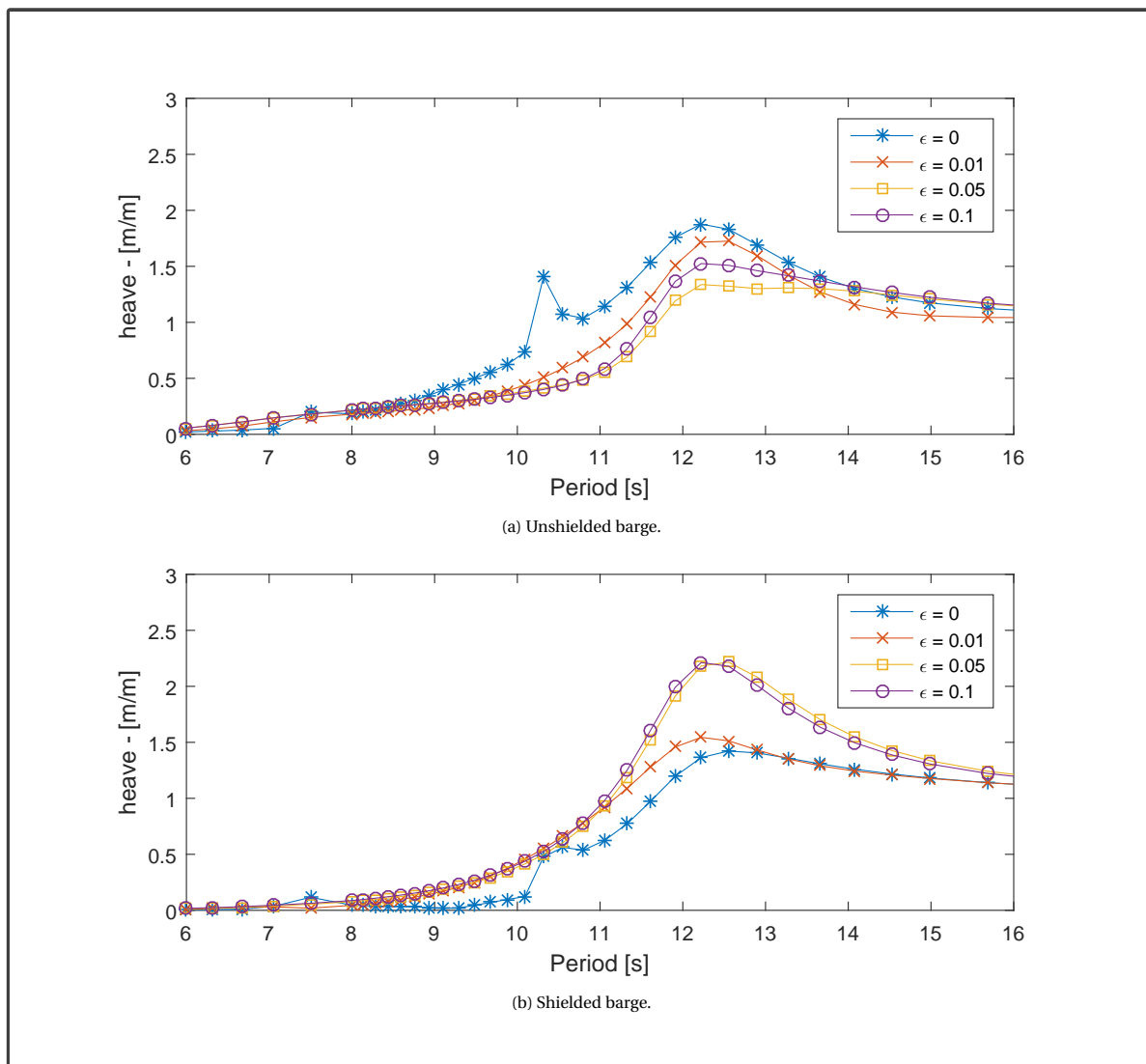


Figure 4.12: Heave RAO uncoupled barges for different values of ϵ in beam waves.

It is difficult to find a rational to explain why this happens. The damping of the wave elevation between the barges results in increased RAOs. When looked at the roll RAOs in Figure 4.13a and 4.13b it can also be seen that the RAOs slightly increase for both the shielded and unshielded barge.

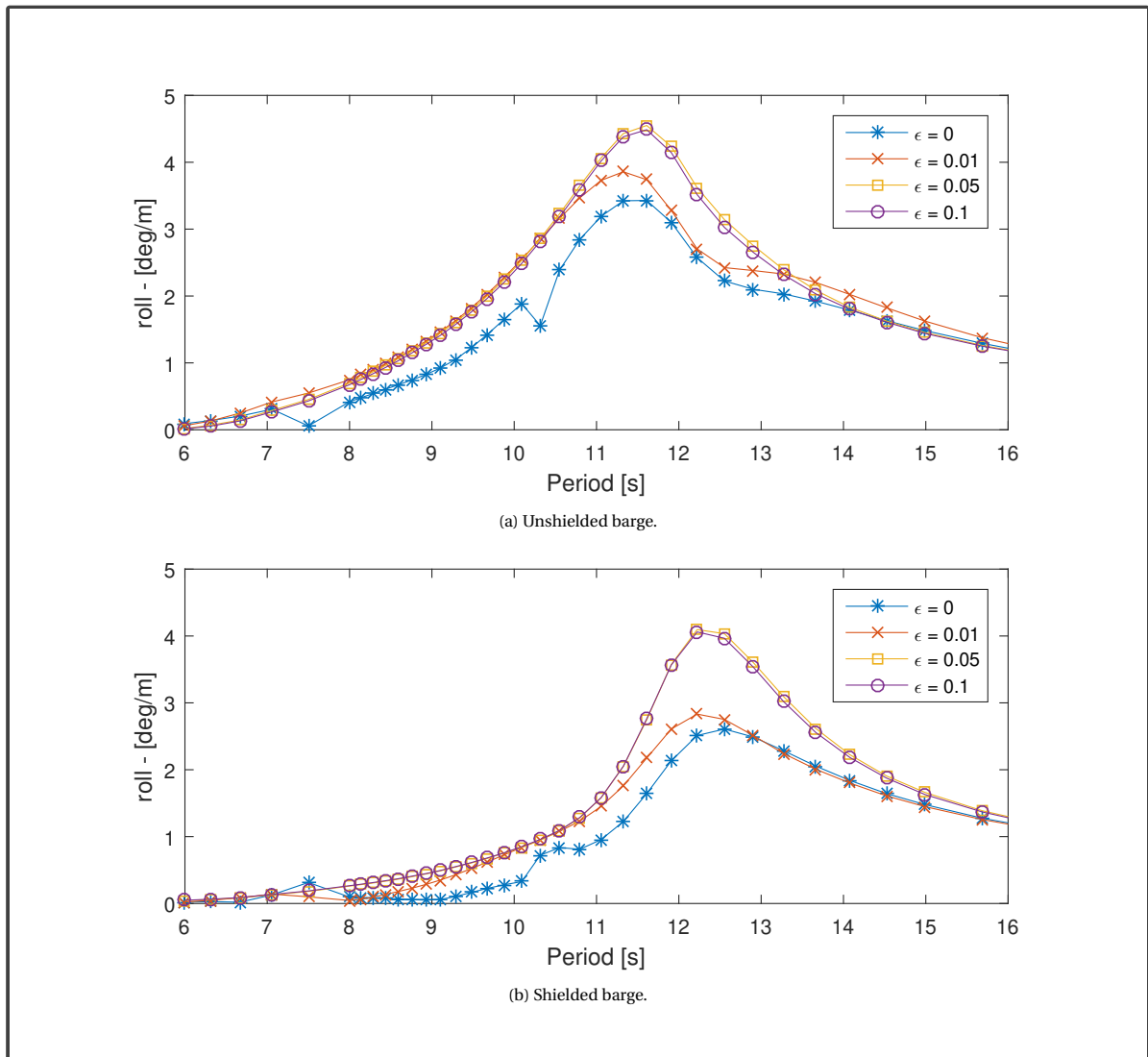


Figure 4.13: Roll RAO uncoupled barges for different values of ϵ in beam waves.

4.5. EFFECT OF THE DAMPING LID ON THE COUPLED BARGES

Heave RAOs are also calculated for the connected barges. For a damping lid with $\epsilon = 0.01$ the heave RAO increases beyond any physical reason up to 7 m/m for the unshielded barge as can be seen in Figure 4.14a. For $\epsilon = 0.1$ and $\epsilon = 0.05$ the RAOs seem to converge to more realistic values. Furthermore the peak in the heave RAO with $\epsilon = 0$ is successfully filtered out using a damping lid with a small amount of damping.

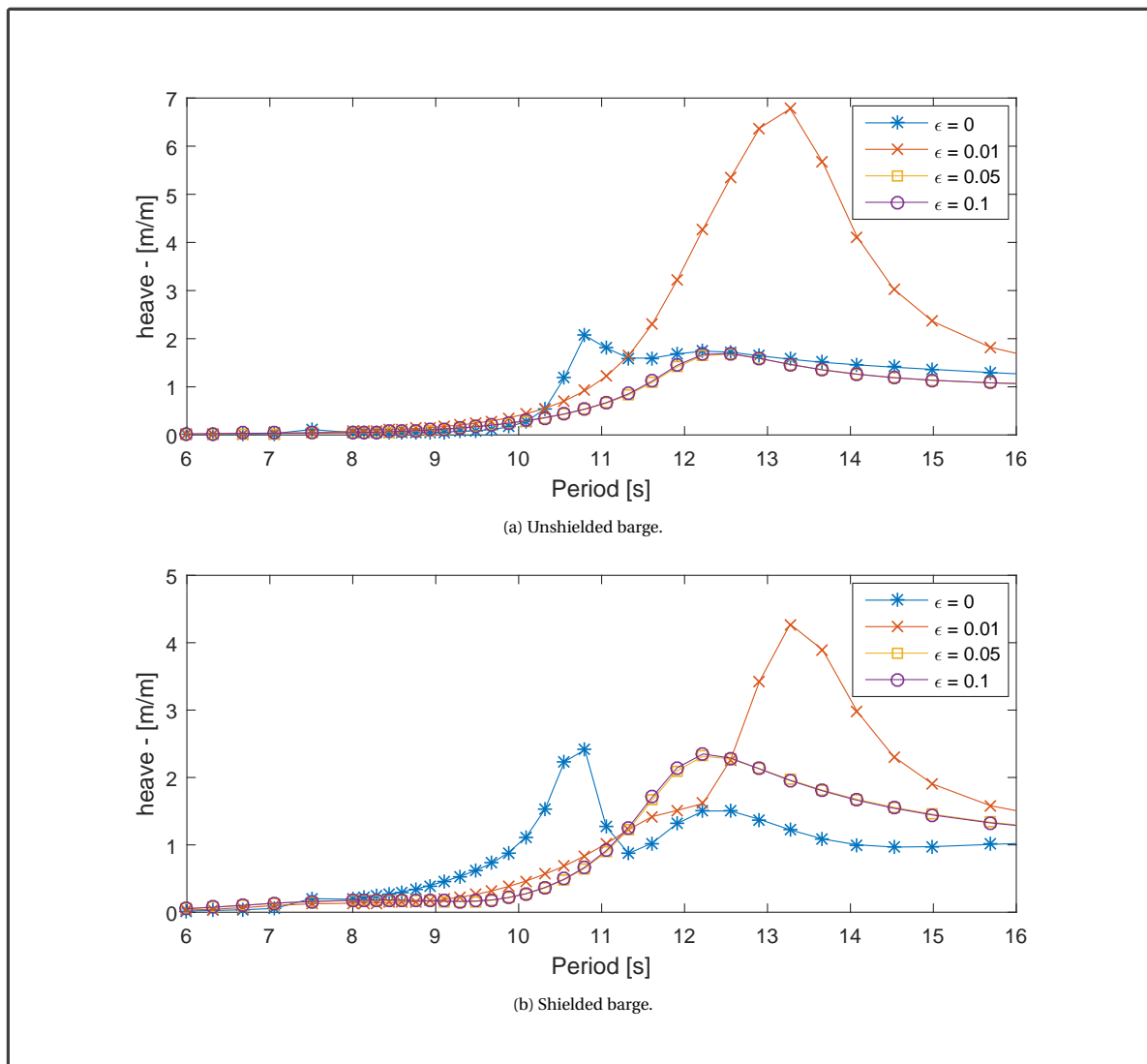


Figure 4.14: Heave RAO coupled barges for different values of ϵ in beam waves.

4.6. DISCUSSION EXTERNAL LID

The exercise of including an external damping lid shows that it can be used to suppress the standing waves that occur in between the barges. A small amount of damping already results in significant decrease of the occurring resonance. On the other hand the exercise proves one of the conclusions of Fournier, i.e. that no rationale could be found in predicting the most appropriate damping factor before hand. He states the following: *"It is noteworthy that the HYDROSTAR and WAMIT methods both apply damping at the free surface that is away from where the dissipation actually takes place (i.e. near the bilge keels and the vessel walls owing to friction)"*[17]. In the previous exercise it is shown that the damping lid even tends to increase the motions for lower frequencies.

The damping lid can be used as a tool to suppress standing waves, but one has to be very careful with the outcome. A damping lid with $\epsilon = 0.05$ results in RAOs similar to the results discussed by Fournier. It seems unnecessary to increase the value further to $\epsilon = 0.1$; the RAOs for both values are almost equal. Therefore the value of $\epsilon = 0.05$ will be used to damp out the resonance in between the barges. This amount of damping will be used regardless of the change in gap distance. It is very well understood that this solution is not optimal; there is no real evidence that the results should match the results of Fournier. On the other hand, occurrence of standing waves in between floating bodies and how to deal with it is widely discussed in previous studies and the use of a damping lid is an accepted solution [17] [32] [31] [6]. A better approximation of the results

can be made by performing model tests with the configurations discussed in this research. This lies outside the scope of this thesis and might be a subject for future research. An external damping lid with damping factor $\epsilon = 0.05$ and 10% added roll damping will therefore be used in the following calculations.

4.7. CHAPTER REVIEW

In this chapter the hydrodynamic behaviour of the barges is discussed. ANSYS Aqwa is used to calculate the hydrodynamic parameters, after which the RAOs can be determined. In the outcome peculiar peaks are observed in the graph of the RAOs. Literature shows that these peaks can be the consequence of numerical errors in the software at the so called irregular frequencies. The first proposed solution is to include an internal lid in the ANSYS Aqwa calculation. This only has a minor influence on the results. Another reason for the peculiar peaks can be the underestimation of the damping. Previous studies show that it is reasonable to include an additional roll damping of 10% when dealing with rectangular barges. Still the peaks remain visible to some extent when this additional roll damping of 10% is added to the system.

Earlier research on the topic of side-by-side moored vessels shows that the occurrence of these peaks is the consequence of a standing wave effect in between the vessels. Experiments performed by Fournier, on a similar configuration of side-by-side moored LNG-carriers, shows that the hydrodynamic software overestimates these peaks. The proposed method to deal with this is the use of an external damping lid. The underestimation of nonlinear damping such as viscous damping or vorticity is opposed with an artificial damping term applied at the free surface between the barges. In this way unrealistic wave elevations can be reduced.

The external lid method shows no explicit rationale for different damping values. It is difficult to determine the correct value for the damping based on calculations. Scaled model test should be performed to validate the correct damping value. Because this lies outside the scope of this thesis, the damping value will be based on the experiments of Fournier. The damping value is chosen such that the RAOs are similar to those of Fournier. This results in a damping value of $\epsilon = 0.05$. Further calculations will be performed with this damping value. Additionally a roll damping of 10% will be added to the system.



F I V E

P A R A M E T R I C S T U D Y

In this chapter the input required for the parametric study is obtained and discussed. The necessary output and limiting parameters are touched upon and the method used to come up with the results is explained. The parametric study is performed in two stages. In the first stage each of the parameters is changed separately to say something about the sensitivity of each parameter. In the second stage the influence of the barge gap/width ratio is examined and the optimal vessel dimensions are chosen.

5 | Parametric sensitivity study

5.1. WAVE DATA INPUT

To calculate the motions of the vessels, a wave spectrum has to be defined. Many different wave spectra exist. The Pierson-Moskowitz spectrum represents fully developed sea states. The JONSWAP spectrum was developed during the Joint North Sea Wave Project and additionally includes a peak enhancement factor to be more suited for developing seas [18]. This spectrum suits the conditions in the North Sea the best and will therefore be used (Figure 5.1). The input needed for the JONSWAP spectrum is the significant wave height, the peak enhancement factor and the peak period. When the RAOs are used to calculate the response, the system is linear and the vessel motions will therefore increase linearly with the wave height. The significant wave height will therefore be normalized to 1 meter for all calculations. The mean peak enhancement factor is taken as 3.3 [18]. The peak period depends on the location in the North Sea, but also the time of the year. Summer sea states are in general more calm than in winter. Shorter wave periods and wave heights can be expected. Within Allseas, hindcast meteocean data is made available on the location of the Brent Delta platform in the northern North Sea which can be found in Appendix C [33]. Additionally the annual and summer wave count scatter diagrams are extracted from the data report for the Brent Delta location based on measured data between March 1973 and December 2006 (Figure 5.2 and Figure 5.3).

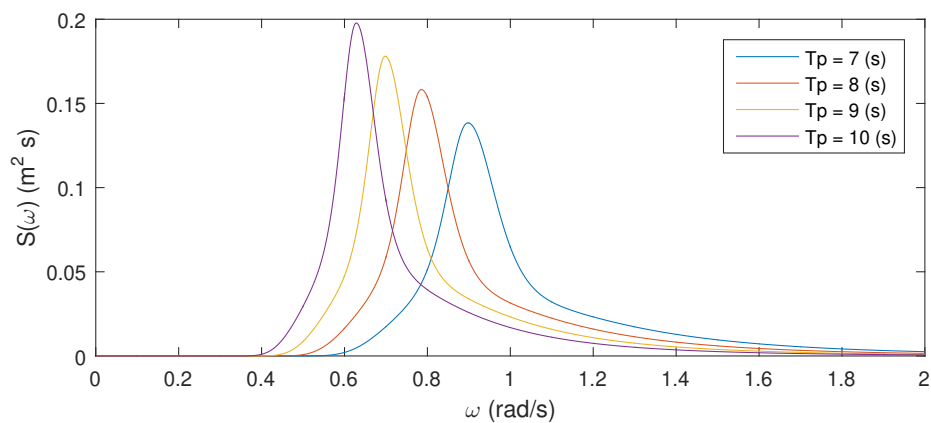


Figure 5.1: Jonswap energy density spectrum for different peak periods T_p and $H_s = 1 m$

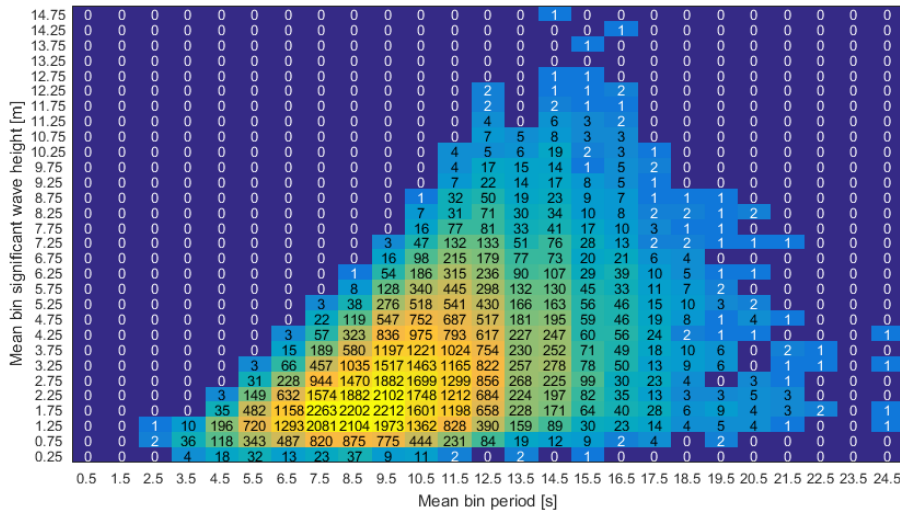


Figure 5.2: Wave count Brent Delta annual

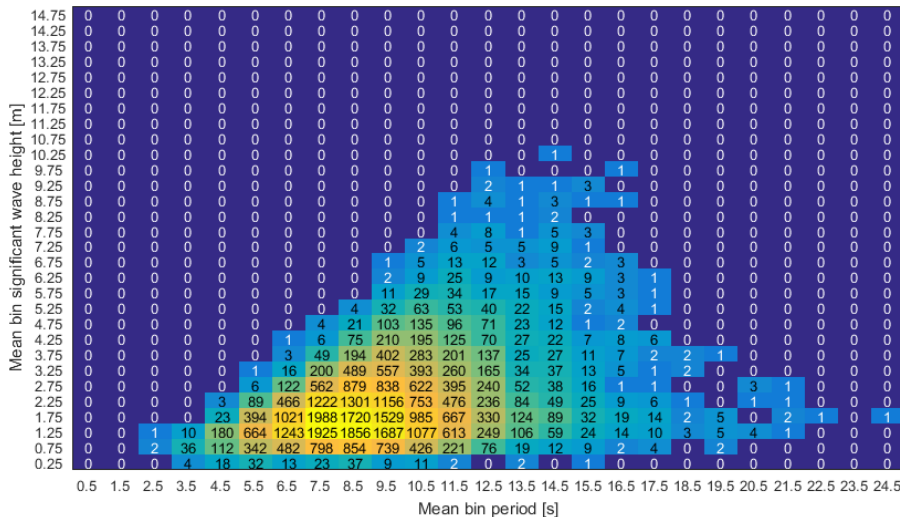


Figure 5.3: Wave count Brent Delta April to September

Comparing the annual and summer wave count, it is clear that in summertime the number of high waves counted is less and the periods are in general shorter. The ambition is to be operational in conditions with significant wave heights between 2 and 3m. Therefore, based on this hindcast data, the calculations will be performed using a JONSWAP spectrum with peak periods of seven, eight and nine seconds, the most occurring periods corresponding to these significant wave heights. The wave directions will be equally divided between -180° and 180° with a step size of 30° . The JONSWAP spectra will be applied for each wave direction independently. Additionally the total scatter diagrams will be used to calculate the annual and summer workability of the decommissioning concept.

5.2. BARGE DIMENSIONS

The parametric study will be performed for the following range of parameters:

- **Length** from 150m to 275m with stepsize of 25m
- **Width** from 40m to 70m with stepsize of 5m

- **Draught** from 10m to 25m with stepsize of 2.5m
- **Distance** from 25m to 70m with stepsize of 5m

The dimensions of the barges are based on the existing barges discussed in Section 2.5. Additionally the distance between the barges is based on the most extreme platforms in the North Sea, discussed in the same section. The parameters are changed separately around the base case configuration. First only the length will be adjusted, then the width and so on. The goal is to find a relation between the different parameters and the motions of the vessels. This will result in information necessary to perform the next calculation run. If the motions are proven to be more sensitive to one parameter than another, it will be more effective to change the most sensitive parameter. Each configuration requires approximately twenty minutes calculation time. In this way, the calculation does not have to be performed for all different parameter sets possible, saving calculation time.

5.2.1. LIFTING POINT

The position of the lifting point is needed to say something about the vertical motion and thus the impact velocity between the lifting point and the topsides. The location of the lifting point should be taken with respect to the centre of gravity of the barge. The location is assumed to be fixed at a vertical distance of $z_{lp} = 25m$ with respect to the mean sea level (MSL). Additionally the x-coordinate will be taken as $x_{lp} = 50m$ with respect to the centre of gravity of the *topsides*. These coordinates can directly be translated to the coordinates of the lifting point with respect to the centre of gravity of the *vessel*. For the y-coordinate it is assumed that the vessels can move as close as five meters from the lifting point. Depending on the width of the vessel this means that the y-location of the lifting point is given by $y_{lp} = 0.5 \cdot width + 5$. This means that the lever arm of the vertical motion increases with the increase of the width of the barges. All coordinates are based on the conceptual design and the information on platforms presented in chapter 2.

5.3. METHOD OF THE PARAMETRIC STUDY

Aqwa-line uses a .DAT file as input file. This is a text file containing the mesh information, structural properties of the system and the wave frequencies and directions for which the motions should be calculated. The Aqwa Workbench environment is used to create such an input file for the base case configuration. To create an input file of a new configuration, this general file will be read out with Matlab. The meshing information will be stored as a matrix and can then be adapted to the new configuration accordingly. For example, if the length of the new configuration is 1.5 times the length of the general configuration, all the x-coordinates of nodes in the mesh will be multiplied with a factor 1.5. The same applies for the width of the barge and the y-coordinates together with the draught of the barge and the z-coordinates. The new mesh is then saved in the new text file. Finally the structural properties such as the mass and the mass moment of inertia are changed as well. The new input file can now be used as input for Aqwa.

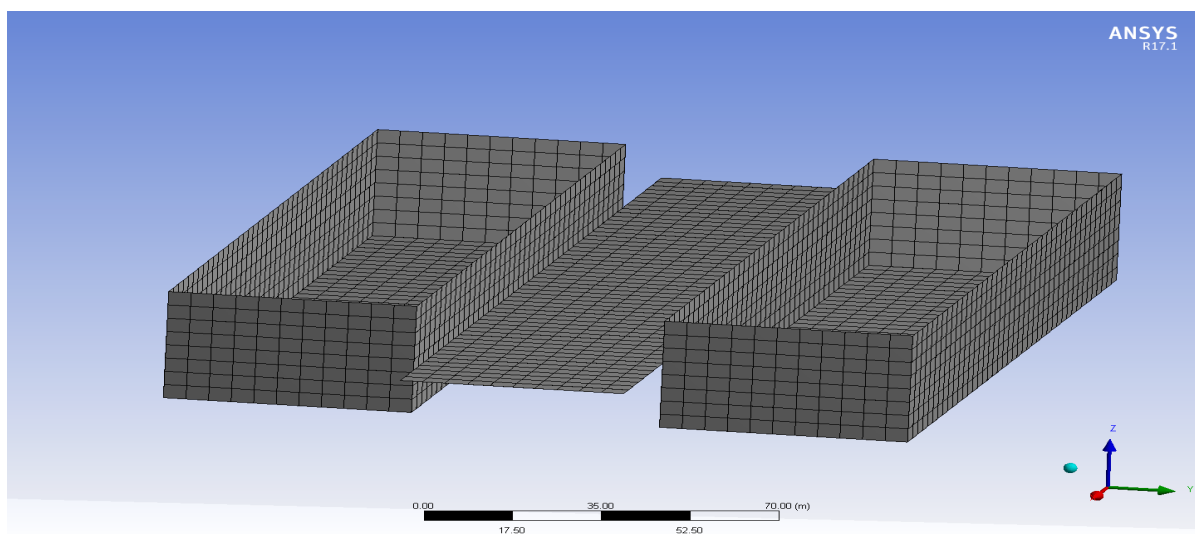


Figure 5.4: Ansys Aqwa mesh including damping lid.

5.4. VESSEL RESPONSE IN WAVES

The main indicator to the performance of the concept vessel will be the response to the incoming waves. The incoming waves are defined by a JONSWAP wave energy spectrum. This wave energy is defined in the following formula:

$$S_{\zeta}(\omega) \cdot d\omega = \frac{1}{2} \zeta_a^2(\omega) \quad (5.1)$$

To transform this wave spectrum to a response spectrum the wave amplitude is multiplied with the RAO of the motion [21, p.222]. For the heave (z) motion holds:

$$S_z(\omega) \cdot d\omega = \left| \frac{z_a}{\zeta_a}(\omega) \right|^2 \cdot \frac{1}{2} \zeta_a^2(\omega) = \left| \frac{z_a}{\zeta_a}(\omega) \right|^2 \cdot S_{\zeta}(\omega) \cdot d\omega \quad (5.2)$$

In words this means that the wave spectrum should be multiplied with the RAO squared to get the response spectrum. To say something about the maximum motion the most probable maximum (MPM) will be determined. Given that the wave amplitudes are Rayleigh distributed the MPM is calculated using equation 5.3 [21, p.432].

$$\zeta_{a_{max}} = \sqrt{2 \cdot m_{0\zeta} \cdot \ln(N)} \quad (5.3)$$

where $m_{0\zeta}$ represents the area underneath the graph of the response spectrum and N represents the number of oscillations in a given timespan. The latter is usually taken as three hours, the approximate timespan in which a sea state remains constant. N can now be calculated by dividing the timespan by the mean zero crossing period of the motion. The most probable maximum can now be calculated to give an indication of the performance of the concept.

5.5. FIRST STAGE PARAMETRIC STUDY: RESULTS

The results are presented in the form of a rose plot. In the rose plots the output criteria is plotted as a colour, against the concerned variable along the radius of the plot. This is done for all different wave directions. Values in between the calculated directions and dimensions are interpolated using a cubic interpolation method within MATLAB. For each wave direction a JONSWAP spectrum is applied with a significant wave height of $H_s = 1m$. The angles indicate the direction from which the wave is coming. The output criteria is given as the MPM amplitude during a three-hour sea state with this wave spectrum. Additionally a topside view of the barges is given in the centre of the plot, including the position of the lifting point for which the output criteria is calculated, indicated with the red dot. As example Figure 5.5 shows the rose plot of the MPM vertical motion of the lifting point as function of the vessels' width. The width changes from 40 to 70m along the radius of the rose plot. The other barge dimensions remain the same as for the base case scenario.

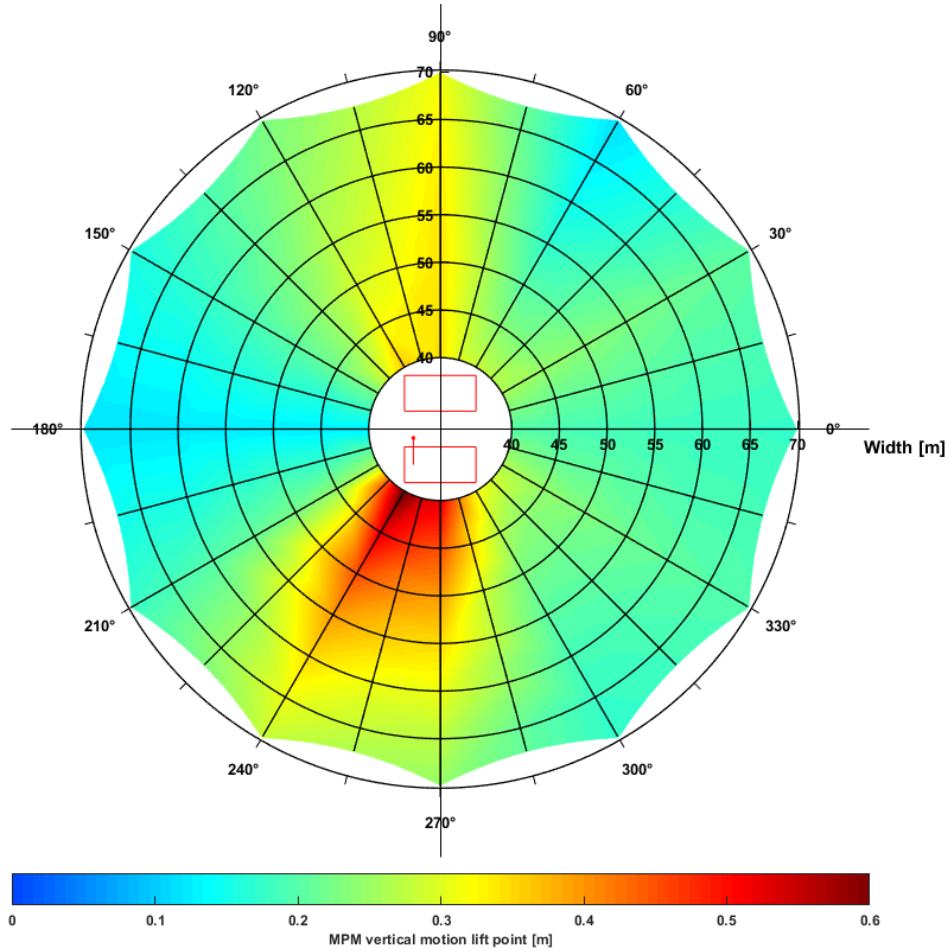


Figure 5.5: MPM vertical lift point motion per wave direction for the coupled barges as function of vessel's width for $T_p = 9s$.

In the figure it can be seen that the vertical motion of the lifting point is the biggest for small widths and incoming wave angles between 240° and 270°. At these wave angles an increase in width really tempers the vertical motion of the lifting point. When the waves are coming from an angle of 90° the vertical motion of the lifting point seems less sensitive to an increase of width. The rose plots of the other variables (again including the width) are given in Figure 5.6.

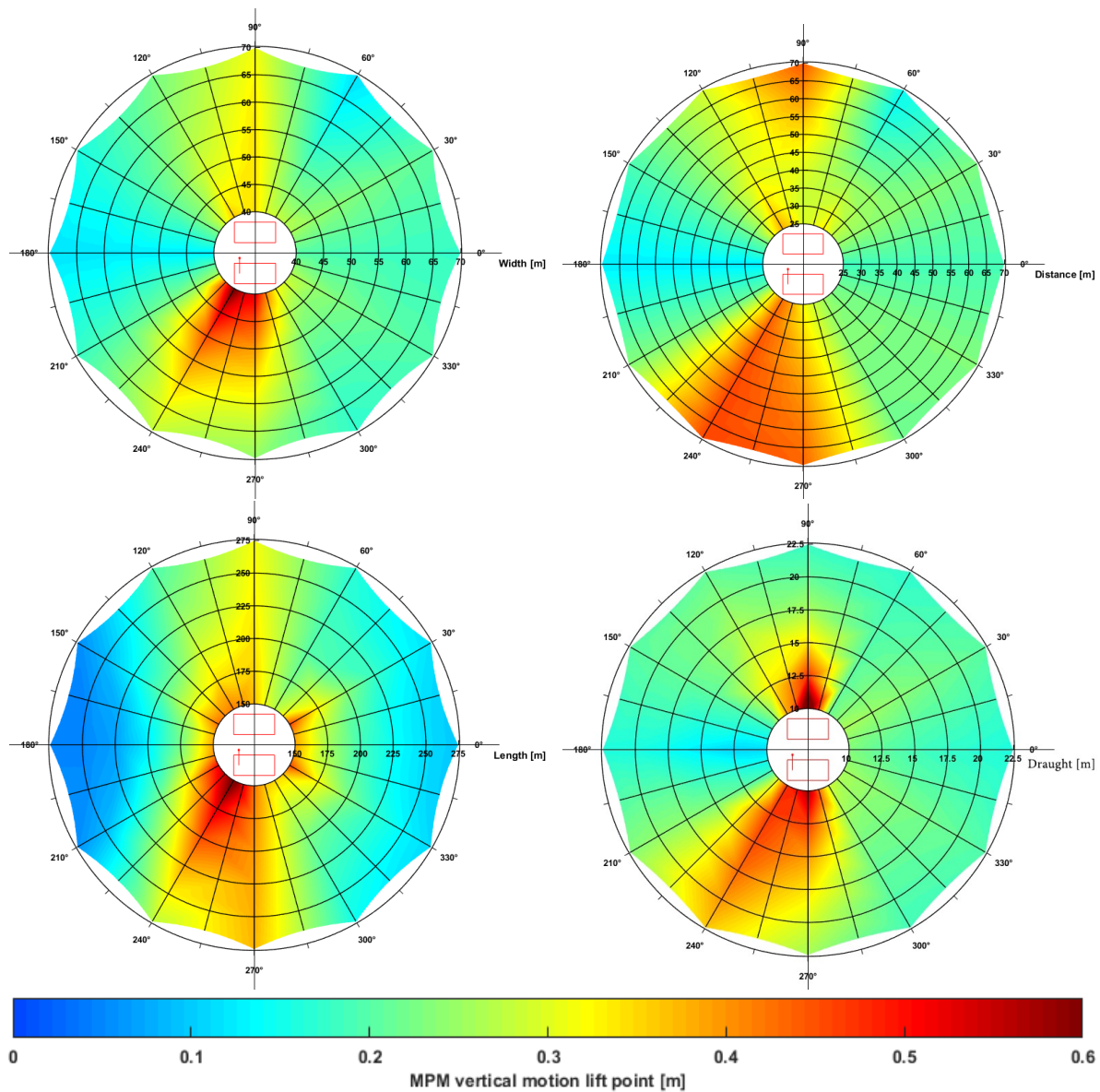


Figure 5.6: MPM vertical lift point motion amplitude per wave direction for the coupled barges as function of vessel's width, distance, length and draught for $T_p = 9$ s.

Additional to the width, the distance, length and draught rose plots are shown. An increase of distance in general does not have any effect on the vertical motion of the lifting point. However, for waves coming from 90° an increase in the vertical motion can be seen for a bigger distance between the barges.

A variation in length has the most effect on the vertical motion of the lifting point for waves coming from 0° and 180°. The length increase will decrease the pitch motion of the vessel for those wave directions and therefore decrease the vertical motion of the lifting point.

The variation of the draught shows more straightforward results. Increasing the draught results in smaller motions. Just as in the other plots the wave direction that results in the biggest lifting point motions is between 240° and 270°.

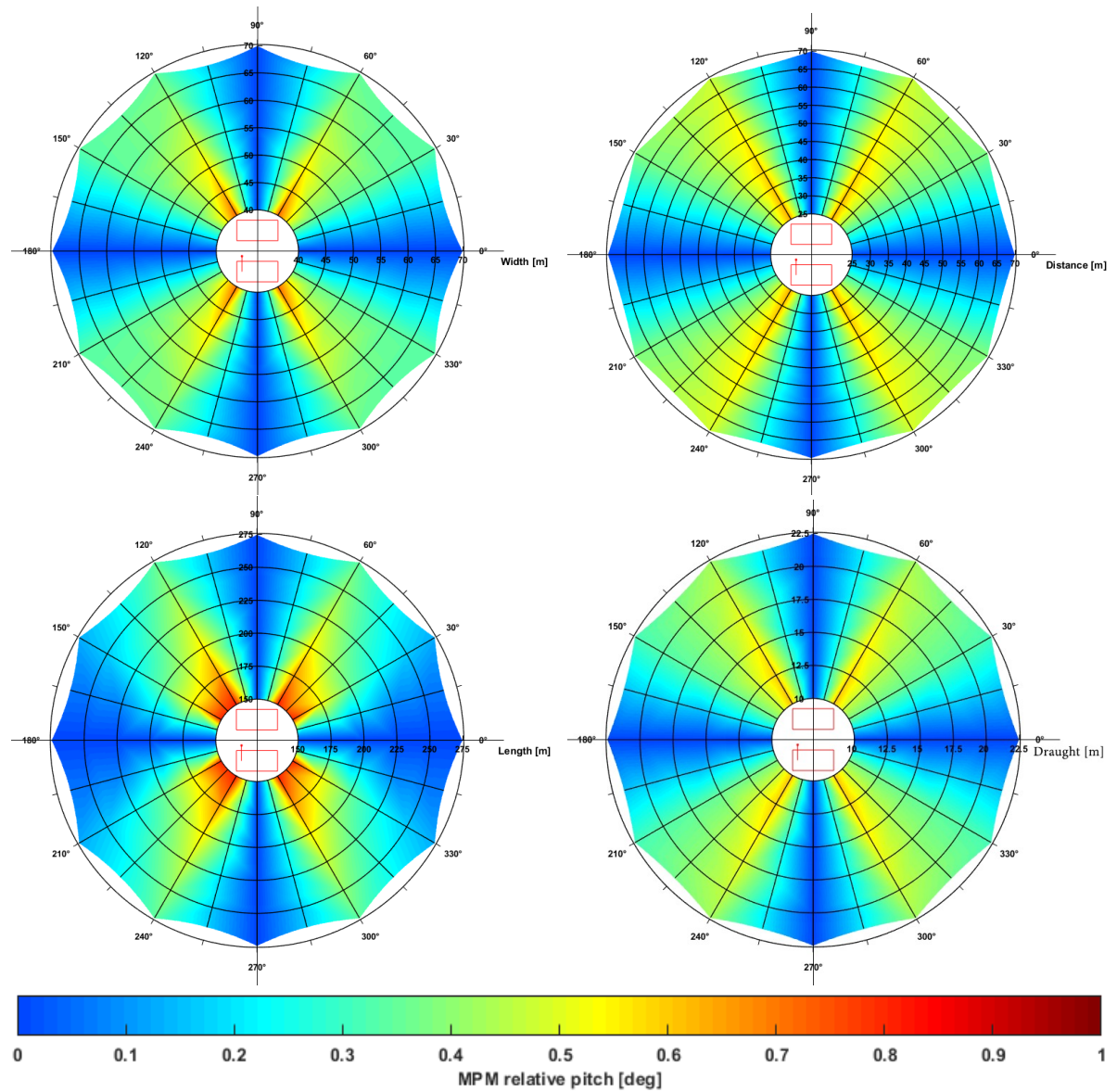


Figure 5.7: MPM relative pitch motion amplitude per wave direction for the coupled barges as function of vessel's width, distance, length and draught for $T_p = 9s$.

Figure 5.7 shows the rose plots for the relative pitch criteria. It can be seen that the criteria is the most sensitive to an increase of the length. For all the other parameters also holds that an increase of the parameter results in a smaller relative pitch. It has to be noted that the connections do not influence the relative pitch motion. The rose plots for the system without connections are identical.

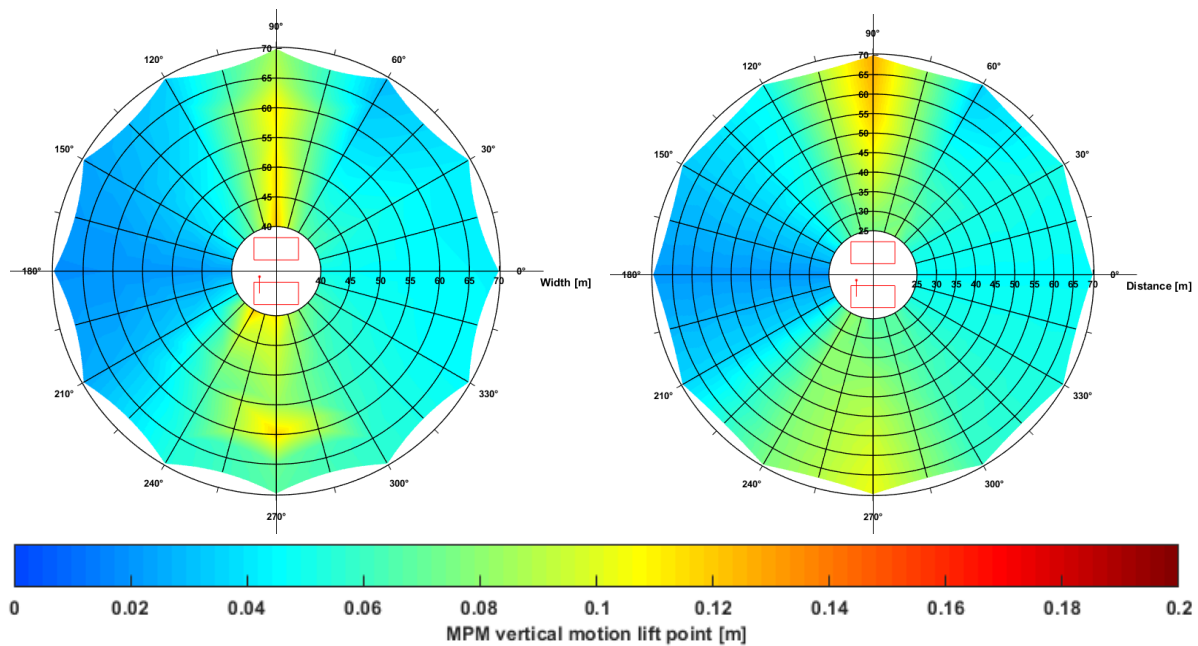


Figure 5.8: MPM vertical lift point motion amplitude per wave direction for the coupled barges as function of vessel's width and distance for $T_p = 7s$.

In Figure 5.8 again the MPM vertical motion of the lifting point is the given criteria but now for a wave spectrum with a peak period of $T_p = 7s$. Note that the range of the colour bar is now only one third of what it was for the plot with $T_p = 9s$. The comparison directly shows the influence of the different wave periods to the vessels' motions with longer periods resulting in larger motions. A noteworthy detail again is the visible peak for a wave direction of 270° and a width of around 60 meters. Also an increase in distance for a wave direction of 90° tends to increase the motions of the lifting point. Furthermore the pitch motion seems to have less influence on the vertical motion of the lifting point for $T_p = 7s$. Where the maximum motions were first to be found for oblique incoming wave of about 240° for $T_p = 9s$, now they are found almost exactly at beam waves.

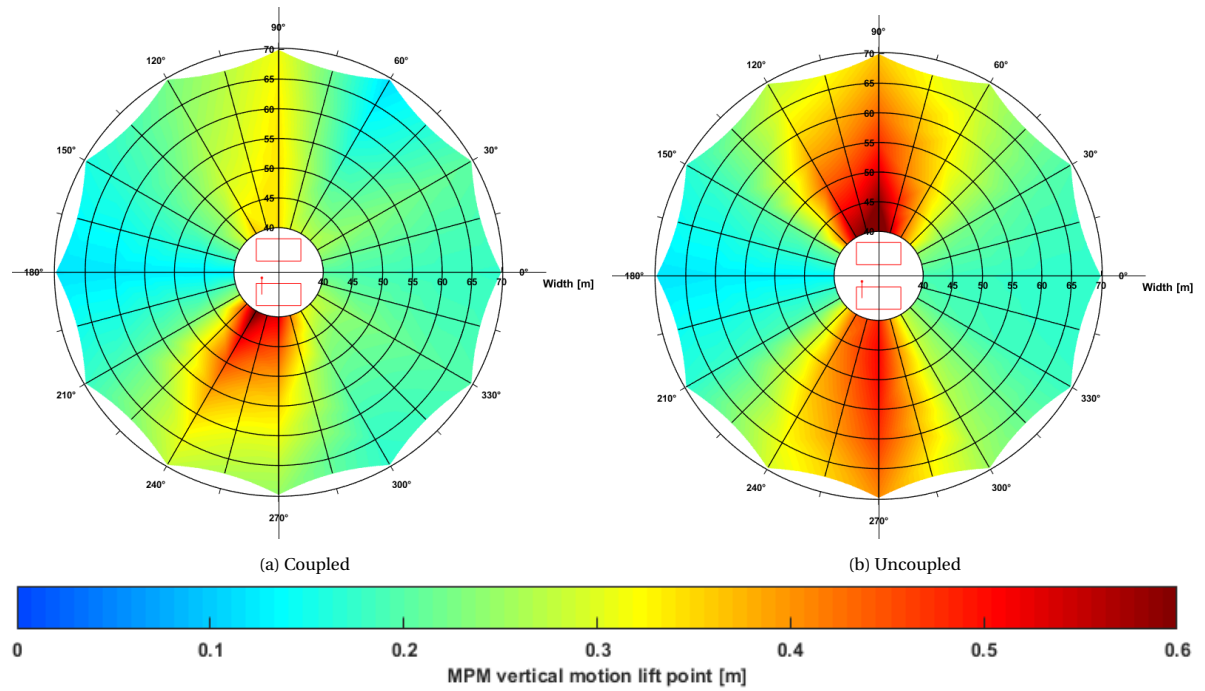


Figure 5.9: MPM vertical lift point motion amplitude per wave direction and as function of vessel's width for $T_p = 9s$.

In Figure 5.9 the difference between the barges with and without connections is made visible. It is directly obvious that the connections indeed decrease the motions of the vessel. Also noteworthy is the fact that for the uncoupled barges no shielding effect is present. The motions even seem to be larger when the waves are coming from a 90° angle. This effect is also discussed in section 4.4 and has to do with the influence of the external damping lid. In that section Figure 4.12b shows an increase in the heave RAO for the shielded barge in comparison with the unshielded barge.

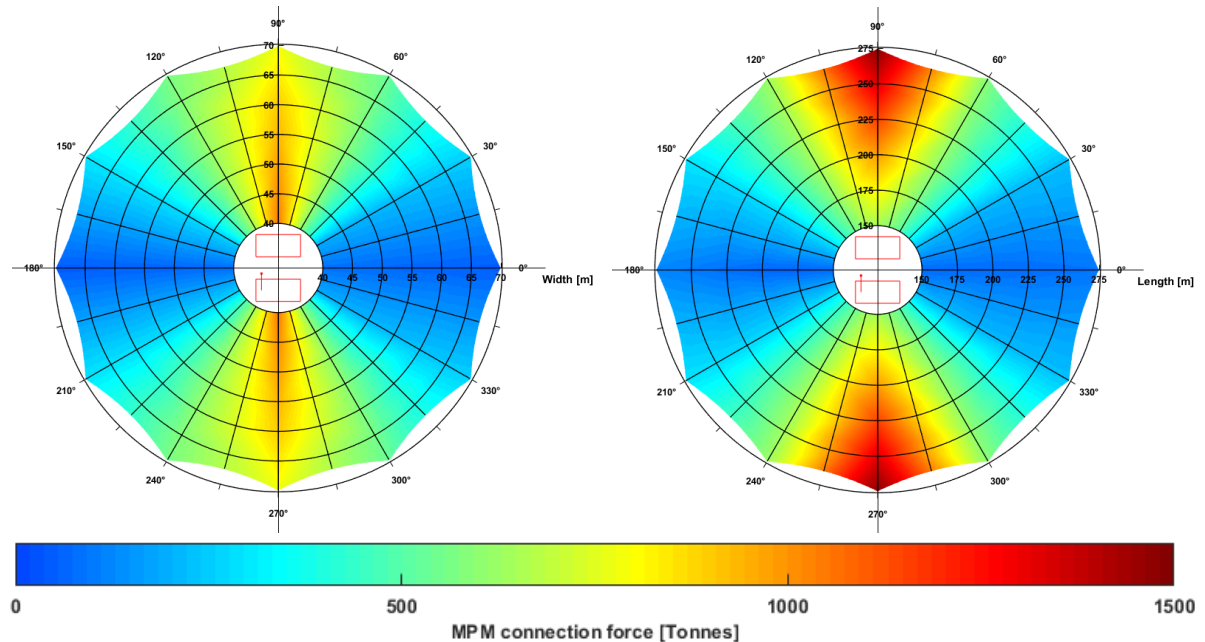


Figure 5.10: MPM connection force per wave direction and as function of vessel's width and length for $T_p = 9s$.

Figure 5.10 shows the rose plot of the connection force as function of the width and the length. The connections only prohibit relative roll, sway and surge so logically the forces are the largest when the vessel is subjected to beam waves. An increase in length results in a bigger body subjected to waves and therefore an increased overturning roll moment resulting in bigger forces in the connection beams.

5.5.1. FIRST STAGE PARAMETRIC STUDY: DISCUSSION

The focus of the results lies on what the most sensitive vessel parameters are and how they can be changed in order to improve the hydrodynamic performance of the vessel. Also the relation between the wave length, barge width and barge distance is of interest.

In general the motions of the lifting point remain below $0.5m$ amplitude for a JONSWAP wave spectrum with a significant wave height of $H_s = 1m$ and a peak period of $T_p = 9s$. An increase of the dimensions of the barges overall results in a decrease in vessel motions. For the relative pitch motion the increase of length has the most influence.

If the vessels are excited by a JONSWAP spectrum with $T_p = 7s$ the motions of the vessel decrease significantly. Another interesting result is the presence of a peak in the motions for a width between 60 and $65m$ and an incoming wave of 270° . Furthermore an increase in distance also results in an increase of the vertical motion of the lifting point for $T_p = 7s$. It can be said that the barges are more influenced by longer period waves but the relation between the wave length, barge width and barge distance is more visible for shorter waves.

When looking at the connection forces it can be seen that the forces are in the order of $1000t$. This amount of force can very well be designed for as it is below the value of $6000t$. The connection forces tend to increase when the length of the barges increases. An increase of the width on the other hand results in a decrease of the connection forces.

Some unexpected findings are visible when looked at the motions for the uncoupled barges. In Figure 5.9 it can be seen that there is no sign of any shielding effect. The motions are even bigger for the vessel shielded by the incoming waves. These effects origin from the inclusion of the external lid, as discussed in section 4.4. Experimental results could disclose if this is also the case in reality.

It is clear that an increase in barge dimensions results in improved hydrodynamical behaviour. For a JONSWAP spectrum with $T_p = 9s$ no clear relation between wave length, barge width and barge distance is visible. Only for an increased distance the motions become a little larger for a wave direction of 90° . For $T_p = 7s$ this relation is more present, although the motions are way less than for $T_p = 9s$.

To improve the dynamical behaviour, the dimensions will be increased to the maximum values in the presented range of dimensions. It is still of interest if the relation between barge gap and barge width has an effect on the response. Therefore the calculation run for the second stage will be performed for a configuration with the following dimensions:

- **Length** = $275m$
- **Draught** = $25m$
- **Width** = $40, 45, 50, 55, 60, 65, 70m$
- **Distance** = $25, 30, 35, 40, 45, 50, 55, 60, 65, 70m$

This time all possible combinations of parameters will be used to calculate the motions to assess the influence of the gap/width relation. In the next section the results of the second stage calculation are discussed.

5.6. SECOND STAGE PARAMETRIC STUDY: RESULTS

In Figure 5.11 the MPM vertical motion of the lifting point is plotted against the width and the barge distance for different incoming wave directions. It can be seen that the trend found in the previous results continues: increased dimensions result in decreased motions. It can be stated that no extraordinary motions are present due to certain relations between the width and the distance. The peak values found previously for certain widths are not longer visible. Still, the influence of a changed distance manifests itself clearly in the graphs. An increased distance results in declined motions. Only for head waves this is not the case.

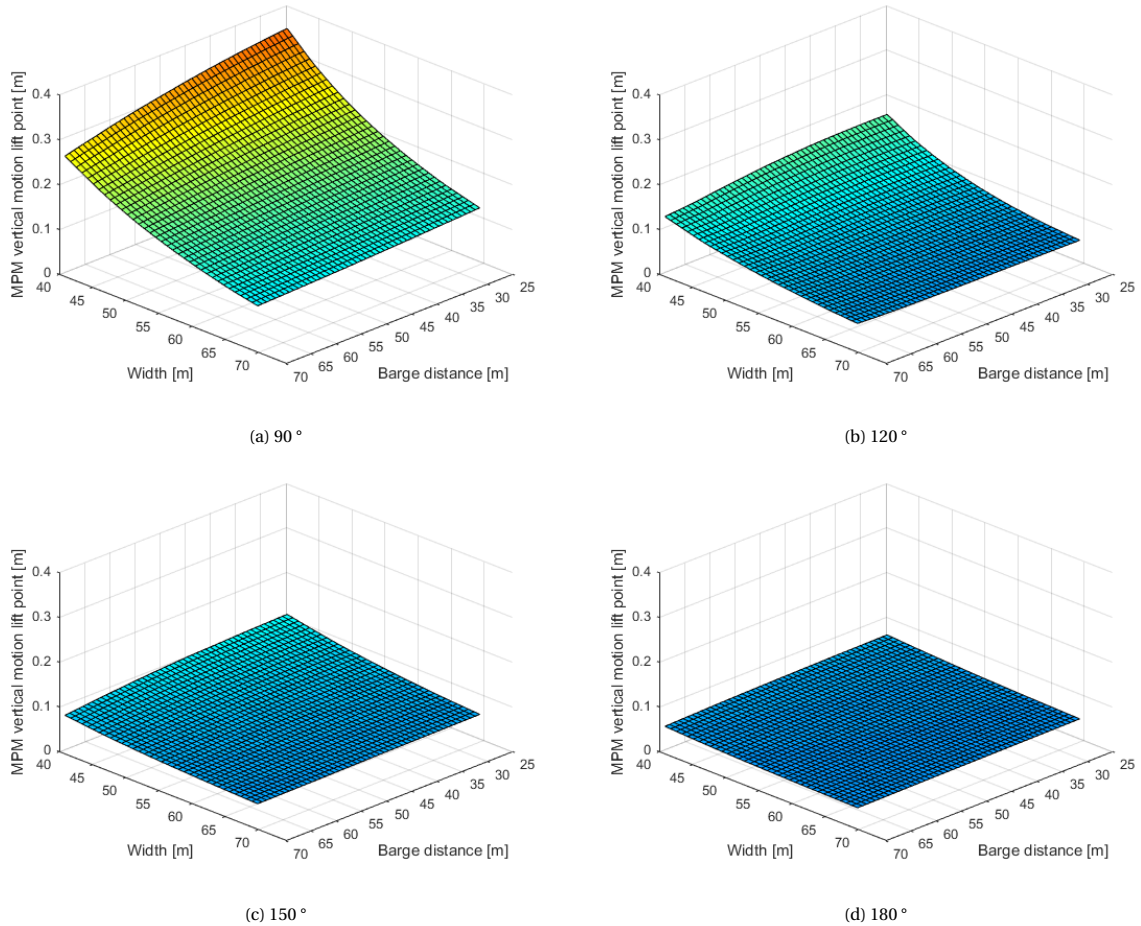


Figure 5.11: MPM vertical motion lift point as function of barge width and barge distance for different incoming wave angles and $T_p = 9s$.

Figure 5.12 shows the most probable maximum relative pitch for incoming waves of 120° and 150°. Similarly to what is observed in Figure 5.7 the relative pitch is larger for incoming waves of 120°. What also stands out is that the increase of distance does not seem to have influence on the relative pitch, while Figure 5.7 does show a slight decrease of relative pitch with increased distance. The figures for 90° and 180° are not included because the relative pitch is equal to zero for those incoming wave angles.

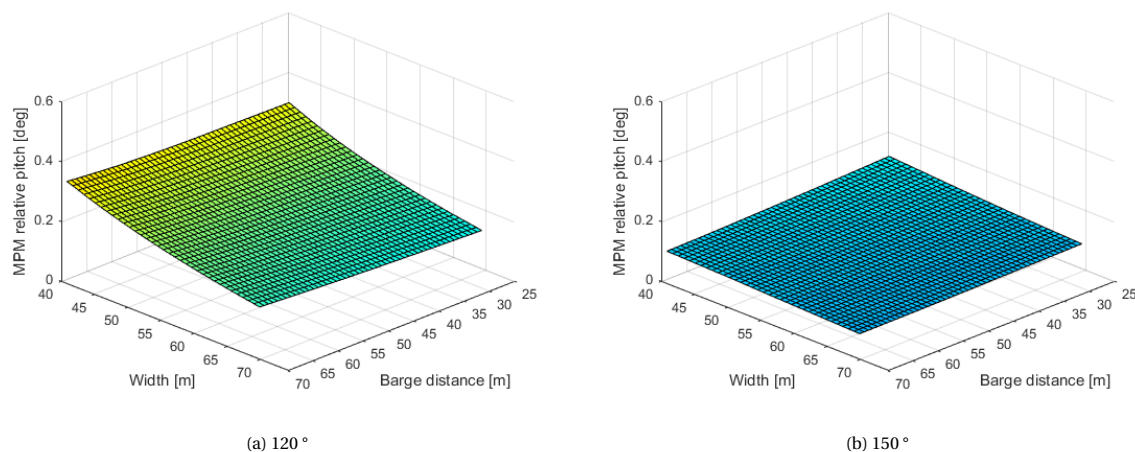


Figure 5.12: MPM relative pitch as function of barge width and barge distance for different incoming wave angles and $T_p = 9s$.

5.6.1. SECOND STAGE PARAMETRIC STUDY: DISCUSSION

The purpose of the second stage calculation was to determine whether extraordinary motions are present due to certain relations between the width and the distance between the barges. Although this relation was evidently influencing the motions in the first stage calculations, it does not have significant impact on the motions in the second stage calculation.

For the final barge design the dimensions will be increased to the maximum value in the range of parameters. Additionally the distance between the barges will be fixed at $50m$ in the following calculations.

5.7. CHAPTER REVIEW

In this chapter the wave input is defined, using a metocean data report for the Brent Delta location in the northern North Sea. The data is used to define a JONSWAP wave spectrum. The wave spectrum is translated into a motion spectrum using the RAOs. The first stage of the parametric study is performed, examining the influence of the changing dimensions on the vessels' motions. Increasing the dimensions overall results in a better hydrodynamic performance. The ratio between the width of the barges and the gap does have influence on the motions. In the second stage of the parametric study the length and draught of the barges is increased to $275m$ and $25m$ respectively. The motions are calculated for each possible combination of the barge width and gap size. The results show now extraordinary motions for certain width to gap ratios. To calculate the limiting sea states and workability the following barge configuration will be used:

- **Length** = $275m$
- **Draught** = $25m$
- **Width** = $70m$
- **Distance** = $50m$



22
M
B
4

21
M
B
4

20
M
B
4

19
M
B
4

18
M
B
4

17
M
B
4

16
M
B
4

15
M
B
4

14
M
B
4

13
M
B
4

12
M
B
4

S I X

L I M I T S

In this chapter a probability study is performed on the exceedence of the critical limits. Probability distributions are made of the impact velocity, the relative pitch and the connection beam force. For different incoming wave directions the limiting parameters are obtained. Finally the operating envelope is determined.

6 | Limiting sea state

6.1. PROBABILITY DENSITY FUNCTIONS

A considerably big amount of data is available on wind and wave conditions at different locations in the sea world wide. Still, the amount of data is not sufficient to test offshore activities on feasibility and safety with complete certainty. To take into account this risk, the environmental conditions are usually modelled with the use of a stochastic model [27]. In these models a probability density function (PDF) of a certain process is determined using the provided data. The water surface elevation is in this way modelled as a Gaussian- or normal distribution [21, ch.5, p.33] :

$$f(x, \sigma) = \frac{1}{\sigma\sqrt{2\pi}} \exp\left(\frac{-x^2}{\sigma^2}\right) \tag{6.1}$$

By assuming that the wave elevation is Gaussian distributed, the amplitude distribution can be derived to be a Rayleigh distribution, given by Equation 6.2 [21, ch.5, p.34]:

$$f(x, \sigma) = \frac{x}{\sigma^2} \exp\left(\frac{-x^2}{2\sigma^2}\right) \tag{6.2}$$

where σ represents the mode of the distribution.

Because the motions are linearly correlated with the wave amplitudes, it is expected that in a linear model the distribution of the motions is also Rayleigh distributed. This relation does however not always hold. The impact velocity of a load lifted by a crane vessel during an offshore lifting operation for instance, does not follow a Rayleigh distribution but is better represented by a Weibull distribution [7]. The latter is given by Equation 6.3:

$$f(x, k, \lambda) = \frac{k}{\lambda} \left(\frac{x}{\lambda}\right)^{k-1} \exp\left(-\left(\frac{x}{\lambda}\right)^k\right) \tag{6.3}$$

where k and λ represent the shape and the scale factor respectively. Note that the Weibull distribution becomes a Rayleigh distribution for $k = 2$ and $\lambda = \sigma\sqrt{2}$. Figure 6.1 shows different Rayleigh and Weibull distributions for different function parameters.

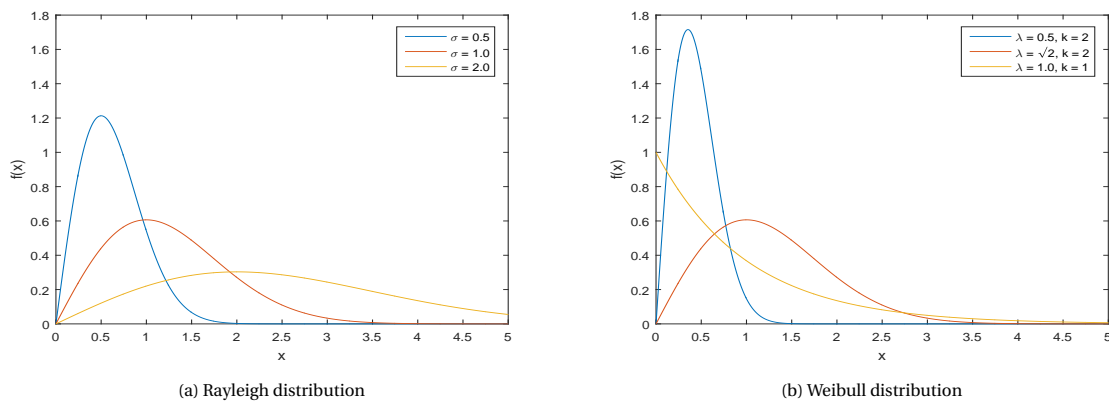


Figure 6.1: Rayleigh and Weibull probability density functions for different function parameters. The Weibull distribution becomes a Rayleigh distribution for $k = 2$ and $\lambda = \sigma\sqrt{2}$ and reduces to an exponential distribution for $k = 1$

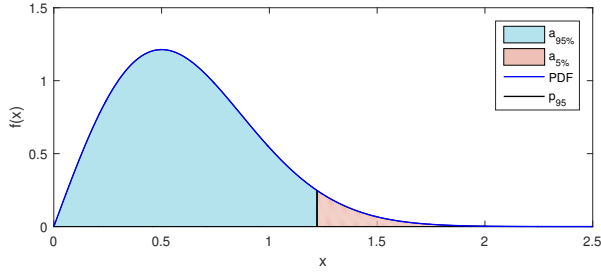


Figure 6.2: Rayleigh PDF showing the 5% and 95% probability interval

Figure 6.2 shows a Rayleigh PDF with $\sigma = 0.5$. The probability of exceedance is calculated by taking the integral from the value to be exceeded to infinity. In that way the p_{95} value represents the value of x for which there is a five percent chance that the value is exceeded, noted in the graph by the pink area.

To say something about the maximum expected limits and the corresponding sea states, a distribution will be made of the impact velocity, relative pitch and connection beam force. Using linear regression both a Rayleigh and a Weibull distribution will be fitted over the data. The goodness of fit will be determined by the use of an quantile-quantile plot (QQ plot). To obtain the PDFs of the limiting parameters two different models are used; the linear Matlab model that is discussed throughout this thesis, and the nonlinear Orcaflex model, used to compare and validate the results of the Matlab model.

6.2. MATLAB: THE FREQUENCY DOMAIN PLUS METHOD

To find the distribution of limiting responses, the frequency domain model has to be translated to time domain. As explained in Chapter 3 this can be done using the superposition principle. The sea state will be simulated by linearly combining a number of different harmonic waves. The sum of all harmonics will represent the sea state in time domain.

$$\zeta(t) = \sum_{n=1}^N \zeta_{a_n} \cos(k_n x - \omega_n t + \epsilon_n) \quad (6.4)$$

where ζ_{a_n} , k_n , ω_n and ϵ_n are the wave amplitude, wave number, frequency and phase for each wave component respectively. The wave amplitude depends on the wave spectrum $S_\zeta(\omega)$ and is given by:

$$\zeta_{a_n} = \sqrt{2 \cdot S_\zeta(\omega) \cdot \Delta\omega} \quad (6.5)$$

where $\Delta\omega$ represents the frequency interval. The phases are randomly generated in the range of $0 < \epsilon_n < 2\pi$. Finally, to obtain the motions, each of the harmonic wave components has to be multiplied by the RAO at the frequency of the harmonic. Orcaflex has the option to discretize the wave spectrum by means of equal energy (Figure 6.3). This means that each harmonic wave component represents an equal amount of energy of the total wave energy spectrum. This discretisation is implemented in the Matlab model by linearly interpolating the RAOs to the discretised values. The combined harmonics result in a time domain simulation of the vessels' motions. This method is also known as the frequency domain plus method.

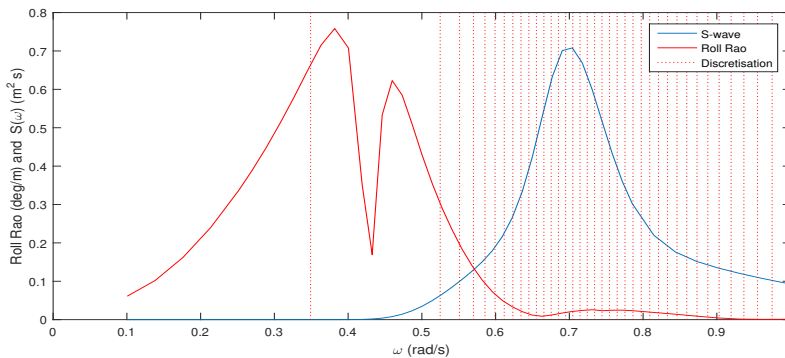


Figure 6.3: Equal energy discretisation of the RAOs and the wave energy. The figure shows the roll RAO for beam waves together with the energy distribution of a JONSWAP spectrum with $T_p=9s$ and $H_s=2m$.

6.3. ORCAFLEX

Additionally a time series will be produced using Orcaflex to compare the Matlab model with a software package that is considered as a standard throughout the maritime industry. Inside the Orcaflex environment, vessels can be added to a certain domain. The hydrodynamical parameters of these vessels can be imported from ANSYS Aqwa. Within Orcaflex certain additional attributes, such as mooring lines, buoys and springs, can be added to the domain. This makes it possible to model the coupled barges system within Orcaflex (Figure 6.4). One effect of the time domain simulation is that the motions are not completely harmonic; the vessels can also drift or rotate. To mitigate these effects mooring lines are included in the model. The stiffness of the mooring lines is chosen to be very low in order to have minimal influence on the primary motions.

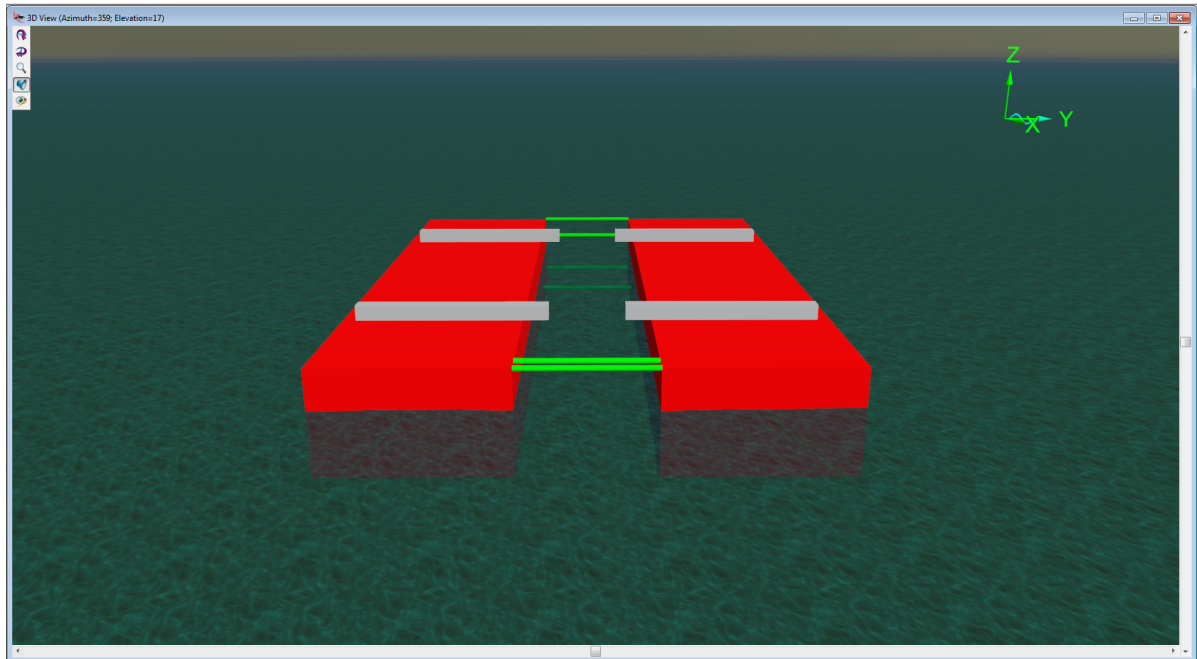


Figure 6.4: Coupled barges modelled within the environment of Orcaflex

Orcaflex has the option to calculate the superimposed motions in time domain with the use of RAOs or using convolution. The latter method calculates the motions each time step, which makes it possible to include the influence of the connection forces on the motions of the vessels. This does come at the cost of being very expensive in calculation time. Still, the convolution method will be used to compare and validate the Matlab model results in the following sections.

6.4. IMPACT VELOCITIES

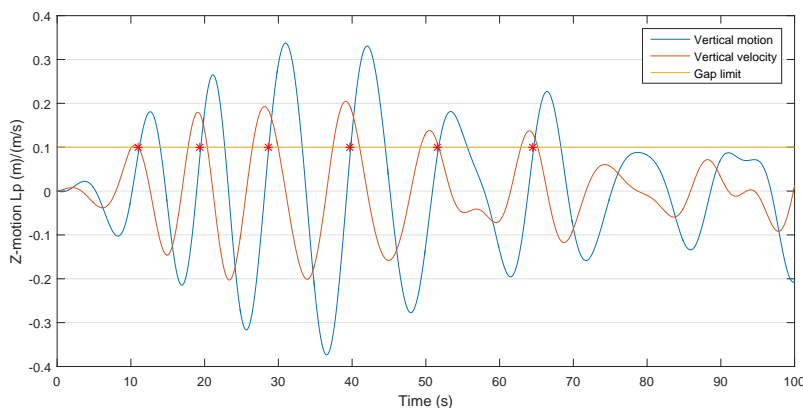


Figure 6.5: An example of a 100s time simulation of the vertical motion of the lifting point for beam waves with $H_s=5m$ and $T_p=9s$. The red dots indicate the moments that impact takes place. Gap size is taken as $0.1m$.

A distribution of the velocities at the moment of impact is made to say something about the probability of exceeding a certain impact velocity (Figure 6.5). The influence of the impact on the motions depends on the details of the lifting system and is different for each topsides. Because the mass of the vessels is much larger than the mass of the topsides, it is expected that the topsides does not influence the motions of the vessels significantly. Still, it can be imagined that the second and third impact velocities might in reality be smaller due to the influence of the *first* impact. During these impacts energy is dissipated which dampens out the motions of the vessels [10, p.137]. Therefore in section 6.4.3 also the velocities of these first impacts will be compared to the previously discussed impact velocities.

6.4.1. NUMBER OF IMPACTS

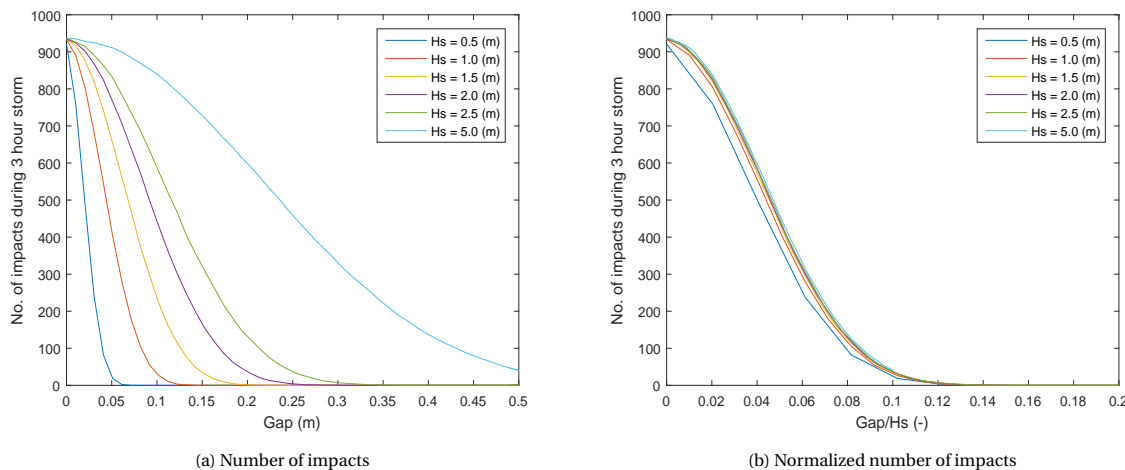


Figure 6.6: Number of impacts during a three hour beam wave sea state as function of gap size and significant wave height. The number of impacts converges to 900 when the gap size becomes zero. This is a measure for the zero crossing period of the motion.

Figure 6.6 shows the number of impacts as function of the gap between the topsides and the lifting point. The right graph also shows the number of impacts but now as function of the gap divided by the significant wave height. It becomes elegantly visible that there is linearity involved. Increasing the gap size and the significant wave height by the same factor does not result in a different number of impacts. Additionally it can be seen that for each significant wave height no impacts are observed from a factor $gap/H_s = 0.16$. When the gap size is bigger than this value no impacts are expected.

6.4.2. IMPACT VELOCITY PROBABILITY DISTRIBUTION

To find the distribution of the impact velocity a histogram is made of the acquired impact velocities at a gap size of $0.05 \cdot H_s$. As example Figure 6.7 shows the impact velocity distribution for beam waves with a significant wave height of 1 m. The height of the bars represents the number of impacts within the edges of the bar during a 24-hour sea state. The graph is normalized to make sure that the area of the graph, or the total probability, equals one. Additionally both a Rayleigh and a Weibull distribution are fitted over the histogram. The quantiles are defined as the values that divide the data in intervals containing an equal fraction of the sample probability. QQ-plots for both distributions are shown for the Rayleigh (left) and Weibull (right) distributions. The QQ-plot shows the quantiles of the sampled data plotted against the quantiles of the theoretical distribution. If both quantiles follow the same linear trend, the sample data coincides with the theoretical distribution. It can be seen that for this significant wave height and incoming wave angle α the Rayleigh distribution, fits the impact velocity distribution well. The k -value of the Weibull fit is close to 2 and the λ -value is close $\lambda = \sigma\sqrt{2}$, indicating that the impact velocity distribution is closely resembled by a Rayleigh distribution. Both QQ-plots do show a light tail on the right side of the plot where the quantiles of the sample data deviate below the theoretical data. This means that the extreme values of the impact velocity are slightly overestimated by the theoretical distributions.

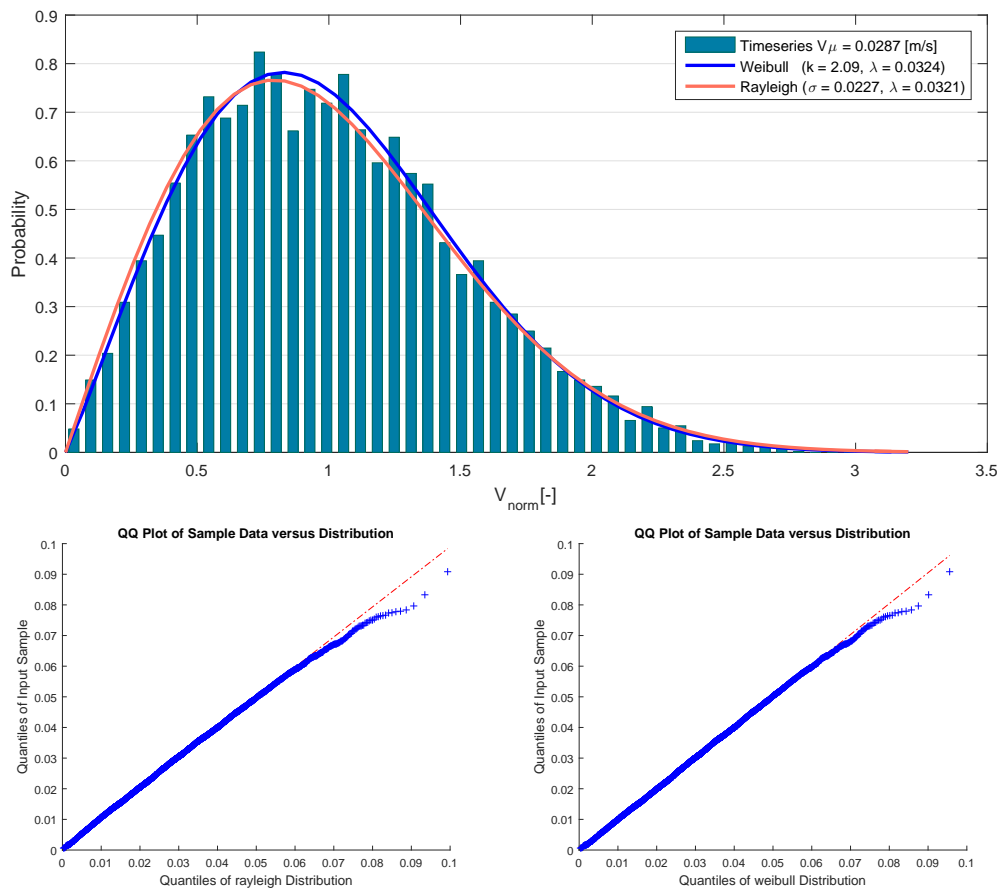


Figure 6.7: Impact velocity distribution for $H_s = 1$ (m) and $\alpha = 90^\circ$. Below the QQ-plots are shown for the Rayleigh (left) and Weibull (right) distributions

The impact velocity distributions of both the linear Matlab model and the nonlinear Orcaflex model are compared in Table 6.1. The value of μ equals the mean impact velocity, sd equals the standard deviation of the data set and p_{95} represents the value for which there is a 95% chance that the impact velocity lies below this value.

Table 6.1: Impact velocity distribution parameters as function of significant wave height for beam waves with $T_p = 9$ s

Hs (m)	Orcaflex			Matlab		
	Distribution parameters					
	μ	sd	p_{95}	μ	sd	p_{95}
1.0	0.029	0.015	0.054	0.028	0.015	0.054
2.5	0.072	0.038	0.139	0.071	0.037	0.137
5.0	0.145	0.076	0.280	0.142	0.073	0.274

It can be seen that the μ , sd and p_{95} parameters increase almost linearly with the increase of the significant wave height. This is the case for both the Matlab model as for the nonlinear Orcaflex model. The Matlab model and Orcaflex model give similar results. The same distribution parameters are compared for oblique incoming waves (Table 6.2). Also here the results are in close agreement. The wave angle of 120° is the most critical wave angle for the impact velocity.

Table 6.2: Impact velocity distribution parameters as function of the incoming wave angle for $H_s = 1$ m and $T_p = 9$ s

α ($^\circ$)	Orcaflex			Matlab		
	Distribution parameters					
	μ	sd	p_{95}	μ	sd	p_{95}
90	0.029	0.015	0.054	0.028	0.015	0.054
120	0.030	0.014	0.055	0.029	0.013	0.050
135	0.022	0.010	0.040	0.021	0.010	0.039
150	0.013	0.006	0.024	0.014	0.007	0.027
180	0.010	0.005	0.019	0.010	0.005	0.019

For quartering waves the Weibull distribution represents the impact velocity much better (Figure 6.8). Additionally the QQ-plot of the Rayleigh distribution does not fit the linear line as good as the Weibull distribution does. Both distributions are lightly tailed, indicating a slight overestimation of the extreme values. The results coincide with a previous study on the impact velocity distribution [7].

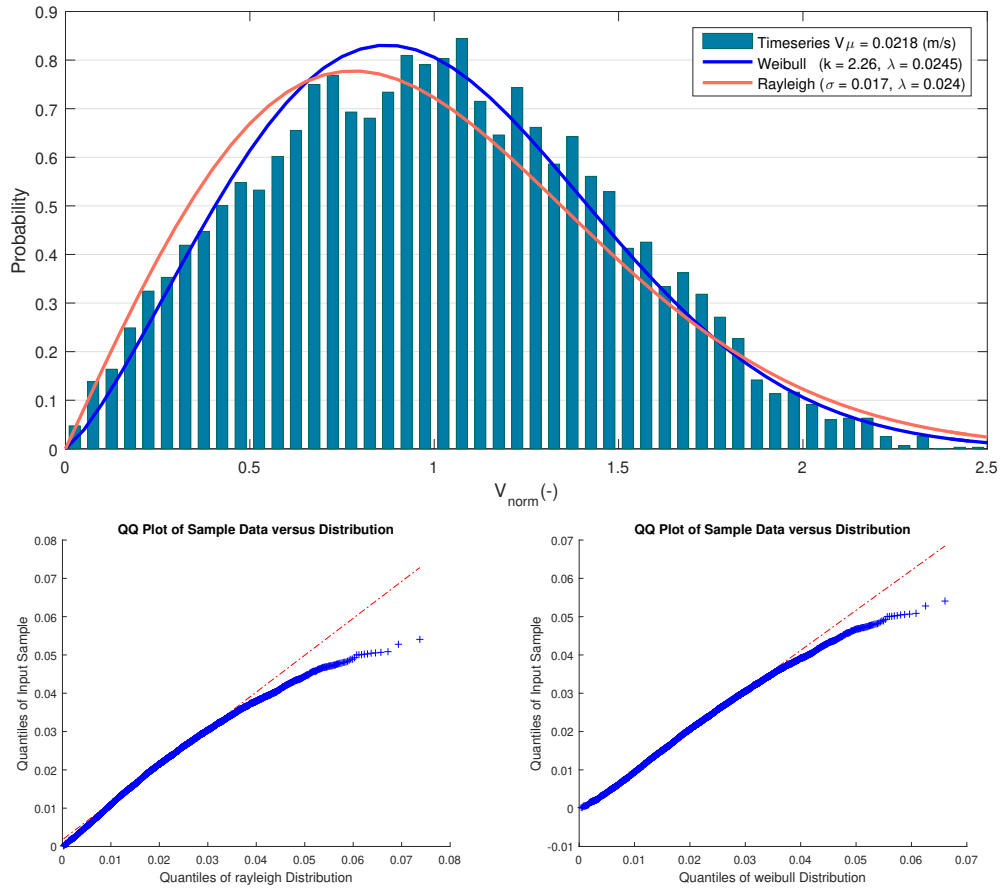


Figure 6.8: Impact velocity distribution for $H_s = 1$ (m) and $\alpha = 135^\circ$. Below the QQ-plots are given for the Rayleigh (left) and Weibull (right) distributions

6.4.3. FIRST IMPACT VELOCITY PROBABILITY DISTRIBUTION

As explained in section 6.4, the impact velocity distribution of the *first* impact is discussed here. To simulate the first impact, the initial gap size will be taken as $0.2H_s$. In this way no impact will take place during this initial phase. After this the gap size will be decreased until the lifting point hits the platform. Figure 6.9 shows the time series of the first impact.

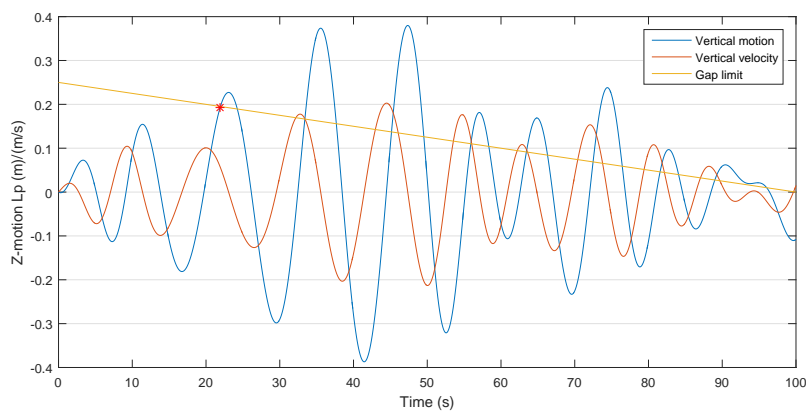


Figure 6.9: First impact time series for $H_s = 5$ m and beam waves with $T_p = 9$ s. The gap limit is decreased to represent the de-ballasting of the vessels

The setdown speed depends on the ballast capacity of the vessel. It is known that a similar vessel such as the *BOKA Vanguard* has a ballast capacity of over $22.500 \text{ m}^3/\text{hr}$ [4]. Similarly the *Pioneering Spirit* has a main ballast capacity of $19.000 \text{ m}^3/\text{hr}$. The *BOKA Vanguard* has similar dimensions and therefore this ballast capacity will be assumed to calculate the set down speed.

$$V_{setdown} = \frac{22.500}{L \cdot B \cdot 3600} = 0.00032 \quad (\text{m/s}) \quad (6.6)$$

Tables 6.3 and 6.4 compare the Weibull distribution parameters of the first impact velocity with those of the impact velocity previously discussed and displayed in Tables 6.1 and 6.2. It can be seen that the mean first impact velocity is almost half of the mean overall impact velocity for beam waves. For oblique incoming waves only a slight decrease of the impact velocity is visible when looked at the first impact.

Table 6.3: Impact velocity distribution parameters as function of significant wave height for beam waves and $T_p = 9\text{s}$

Hs (m)	Matlab timeseries			Matlab first impact		
	Distribution parameters					
	μ	sd	p_{95}	μ	sd	p_{95}
1.0	0.028	0.015	0.054	0.012	0.006	0.024
2.5	0.071	0.037	0.137	0.032	0.017	0.061
5.0	0.142	0.073	0.274	0.066	0.034	0.125

Table 6.4: Impact velocity distribution parameters as function of the incoming wave angle for $H_s = 1\text{m}$ and $T_p = 9\text{s}$

α (°)	Matlab timeseries			Matlab first impact		
	Distribution parameters					
	μ	sd	p_{95}	μ	sd	p_{95}
90	0.028	0.015	0.054	0.012	0.006	0.024
120	0.029	0.013	0.050	0.010	0.005	0.019
135	0.021	0.010	0.039	0.009	0.005	0.019
150	0.014	0.007	0.027	0.009	0.004	0.017
180	0.010	0.005	0.019	0.009	0.004	0.017

6.4.4. IMPACT VELOCITY SECTION REVIEW

The results show that both the impact velocity and the first impact velocity seem to be linearly correlated with the significant wave height. The impact velocity is best resembled by a Weibull distribution. Both the Matlab and Orcaflex model give agreeing results.

When comparing the impact velocity distribution to the *first* impact velocity distribution it can be seen that the first impact velocity is almost half of the regular impact velocity. It would therefore be very interesting to know what the influence of the impact is on the motions of the vessel. The investigation of this lies outside the scope of the thesis. Therefore the most conservative values of the impact velocity will be used to define the limiting sea state being the results of the Orcaflex time domain simulation.

6.5. TOPSIDES LOADS

To assess the loads in the topsides the Brent Alpha topsides will be subjected to prescribed motions and accelerations. Because the mass of the topsides is small in comparison to the mass of the vessels, the influence of the topsides on the motions is not taken into account. The main contributor to the topsides loads is the relative pitch. The accelerations only play a small role and are therefore not taken into account. An assessment on this topic can be found in Appendix E.

6.5.1. RELATIVE PITCH PROBABILITY DISTRIBUTION

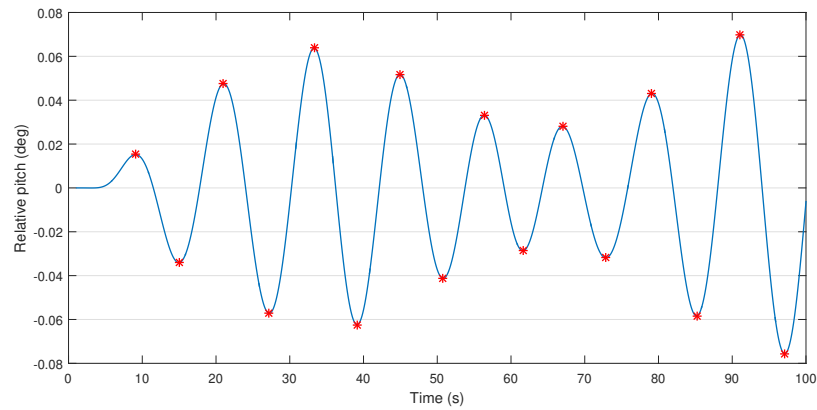


Figure 6.10: Relative pitch time series, $H_s = 1\text{ m}$, $\alpha = 120^\circ$

Figure 6.10 shows a time series of the relative pitch for a sea state with a significant wave height of 1 m and an incoming wave angle of $\alpha = 120^\circ$. To say something about the maximum relative pitch angle during a certain period, a distribution will be made of the maximum relative pitch values. These values are highlighted with the red dots. Because the direction of the relative pitch is of no importance, a distribution is made of the absolute values. Again QQ-plots are made for both the Weibull and Rayleigh distribution (Figure 6.11). Both distributions are lightly tailed, thus the theoretical distributions overestimates the extreme values slightly.

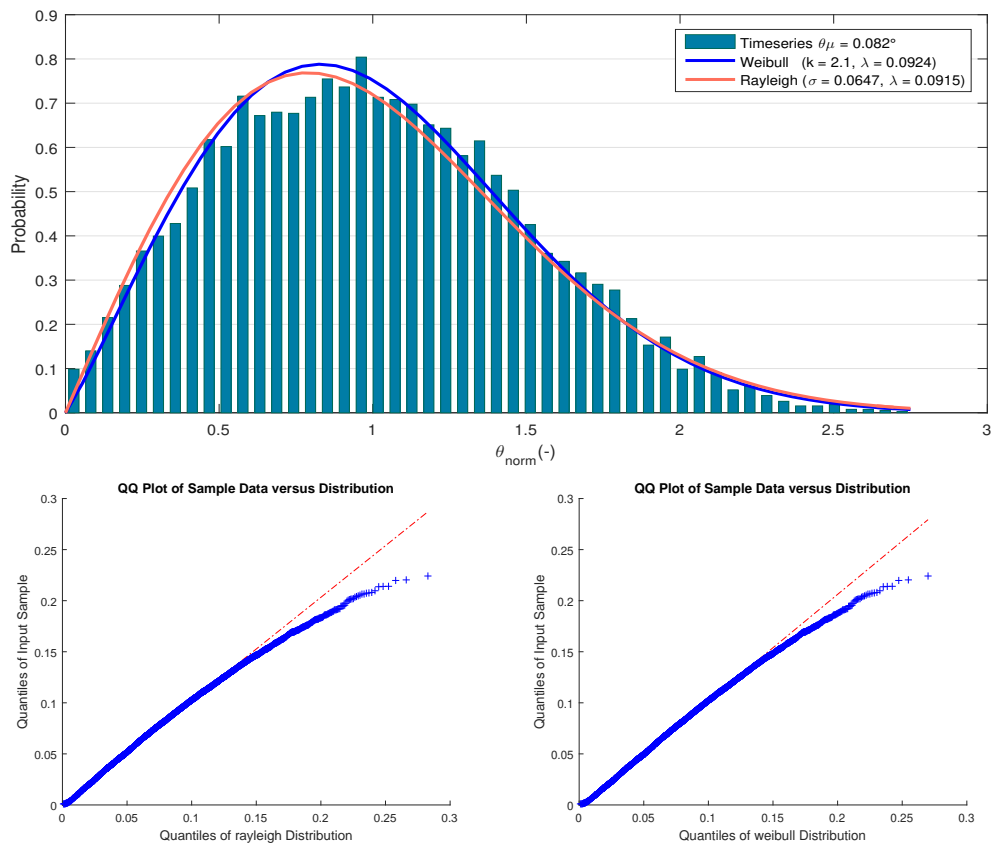


Figure 6.11: Relative pitch distribution and QQ-plots for waves with $H_s = 1\text{ m}$, $T_p = 9\text{ s}$ and an incoming wave angle of $\alpha = 120^\circ$

Table 6.5 compares the distribution parameters of the relative pitch distribution only for incoming wave angles of 120° , 135° and 150° . The relative pitch for beam and head waves is very small and those wave angles are therefore not taken into account. The parameters are obtained using both the Matlab and Orcaflex model time series. It can be seen that the Matlab model slightly underestimates the relative pitch in comparison with Orcaflex. Both models show that the relative pitch stays well below the 0.38° for a significant wave height of 1 m .

Table 6.5: Relative pitch distribution parameters as function of incoming wave angle for $H_s = 1\text{ m}$ and $T_p = 9\text{ s}$

α ($^\circ$)	Orcaflex			Matlab		
	Distribution parameters					
	μ ($^\circ$)	sd ($^\circ$)	p_{95} ($^\circ$)	μ ($^\circ$)	sd ($^\circ$)	p_{95} ($^\circ$)
120	0.082	0.043	0.155	0.076	0.038	0.144
135	0.074	0.039	0.140	0.067	0.033	0.126
150	0.048	0.025	0.089	0.042	0.021	0.079

6.5.2. TOPSIDES LOADS SECTION REVIEW

Oblique incoming waves result in relative pitch. For 120° incoming waves with a significant wave height of 1 m , a relative pitch angle of 0.155° is calculated as the p_{95} value, which is already close to the limiting value of 0.38° . The forces in the legs due to the accelerations are dwarfed by the forces due to this relative pitch. For exact beam and head waves also the relative pitch becomes very small and the accelerations will have more influence. Still, the topsides accelerations have minor influence on the topsides loads and will therefore not be included in the limiting load cases.

6.6. CONNECTION FORCES PROBABILITY DISTRIBUTION

Figure 6.12 shows a time series of the axial forces in the connection beams calculated with Orcaflex. Due to the high stiffness of the connections, the force has some high frequent behaviour. Because of this behaviour making a distribution of the peak values does not represent a distribution of the extreme values. Therefore the peak values will be translated to the extreme values before the distribution is made.

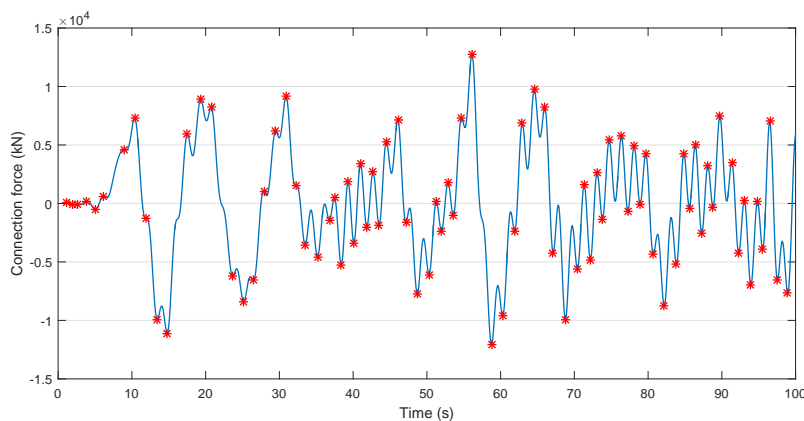


Figure 6.12: Time domain simulation of the axial connection force for $H_s = 1\text{ m}$, $T_p = 9\text{ s}$ and $\alpha = 90^\circ$

To do so the zero crossing period of the motions is calculated. This value is then used to condition the extracted peak values. Within one zero crossing period the maximum peak will be determined. The next maximum value will be determined after another zero crossing period. This way of filtering results in Figure 6.13 where the red dots represent the peaks considered in the distribution.

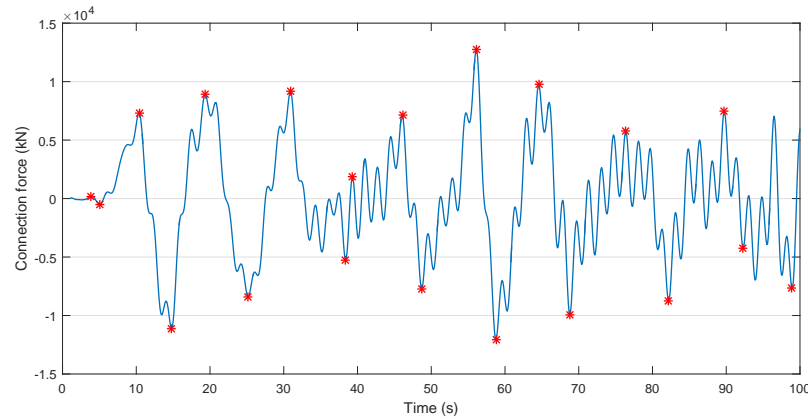


Figure 6.13: Filtered extreme values of the time domain simulation of the axial connection force for $H_s = 1m$, $T_p = 9s$ and $\alpha = 90^\circ$

In this way the high frequent behaviour is filtered out of the extreme value distribution. This results in the distribution of the connection force for 90° seen in Figure 6.14. Both the Weibull and Rayleigh distribution give a corresponding fit for the sample data. At the right tail of the graph the Weibull distribution seems to fit the sampled data a little better. The QQ-plot shows that the quantiles of the sampled data are larger than the quantiles of the Weibull distribution, meaning that the theoretical Weibull distribution underestimates the extreme values slightly.

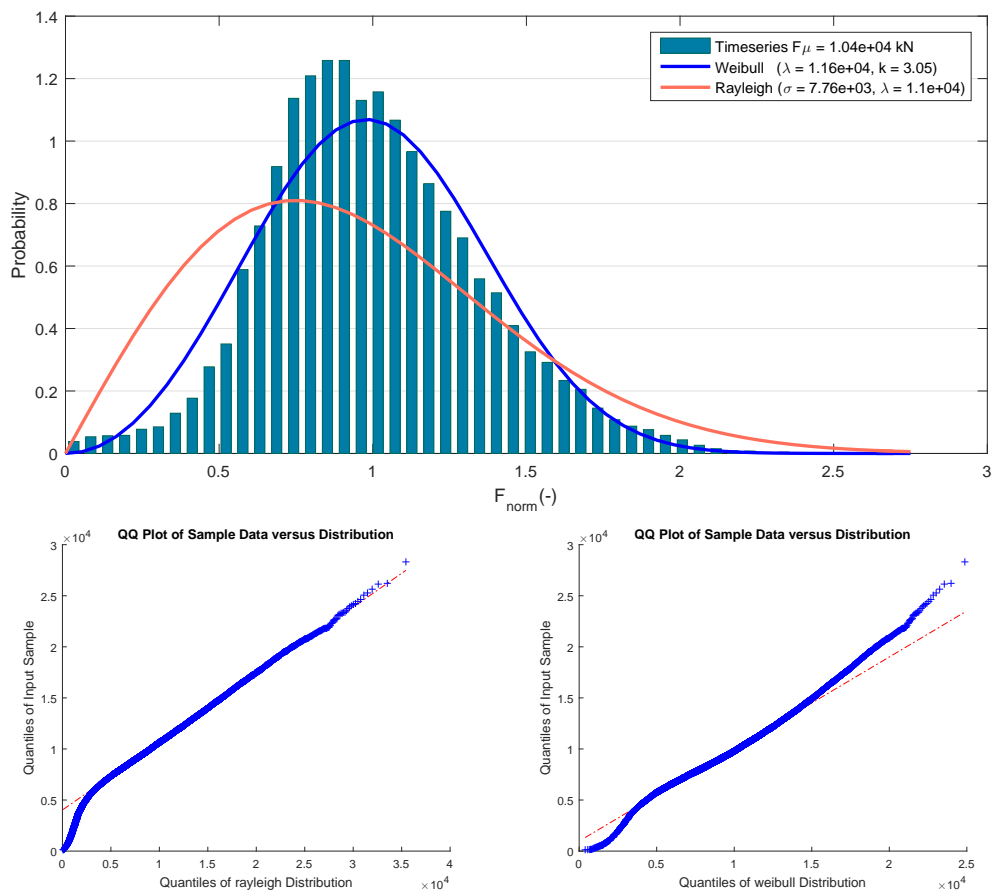


Figure 6.14: Axial connection force distribution and QQ-plots for $H_s = 1 (m)$ and $\alpha = 90^\circ$

Table 6.6 shows the distribution parameters of the connection force as function of the significant wave height for both the Orcaflex and the Matlab time domain simulation. It can be seen that for both models there is an almost linear relation between the wave height and the force. The Matlab model slightly underestimates the forces in comparison with the Orcaflex model.

Table 6.6: Axial connection force distribution parameters as function of significant wave height for beam waves with $T_p = 9$ s

Hs (m)	Orcaflex			Matlab		
	Distribution parameters					
	μ (t)	sd (t)	p_{95} (t)	μ (t)	sd (t)	p_{95} (t)
1.0	1040	537	1700	844	363	1483
2.5	2600	1343	4124	2100	907	3717
5.0	5230	2705	8319	4220	1815	7433

For beam waves the wave force is in the axial direction of the connections. Therefore the high frequent behaviour is more visible than for quartering waves. The fading of this effect is shown in Figure 6.15 where a time series of the connection force is plotted for a wave angle of 120° .

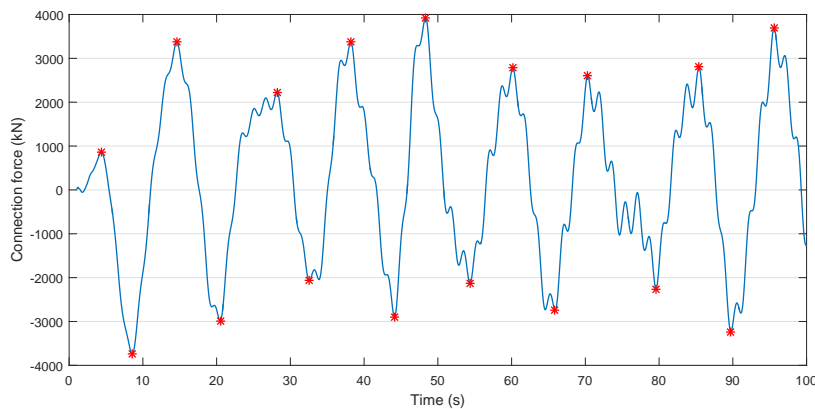


Figure 6.15: Time domain simulation of the axial connection force for $H_s = 1$ m, $T_p = 9$ s and $\alpha = 120^\circ$

The distribution of the connection forces for this wave angle is shown in Figure 6.16. Both the Rayleigh as the Weibull distribution fit the data of the connection force. Both QQ-plots show that the quantiles of the data are larger than the theoretical distributions at the right tail. This indicates that the Rayleigh and Weibull distributions both underestimate the extreme values of the force in the connection beams.

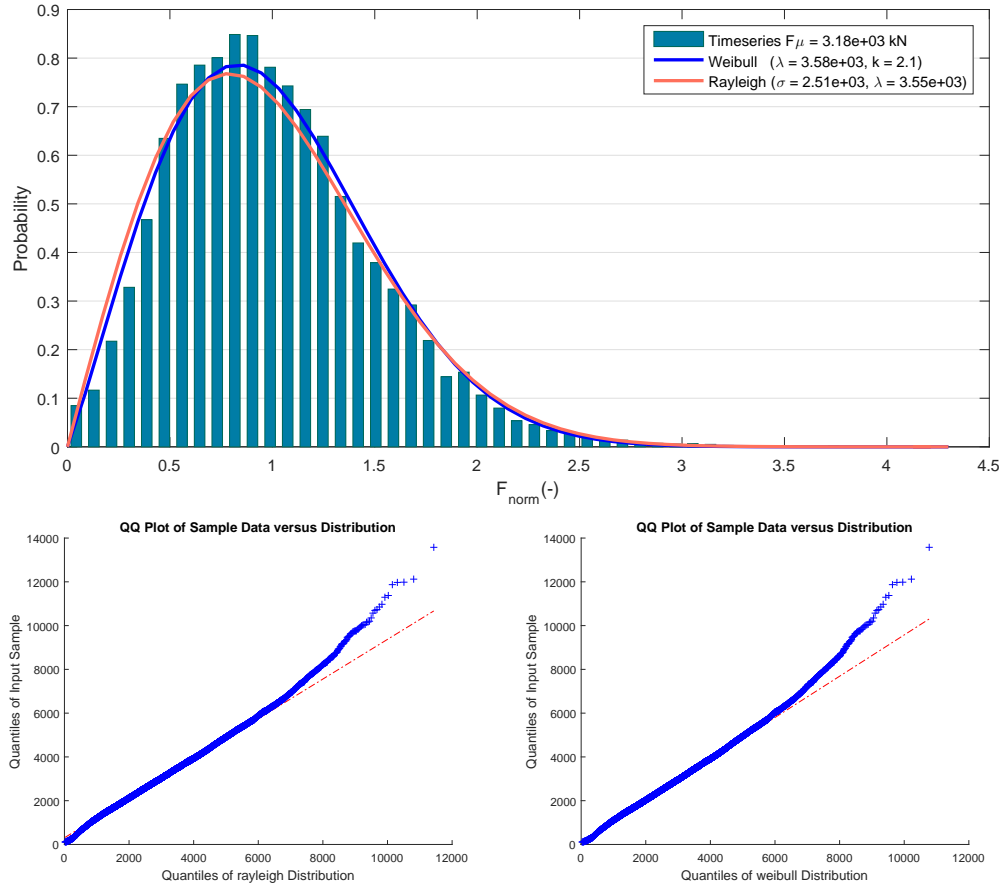


Figure 6.16: Axial connection force distribution and QQ-plots for $H_s = 1\text{ m}$, $T_p = 9\text{ s}$ and $\alpha = 120^\circ$

Table 6.7 shows the Weibull distribution parameters of the connection force for different incoming wave angles. Also here the mean value of the 24-hour simulation and the 95% force value are shown for both the Orcaflex and Matlab simulation. It can be seen that the force in the connection beams is the largest for beam waves. The force gradually decreases for bigger incoming wave angles. The Orcaflex model gives slightly lower values in comparison with the Matlab model for oblique or head waves. For beam waves the Matlab model calculates a lower value for the connection force. For a significant wave height of 1 m , the connection force stays well below the limit of 6000 t for all incoming wave angles.

Table 6.7: Connection force distribution parameters as function of incoming wave angle for $H_s = 1\text{ m}$ and $T_p = 9\text{ s}$

α ($^\circ$)	Orcaflex			Matlab		
	Distribution parameters					
	μ (t)	sd (t)	p_{95} (t)	μ (t)	sd (t)	p_{95} (t)
90	1040	537	1700	844	363	1483
120	318	167	600	375	187	714
135	193	101	406	225	117	429
150	135	70	250	152	79	283
180	45	24	80	51	26	91

6.6.1. CONNECTION FORCES SECTION REVIEW

The highest connection forces are found when the vessel is subjected to beam waves. For this wave direction the connection force seems to increase linearly with the wave height. For a significant wave height of $1m$ the forces remain well below the $6000t$. The QQ-plots show that both the Rayleigh and Weibull distribution give a good fit but slightly underestimate the extreme values of the connection force.

6.7. DAMPING LID SENSITIVITY

In Chapter 4 the influence of the damping lid on the RAOs is discussed. The damping value $\epsilon = 0.05$ was adopted for the calculations of the parametric study. This section discusses again the influence of the damping factor but now on the results of a 24-hour time domain simulation performed with Orcaflex. It is clear that the damping lid has only very minor influence on the vessels motions (Table 6.8). A explanation for this can be that the damping lid influences the RAOs mostly for the lower frequencies, and not for the higher frequencies where most of the wave energy is applied.

Table 6.8: Values for the impact velocity, the relative pitch and the connection force for different values of ϵ . The values are obtained from a 24-hour simulation with a significant wave height of $H_s = 1m$ and for quartering seas, $\alpha = 135^\circ$

	Impact velocity		Relative pitch		Connection force	
	Orcaflex simulation values					
	μ	p_{95}	μ	p_{95}	μ	p_{95}
$\epsilon(-)$	(m/s)	(m/s)	($^\circ$)	($^\circ$)	(t)	(t)
0.00	0.023	0.044	0.077	0.146	193	392
0.01	0.024	0.043	0.075	0.143	217	425
0.05	0.022	0.040	0.074	0.140	193	406
0.10	0.023	0.043	0.075	0.141	191	403

It can be seen that the outcome for different damping values is in the same order of magnitude. The damping value of 0.01 results in the largest motions. This coincides with the RAOs found in section 4.4. For the impact velocity this means that the outcome can deviate with 4% depending on choosing a damping lid value of $\epsilon = 0.01$ or $\epsilon = 0.05$. For the connection force this outcome can differ up to 22% for a damping lid value of $\epsilon = 0.10$ or $\epsilon = 0.01$. Scaled model tests are the best way to provide information on the appropriate damping value.

6.8. LIMITING DESIGN WAVE

To find the limiting significant wave height per wave direction, assuming that the system is linear with the wave height is very convenient. It was already shown that the impact velocity and connection forces for beam waves increase linear with the increase of the wave height. Table 6.9 additionally shows the mean and maximum limit values of a 24-hour time series for quartering seas. The pitch and impact increase almost linearly for a significant wave height between zero and five meters. For the connection force this is not the case. The forces in the connections show a strong nonlinear behaviour. This makes it impossible to predict the limiting significant wave height using the linearity assumption.

Table 6.9: Distribution values of the impact velocity, relative pitch and connection force for quartering seas of $H_s = 1m$ and $H_s = 5m$. The ratio between values is given to give an indication of linearity i.e. if the ratio lies close to five, the limiting parameters are linearly related with the wave height

	Impact velocity		Relative pitch		Connection force	
	Orcaflex simulation values					
	μ	p_{95}	μ	p_{95}	μ	p_{95}
H_s (m)	(m/s)	(m/s)	($^\circ$)	($^\circ$)	(t)	(t)
1	0.022	0.040	0.074	0.140	193	406
5	0.099	0.183	0.378	0.726	1880	5670
Ratio	4.5	4.6	5.1	5.2	9.7	14.0

The linearity assumption is adopted to give an estimation of the wave height for which the critical parameters will be exceeded. This means that the scale factor of the Weibull distribution can be increased linearly with the increase of the wave height. The shape factor remains the same. In this way the probability calculation can be switched around; the significant wave height can be calculated given a chance of failure. This probability of failure is taken as one percent:

$$p_{3hr} > x_{lim} = 1 - p^n = 1\% \quad (6.7)$$

where

$$p = 1 - \exp\left(\frac{-x}{H_s \cdot \lambda}\right)^k \quad (6.8)$$

Additionally n , the number of occurring peak values during a three-hour storm is needed. For the relative pitch n can be calculated by dividing the 10800s by half the zero crossing period of $T_z = 6.17s$. The same holds for the connection force. For the impact velocity it is assumed that in practice there can be thought of the incorporation of a system that connects the lifting point to the topsides at the first impact, mitigating possible rebounds. The value of n in that case will be one. Still, the most conservative impact velocity distribution will be used. Besides, n will be taken as five, to take into account some uncertainty corresponding to the probability that setting up the connection failed the first four times. An overview of the limiting sea states can be found in Table 6.10 using the limiting values of $0.2m/s$, 0.38° and $6000t$ for the impact velocity, relative pitch and connection force respectively.

Table 6.10: Limiting significant wave height regarding the impact velocity and relative pitch per incoming wave angle and $T_p = 9s$ based on the Orcaflex time domain simulations and with a probability of failure of one percent

	Impact velocity				Relative pitch				Connection force			
	Weibull distribution parameters and limiting wave height											
	k	λ_{wbl}	n	H_s	k	λ_{wbl}	n	H_s	k	λ_{wbl}	n	H_s
α (°)	(-)	(-)	(-)	(m)	(-)	(-)	(-)	(m)	(-)	(-)	(-)	(m)
90	2.09	0.032	5	2.6	n.a.	n.a.	n.a.	n.a.	3.06	1160	3500	2.3
120	2.23	0.032	5	2.8	2.10	0.092	3500	1.3	2.13	360	n.a.	n.a.
135	2.24	0.021	5	4.2	2.12	0.084	3500	1.4	1.74	217	n.a.	n.a.
150	2.37	0.015	5	6.2	2.17	0.054	3500	2.3	2.16	152	n.a.	n.a.
180	2.76	0.011	5	9.4	n.a.	n.a.	n.a.	n.a.	2.48	51	n.a.	n.a.

Unfortunately the same approach can not be applied to calculate the wave height for which the maximum connection force is exceeded for oblique incoming waves. For beam waves a limiting significant wave height of $H_s = 2.3m$ can be found for the connection force. For head and oblique incoming waves it is expected that the maximum relative pitch and impact velocity are reached sooner than the maximum connection force. For the impact velocity high design wave heights are calculated as the waves come more from the head direction. It is expected that these wave heights do not give a correct representation of the actual design wave height for this direction. Effects such as wave spreading can have significant influence on the motions, but are not taken into account in these calculations. This for instance means that the relative pitch is non-existent in the model for head waves. In reality the relative pitch motion will be present even for head waves due to wave spreading. The negligence of these effects result in an overestimation of the design wave and workability for head waves.

6.9. WORKABILITY

The workability of the concept will be calculated by the use of the wave scatter diagrams provided by Shell (Appendix C). For each sea state presented in the wave scatter diagram there will be determined whether the decommissioning concept can safely perform the operation. The workability is defined as the percentage of sea states in which the operation can safely be performed. As many sea states have to be evaluated the faster Matlab model is used to calculate the workability (Figure 6.16).

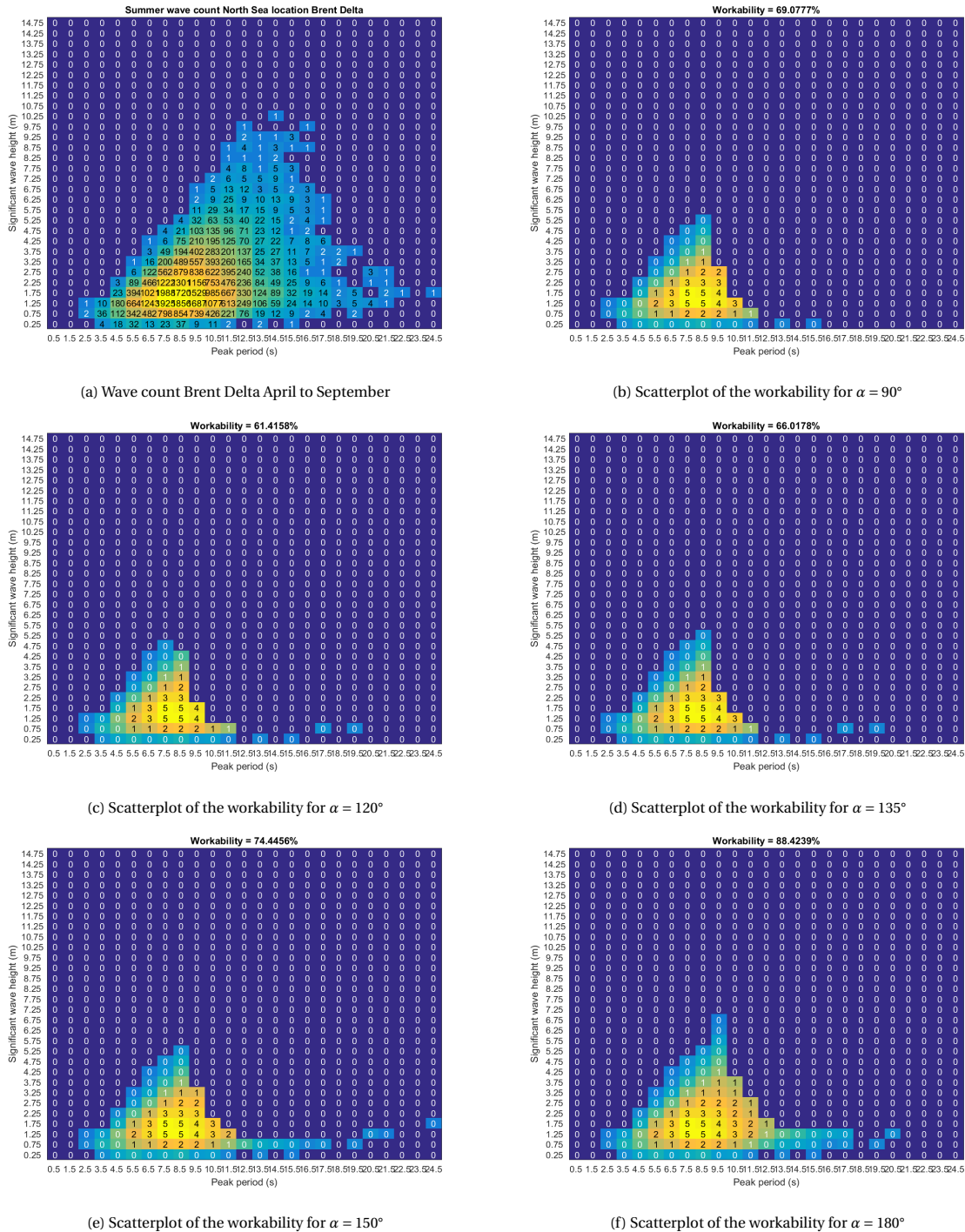


Figure 6.17: Summer wave count for the Brent field location and corresponding workabilities for incoming wave angles of $\alpha = 90^\circ$, $\alpha = 120^\circ$, $\alpha = 135^\circ$, $\alpha = 150^\circ$ and $\alpha = 180^\circ$. The values in the workability scatter diagrams represent the rounded percentage of the total number of waves in the corresponding bin.

Depending on the orientation of the platform and the direction of the waves the operation can be performed for different incoming wave angles. For the most critical incoming wave angle of $\alpha = 120^\circ$ a workability is found of 61%. The most favourable wave direction of $\alpha = 180^\circ$ results in a workability of 88%. It can be seen that the peak period of the wave spectrum has a significant influence on the workability. Beyond a peak period of 9s, only for small significant wave heights a safe operation could be guaranteed.

6.10. CHAPTER REVIEW

The probability distributions of all limiting factors are calculated using Orcaflex and Matlab in combination with the frequency domain plus method. It was found that the impact velocity follows a Weibull distribution. It is of great influence whether a distribution is made of all impacts given a certain gap, or if only the first impact is taken into account.

The forces in the topsides are dominated by the relative pitch. The accelerations in the topsides become more important when the vessel is subjected to beam or head waves. Still to calculate the limiting sea state, the accelerations are neglected. Also the relative pitch seems to follow a Weibull distribution.

The connection forces show some high frequent behaviour. This makes it difficult to fit a distribution to the data. For oblique incoming waves the data seems to follow a Weibull distribution, for beam waves the Weibull fit is not trustworthy. The connection forces only show a linear correlation with the increase of wave height for beam waves.

Differences between motions calculated with the linear Matlab and nonlinear Orcaflex model are only minor. For the calculation of the connection beam force the models start deviating more. It can be said that the linearisation of the connections forces in the Matlab model does not influence the motions but does influence the magnitude of the axial force in the connection beams. Additionally it is found that the damping lid value has very little influence on the calculated motions.

The limiting significant wave heights for a Jonswap spectrum with $T_p = 9s$ are given in Table 2.1 based on the Orcaflex time domain simulations. The critical incoming wave angle is 120° , where a significant wave height of $1.3m$ results in failure due to excessive relative pitch. Also for the other oblique incoming waves the relative pitch is the limiting factor. For beam waves the connection forces and the impact velocity are limiting. Head waves are the preferred wave direction for the lifting of a topsides using two mechanically connected barges.

The workability is calculated for the Brent Delta location in the summer period using the Matlab model. The most favourable wave direction of 180° results in a workability of 88%. For a wave direction of 120° this workability drops to 61%. Depending on the wave direction and the orientation of the platform the workability of the mechanically coupled barges will lie between these two values.



S E V E N

C O N C L U S I O N & R E C O M M E N D A T I O N S

In this chapter the conclusions of the previous chapters are summarized. Recommendations are given to improve the dynamic model in the future. The importance of model tests is highlighted and an advice is given on the topic of future research.

7 | Conclusion and recommendations

7.1. CONCLUSIONS

The two-vessel reverse float-over decommissioning concept may potentially offer a solution to existing challenges concerning the removal of heavy topsides of offshore oil and gas structures. Mechanically coupling of the vessels increases the workability of the concept, making it potentially feasible for the rough conditions of the North Sea. To assess the hydrodynamic behaviour and determine the workability of the concept a dynamical model is made using the potential solver ANSYS Aqwa in combination with Matlab. Small motions may be assumed and the linearisation of the connection forces is substantiated, making a frequency domain approach possible.

Hydrodynamic coupling between the vessels results in standing waves between the barges. The wave elevation is overestimated by the potential solver due to the absence of nonlinear damping within the software. An additional 10% roll damping is added to meet the actual roll damping of the vessels. The standing wave effect still remains. The external lid approach is adopted, adding damping to the wave elevation between the barges. Based on previous experimental studies on side-by-side moored LNG tankers a damping value of $\epsilon = 0.05$ is incorporated. Still some cautiousness is needed towards this approach as it is difficult to find a rational in the value of the damping lid.

A sensitivity study is performed on the dimensions of the vessels and the distance between them. Overall increasing the dimensions results in a decrease of the vessels' motions. For beam waves an increase of the width and draught is the most efficient way of decreasing the motions. For head waves increasing the length is most efficient. For a JONSWAP wave spectrum with $Tp = 7s$ the relation between width and distance is of influence on the motions. Increasing the width does not necessarily mean an improvement of the seakeeping behaviour. For a JONSWAP wave spectrum with $Tp = 9s$ this relation becomes less visible. When increasing the dimensions of the vessels the relation between width and distance loses its influence.

The three main limiting responses of the coupled twin-vessel float-over concept are found to be the impact velocity of the lifting points on the topsides, the axial forces in the connection beams and the relative pitch between both vessels (Table 7.1).

Table 7.1: Limiting parameters and their magnitude

Parameter	Limit	Unit
Impact velocity	0.2	(m/s)
Connection load	6000	(t)
Relative pitch	0.38	(°)

Utilizing the frequency domain plus method with Matlab, the frequency domain model is translated to time domain. Additionally Orcflex is used to calculate the motions in time domain as comparison and validation for the Matlab model. The linear frequency domain approach proves to be a fast and effective alternative for the nonlinear time domain approach in Orcflex. Minor differences between the models are found in the assessment of the axial forces in the connection beams, which are the linearised parts in the Matlab model. For the vessel motions these calculated differences are found to be only very minimal.

Distributions are made of the impact velocity, relative pitch and axial connection beam force. The impact velocity follows a Weibull distribution and increases linearly with the increase of significant wave height. It is of great importance whether the impact velocity is calculated regardless of the influence of the impact on the motions, or only the *first* impact is calculated. For the relative pitch both the Rayleigh as the Weibull distribution give a proper fit. Also here the linear increase with the wave height holds. The axial connection force shows high frequent behaviour for beam waves. For oblique incoming waves this effect decreases. Between

the Rayleigh and Weibull distributions the Weibull gives the best fit. The linear increase with wave height holds for beam waves. For oblique incoming waves the increase becomes nonlinear.

To find the limiting significant wave height the linearity assumption is used. This results in the design waves for a peak period of $Tp = 9s$ given in Table 7.2.

Table 7.2: Limiting significant wave height regarding the impact velocity and relative pitch per incoming wave angle and $Tp = 9s$ based on the Orcaflex time domain simulations and with a probability of failure of one percent

α (°)	Impact velocity				Relative pitch				Connection force			
	Weibull distribution parameters											
	k	λ_{wbl}	n	Hs	k	λ_{wbl}	n	Hs	k	λ_{wbl}	n	Hs
	(-)	(-)	(-)	(m)	(-)	(-)	(-)	(m)	(-)	(-)	(-)	(m)
90	2.09	0.032	5	2.6	n.a.	n.a.	n.a.	n.a.	3.06	1160	3500	2.3
120	2.23	0.032	5	2.8	2.10	0.092	3500	1.3	2.13	360	n.a.	n.a.
135	2.24	0.021	5	4.2	2.12	0.084	3500	1.4	1.74	217	n.a.	n.a.
150	2.37	0.015	5	6.2	2.17	0.054	3500	2.3	2.16	152	n.a.	n.a.
180	2.76	0.011	5	9.4	n.a.	n.a.	n.a.	n.a.	2.48	51	n.a.	n.a.

Additionally the workability of the concept for the Brent Delta location is determined to be at least 61% for the summer period, the critical wave angle being 120°. For an incoming wave angle of 180° the workability increases to 88%. Depending on the orientation of the platform and the wave angle the workability will lie between these two values. The calculated design wave height and the value for the workability indicate that the concept is technically feasible for the conditions of the northern North Sea.

7.2. RECOMMENDATIONS

Three main recommendations can be made to improve future research.

First of all, the wave input used in this thesis is based on hindcast data of the Brent field in the northern North Sea. From the measured energy spectra only the Tp and Hs value are extracted, omitting valuable information. The values of Hs and Tp are then used to create a JONSWAP spectrum, which is subsequently used to calculate the vessels' response. Although the JONSWAP spectrum generally represents the conditions in the North Sea, it can be imagined that using the actual wave energy spectra to calculate the workability, gives more realistic results. The actual hindcast data is available and can be bought from naval institutions. Not only will it give more realistic results, also the effect of using a JONSWAP spectrum approach can be investigated. The data as it is used now furthermore does not take into account wave spreading. Including this effect would already result in a more realistic outcome.

Secondly, a more extensive research on the topic of the impact velocity is advised. The maximum impact velocity value is assumed to be $0.2m/s$ but depends on the topsides, the use of LMUs and the lifting configuration. Additionally an assessment can be performed on the influence of the impact on the motions of the vessels, as this influence is now neglected.

Lastly, scaled model tests of the novel decommissioning concept are highly recommended. The additional roll damping and the incorporated damping lid can in this way be justified. The damping value of the external lid is of influence on the limiting motions. Between a damping value of $\epsilon = 0.01$ and $\epsilon = 0.05$ a difference in the impact velocity of about 4% can be experienced. For the axial connection force this difference can go up to 22%. The hydrodynamic coupling between the barges can be compared to the results of ANSYS Aqwa and that information can be used to improve the dynamical model. Although ANSYS Aqwa and Orcaflex are software programs used commercially throughout the maritime industry, the models still need to be validated. Experimental results would be recommended to do this.

Bibliography

- [1] Allseas B.V. Allseas equipment: Pioneering spirit, 2018. Available at <https://allseas.com/equipment/pioneering-spirit/>.
- [2] ANSYS Aqwa. *ANSYS Aqwa Line Reference Manual Release 14.5*. 2012.
- [3] ARUP, Scottish Enterprise, Decom North Sea. *Decommissioning in the North Sea*. 2003. Technical report.
- [4] BOSKALIS. *BOKA Vanguard equipment sheet*. Boskalis, 2018. Available at <https://boskalis.com/download-center/>.
- [5] S. Chakrabarti. *Emperical calculation of roll damping for ships and barges*, volume 28. Pergamon, 2001.
- [6] X.-B. Chen. *Hydrodynamic analysis for offshore LNG terminals*. Research Department BUREAU VERITAS, 2005.
- [7] D. Clades. *Developing a method to assess the workability of an offshore heavy lifting operation*. TU Delft, 2018.
- [8] Y. Dalgic, I. Lazakis, and O. Turan. *Vessel charter rate estimation for offshore wind O and M activities*. 2013.
- [9] H. de Koning Gans. *Introduction of numerical methods in ship hydromechanics*. Delft University of Technology, 2012.
- [10] Det Norske Veritas. *DNV-RP-H103: Modelling and Analysis of Marine Operations*. Thomson, Brooks/Cole, 2011.
- [11] Det Norske Veritas. *Rules for Ships*. Thomson, Brooks/Cole, 2012.
- [12] Det Norske Veritas. *DNVGL-SE-0080 Rules for transportation*. Thomson, Brooks/Cole, 2016. Available at <http://rules.dnvgl.com/docs/pdf/g1/nobledenton>.
- [13] S. S. Dhavalikar and A. Negi. *Estimation of roll damping for transportation barges*. Proceedings of the ASME 28th International Conference on Ocean, Offshore and Arctic Engineering, 2009.
- [14] S. S. Dhavalikar and A. Negi. *Stability and motion analysis for barges*. National Conference on Computer Aided Modelling and Simulation in Computational Mechanics, 2009.
- [15] D. I. Dmitrieva. *Delfrac; 3D potential theory including wave diffraction and drift forces acting on the structures*. Delft University of Technology, 1994.
- [16] O. M. Faltinsen. *Sea loads on ships and offshore structures*. Cambridge University Press Cambridge ; New York, 1990.
- [17] J.-R. Fournier, M. Naciri, and X.-B. Chen. *Hydrodynamics of two side-by-side vessels; experiments and numerical simulations*. 2006.
- [18] K. Hasselmann, T. Barnett, E. Bouws, H. Carlson, D. Cartwright, K. Enke, J. Ewing, H. Gienapp, D. Hasselmann, P. Kruseman, A. Meerburg, P. Mller, D. Olbers, K. Richter, W. Sell, and H. Walden. *Measurments of Wind-Wave Growth and Swell Decay during the Joint North Sea Wave Project (JONSWAP)*. Deutschen Hydrographischen Zeitschrift Nr. 12, 1973.
- [19] IHS Markit. *IHS Markit Offshore Decommissioning Study Report*. 2016. Available at <http://news.ihsmarkit.com/press-release/energy-power-media/decommissioning-aging-offshore-oil-and-gas-facilities-increasing-si>.

- [20] Indian Register of Shipping. *Rules and regulations for the construction and classification of steel ships Part 3 – General Hull Requirements*. 2008.
- [21] J. Journee and W. Massie. *Offshore Hydromechanics*. Delft University of Technology, 2001.
- [22] M. J. Kaiser and B. Snyder. *The five offshore drilling rig markets*, volume 39. 2013.
- [23] V. J. Katz. *The History of Stokes' Theorem*, volume 52. Mathematical Association of America, 1979.
- [24] A. G. Kemp and L. Stephen. *Prospective Decommissioning Activity and Infrastructure Availability in the UKCS*. 2011.
- [25] C. Lee and P. Sclavounos. *Removing the irregular frequencies from integral equations in wave-body interactions*. Journal of Fluid Mechanics, pp. 393-418, 1989.
- [26] V. A. Mathios. *Hydrodynamic Assessment and Motion Optimization of Mechanically Coupled Barges*. 2015. Master Thesis Offshore and Dredging Engineering.
- [27] V. Monbet, P. Ailliot, and M. Prevosto. *Survey of stochastic models for wind and sea state time series*, volume 22. 2007.
- [28] J. N. Newman and P. D. Sclavounos. The computation of wave loads on large offshore structures. 1988.
- [29] Oil and Gas UK. *Decommissioning Insight Report*. 2013. The UK Oil and Gas Industry Association Limited trading as Oil and Gas UK.
- [30] Oslo-Paris convention. *Inventory of Offshore Installations*. 2013. Available at http://www.ospar.org/content/content.asp?menu=01511400000000_000000_000000.
- [31] W. H. Pauw, R. H. Huijsmans, and A. Voogt. *Advances in the hydromechanics of side-by-side moored vessels*. Jun 2007.
- [32] B. Peña and A. McDougall. *An investigation into the limitations of the panel method and the gap effect for a fixed and a floating structure subject to waves*. 2016.
- [33] Royal Dutch Shell. *Offshore Metocean Design and Operational Criteria, Brent D platform*. 2012.
- [34] J. Stewart. *Calculus, early transcendentals, 6th edition*. Thomson, Brooks/Cole, 2008.
- [35] N. L. M. Verhoef. *Optimization of the skidded load-out process*. 2017. Master Thesis Offshore and Dredging Engineering.
- [36] S. Wang. *Multibody Dynamic Analysis of the Lift-Off Operation*. 2015. Master Thesis Offshore and Dredging Engineering.
- [37] J. Wehausen and E. Laitone. *Surface Waves*. Handbuch der Physik. Springer-Verlag, 1960.
- [38] X. Xu, J.-M. Yang, X. Li, and L. Xu. *Hydrodynamic performance study of two side-by-side barges*, volume 9. Taylor and Francis, 2014.

A | Assessment on the influence of non-linear connection beams

A.1. NONLINEARITIES

To assess the influence of nonlinearities, a time-domain simulation of the simplified 2D model will be made where the added mass and damping are estimated and assumed to be constant over all frequencies. Also the hydrodynamic coupling of both barges is neglected. For the sake of simplicity this model will only take into account the heave, sway and roll motion as this model is only used to assess the effect of the nonlinearities. The system's RAO will then be calculated for the linearized case and compared to the motions of the nonlinear case for a wave amplitude of 1 m . An overview of the simplified model is given in Figure A.1. It has to be stated again that this simplified model is only to show the differences between a linear and nonlinear model and therefore does not represent the real motions of the vessels.

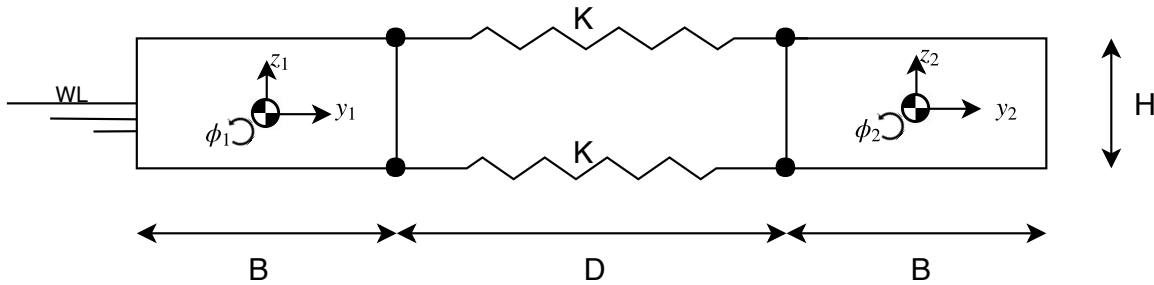


Figure A.1: Simplified model

To come up with the equations of motion the Lagrange method is used. This method uses the kinetic and potential energy of the system to come up with the Lagrangian of the system:

$$L = T - V \quad (\text{A.1})$$

Where T is the kinetic and V is the potential energy. The equations of motion for a system with n degrees of freedom can then be found with:

$$\frac{d}{dt} \frac{\partial L}{\partial \dot{q}_i} - \frac{\partial L}{\partial q_i} = 0 \quad (i = 1, \dots, n) \quad (\text{A.2})$$

KINETIC ENERGY

The generalized equation to determine the kinetic energy of the system is given as:

$$T = \frac{1}{2} \cdot m_i \cdot v_i^2 \quad (i = 1, 2) \quad (\text{A.3})$$

Where m is the mass and v is the velocity. For rotations this mass changes to a mass moment of inertia and the velocity changes to a rotational velocity. The total kinetic energy is a summation of the kinetic energy of all degrees of freedom.

POTENTIAL ENERGY

The potential energy of the barges without connections is given as

$$V = \frac{1}{2} \cdot k_j \cdot \epsilon_j^2 + m_i \cdot g \cdot h_i \quad (i = 1, 2) \quad (j = 1, \dots, n) \quad (\text{A.4})$$

Where k_i is the spring stiffness of each degree of freedom and ϵ_i the elongation of the matching spring. The second part of the equation represents the gravitational potential energy for each of the barges.

It has to be stated that till now the potential and kinetic energy of both the linear and nonlinear system are the same for small motions.

A.1.1. LINEAR CASE

In Figure A.2 the elongation of the springs due to the roll motion of the left barge is made visible. For a certain angle ϕ there will be a displacement of point A in both y- and z-direction resulting in the elongation of the spring. It also has to be pointed out that the elongation of the upper and lower spring due to this angle are not the same. To calculate the potential energy, the elongation of each of the total of 4 springs should be expressed in terms of all motions.

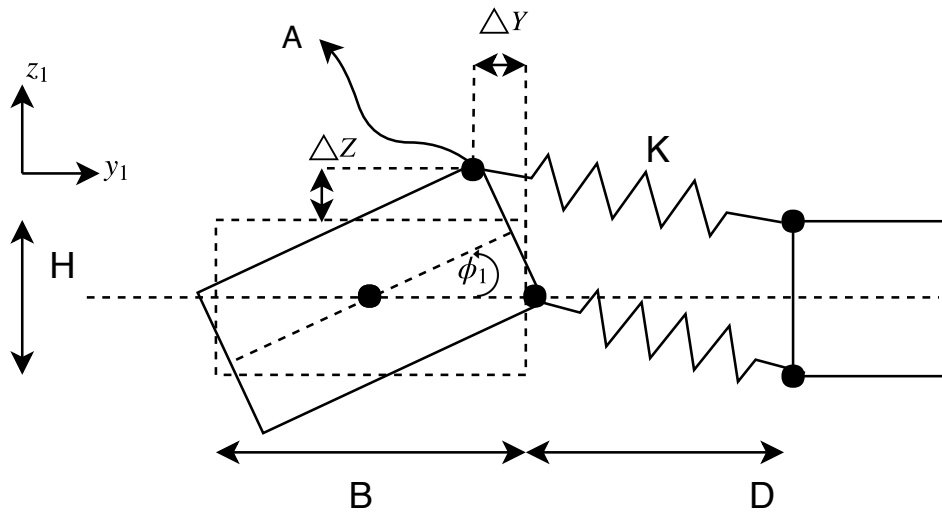


Figure A.2: Elongation of connections

For a linearized spring only the elongation in the axial direction of the spring will result in a reactive force and therefore a change in potential energy. The exact y-coordinate of point A is then given by:

$$y_1 = \Delta y_1 - z_p \cdot \sin(\phi_1) + y_p \cdot \cos(\phi_1) \quad (\text{A.5})$$

Assuming small rotations and translations the $\sin(x)$ and $\cos(x)$ functions can be replaced using the first linear term of their Taylor series, respectively x and 1 . This results in the following formula for:

$$y_1 = \Delta y_1 - z_p \phi_1 + y_p \quad (\text{A.6})$$

Which results in the elongation of the spring ϵ .

$$\epsilon = -\Delta y + z_p \cdot \Delta \phi \quad (\text{A.7})$$

Taking the motions of both barges into account this formula will change to:

$$\epsilon = \Delta y_2 - \Delta y_1 + z_p \cdot (\Delta \phi_1 - \Delta \phi_2) \quad (\text{A.8})$$

Where z_p is the z coordinate of the connection points. It can be seen that the elongation of the 4 springs is not the same. This is the result of the changing coordinates of the connections points of each spring. The change in potential energy due to elongation for each of the springs is now given by:

$$V = \frac{1}{2} \cdot k \cdot \epsilon^2 \quad (\text{A.9})$$

Now that all the contributions to the kinetic and potential energy are known, the equations of motion for the linear system can be formed by substituting the Lagrangian in equation A.2. The system of equations is solved using MAPLE and results in the following force matrix:

$$[F] = \begin{bmatrix} (2.0 H\phi_1(t) - 2.0 H\phi_2(t) + 4.0 y_2(t) - 4.0 y_1(t)) k \\ -m_1 g - k z z_1(t) \\ -kphi\phi_1(t) + 2.0 k (-1.0 y_2(t) + y_1(t) - 0.5 H\phi_1(t) + 0.5 H\phi_2(t)) H \\ (-2.0 H\phi_1(t) + 2.0 H\phi_2(t) - 4.0 y_2(t) + 4.0 y_1(t)) k \\ -m_2 g - k z z_2(t) \\ -kphi\phi_2(t) - 2.0 k (-1.0 y_2(t) + y_1(t) - 0.5 H\phi_1(t) + 0.5 H\phi_2(t)) H \end{bmatrix}$$

Where $kphi$ is the restoring force of the vessels in roll direction and kz is the restoring force in heave direction. The matrix is linear as there are no nonlinear terms.

A.1.2. NONLINEAR CASE

In the nonlinear case only the potential spring energy changes with respect to the linear case. Now also the elongation of the connections due to the movement of the connection points in z-direction is taken into account. The motions of a connection point with location $[y_p, z_p]$ are given by:

$$z_1 = \Delta z_1 + y_p \cdot \sin(\phi_1) + z_p \cdot \cos(\phi_1) \quad (\text{A.10})$$

And:

$$y_1 = \Delta y_1 - z_p \cdot \sin(\phi_1) + y_p \cdot \cos(\phi_1) \quad (\text{A.11})$$

The motions of both connection points have to be determined to calculate the elongation of the connection beams. This elongation can be calculated by taking the distance between the two points and subtracting the original length of the connections using Pythagoras theorem.

$$\epsilon = \sqrt{(z_2 - z_1)^2 + (y_2 - y_1)^2} - D \quad (\text{A.12})$$

Where D is the original length of the spring. The potential energy of each spring can be found with equation A.9. The equations of motion can be found the same way as for the linear case but will result in a more complex system due to the coupling terms.

A.1.3. WAVE PRESSURE INTEGRATION

Now that the equations of motion for both cases are known, a wave force will be added to assess the reaction of both systems. This wave force will be approximated by integrating the wave pressure of only the incident wave over the wet surface of the barges, also known as the Froude-Krylov force. Radiation and diffraction effects will be ignored for the sake of simplicity. To calculate the RAO's the calculation will be performed for a number of frequencies. For each frequency the following relationship between the period and the wavenumber is used:

$$\lambda = \frac{g}{2\pi} \cdot T^2 = 1.56 \cdot \left(\frac{2\pi}{\omega}\right)^2 \quad (\text{A.13})$$

The force in the sway direction is given as:

$$F_y = Re \int_{-T}^0 \rho \frac{\omega^2}{k} \zeta e^{kz} \left[e^{i(\omega t - kB/2)} - e^{i(\omega t + kB/2)} \right] dz \quad (\text{A.14})$$

In the same way the Froude-Krilov force can be found in vertical direction.

$$F_z = Re \int_{-B/2}^{B/2} \rho \frac{\omega^2}{k} \zeta e^{-kT} e^{i(\omega t - ky)} dy \quad (\text{A.15})$$

Where T is the draught of the barge and ζ is the wave amplitude. The roll moment due to the Froude-Krilov force can be found by simply multiplying the inside of the integral with the arm of the force y :

$$M_x = Re \int_{-B/2}^{B/2} y \rho \frac{\omega^2}{k} \zeta e^{-kT} e^{i(\omega t - ky)} dy \quad (\text{A.16})$$

Of course the forces on the second barge will be the same except for a phase difference equal to ky : the term in the exponent of e . The roll moment due to the force in sway direction is assumed to be small and therefore not taken into account in the calculation.

A.1.4. DAMPING

Now that the mass and force-matrix are known, only the damping has to be added to the system. In reality this damping is frequency dependent, but, again for the sake of simplicity, the damping is assumed to be constant. The values of the damping are approximated by taking 10% of the critical damping as value for heave, 10% of the critical damping for roll and 20% of the heave damping for the sway damping. These values are merely approximations of the real damping values. The same values are used for both the nonlinear and the linear model.

A.1.5. RESULTS

The system of differential equations that now has to be solved is of the form:

$$\begin{bmatrix} M_1 & 0 & 0 & 0 & 0 & 0 \\ 0 & M_1 & 0 & 0 & 0 & 0 \\ 0 & 0 & Jx_1 & 0 & 0 & 0 \\ 0 & 0 & 0 & M_2 & 0 & 0 \\ 0 & 0 & 0 & 0 & M_2 & 0 \\ 0 & 0 & 0 & 0 & 0 & Jx_2 \end{bmatrix} \cdot \begin{bmatrix} \dot{y}_1 \\ \dot{z}_1 \\ \dot{\phi}_1 \\ \dot{y}_2 \\ \dot{z}_2 \\ \dot{\phi}_2 \end{bmatrix} + \begin{bmatrix} B_1 & 0 & 0 & 0 & 0 & 0 \\ 0 & B_2 & 0 & 0 & 0 & 0 \\ 0 & 0 & B_3 & 0 & 0 & 0 \\ 0 & 0 & 0 & B_4 & 0 & 0 \\ 0 & 0 & 0 & 0 & B_5 & 0 \\ 0 & 0 & 0 & 0 & 0 & B_6 \end{bmatrix} \cdot \begin{bmatrix} y_1 \\ z_1 \\ \phi_1 \\ y_2 \\ z_2 \\ \phi_2 \end{bmatrix} = \begin{bmatrix} F_1 \\ F_2 \\ F_3 \\ F_4 \\ F_5 \\ F_6 \end{bmatrix}$$

The force matrix consists of the connection and wave forces and is therefore a function of the displacements. The nonlinear terms in the nonlinear case will be found in this force matrix. The system will be solved using an ordinary differential equation (ODE) solver in MATLAB. The initial displacements and velocities will be given to the system, after which the accelerations can be calculated for the first time step. This acceleration is then used to calculate the displacements and velocities at the next time step and so on. The amplitude of the wave force is linearly increased to $1m$ over a time span of 50 seconds. In Figure A.3 a time series of the roll motion of both barges is shown. It can be seen that the roll motion is almost exactly coupled due to the connections. The time series approaches a steady state solution. The normalized motions can now be calculated by taking the maximum roll angle during this steady state motion and dividing it by the wave amplitude. The motions are calculated for a system of barges with dimensions $B = 57m$, $D = 60m$ and $H = 10m$ which are roughly the dimensions of the Iron Lady.

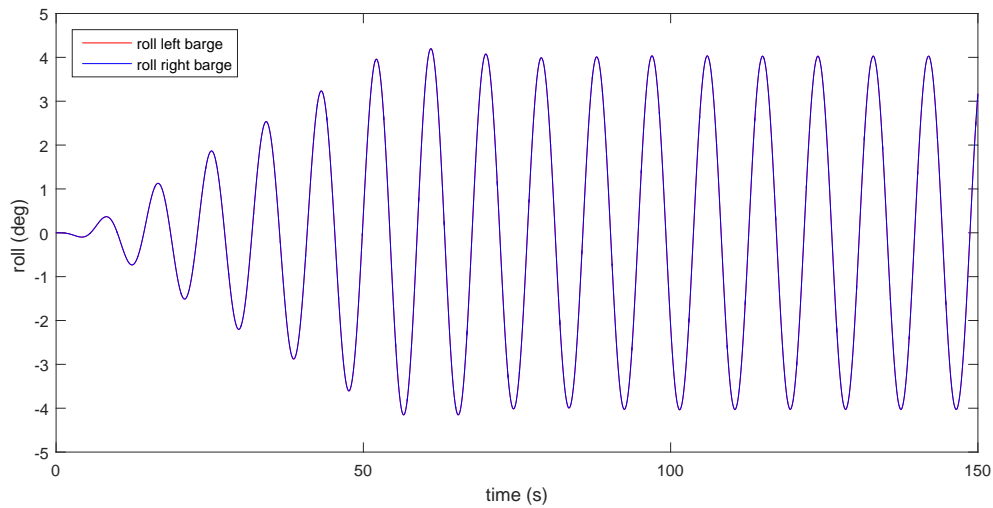


Figure A.3: Timeseries roll motion for a wave with an amplitude of 1 m, and a 9 s period

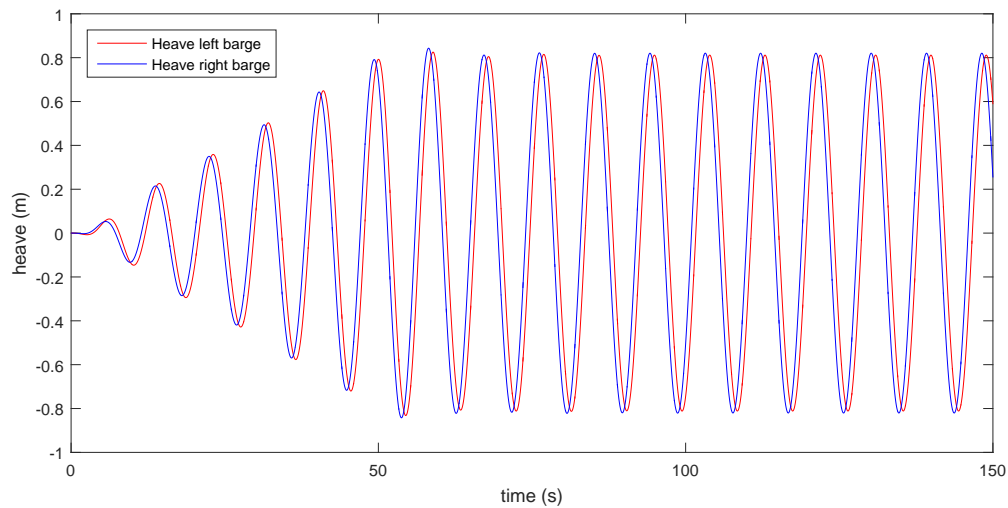


Figure A.4: Timeseries heave motion for a wave with an amplitude of 1 m, and a 9 s period

In Figure A.4 a time series is shown for the heave motion of both barges for the same wave. It can be seen that the amplitude is the same for both barges. For a 9 s wave the wavelength is 126 m which is a little over the distance between the centres of the barges. This is why a phase-difference can be noticed.

In Figure A.5 the normalized heave motion for a wave amplitude of 1 m is given for both the linear and the nonlinear case. It can be seen that the difference between the two is not significant. Still, some nonlinear effects can be seen.

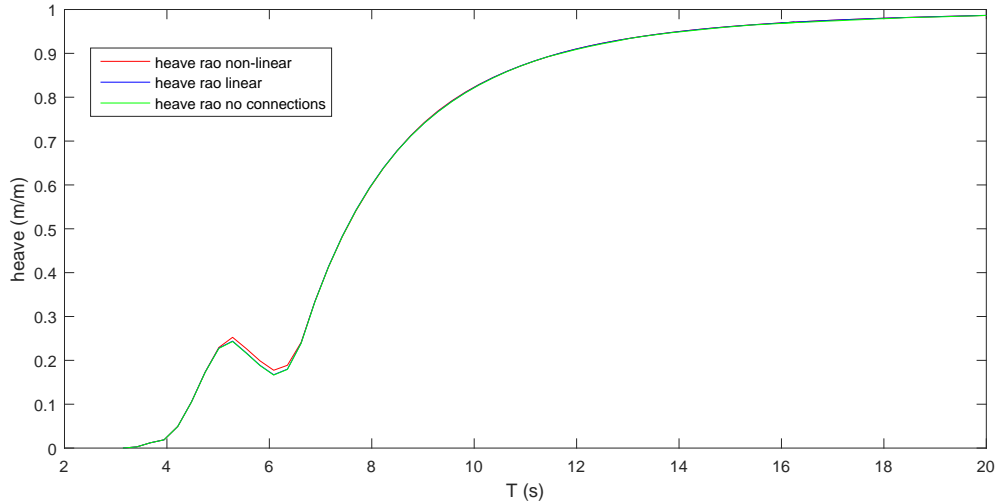


Figure A.5: Normalized heave motion for a wave amplitude of 1 m

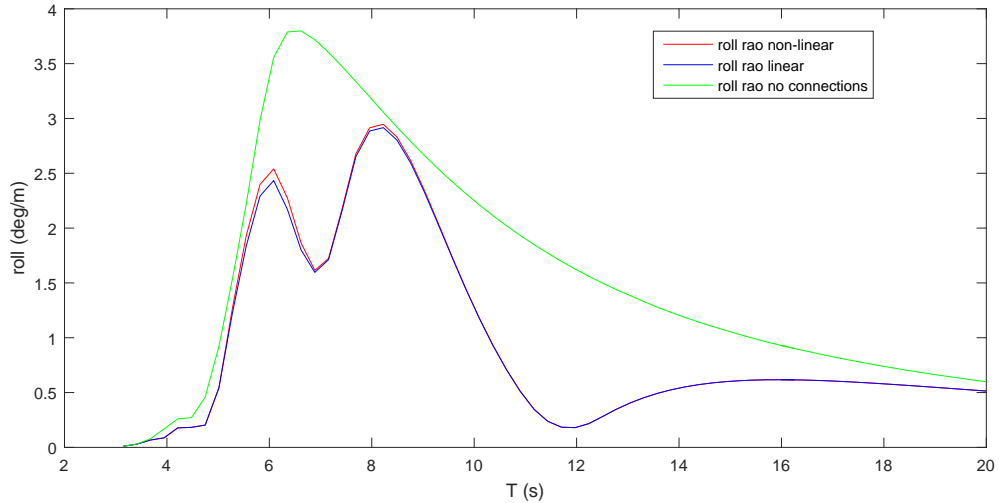
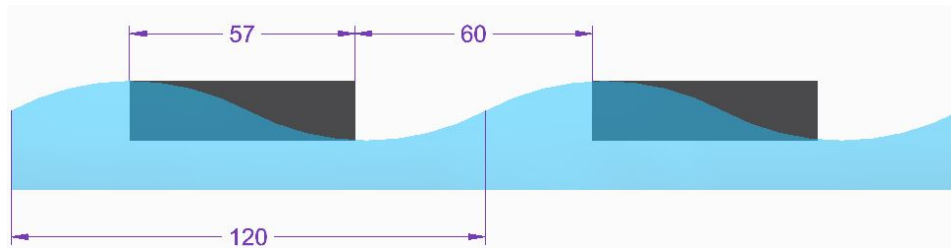


Figure A.6: Normalized roll motion for a wave amplitude of 1 m

When we look at the normalized roll motion in Figure A.6, also small differences between the two systems can be seen. The two peaks coincide with wavelengths of approximately $60m$ and $120m$. Drops in the roll motion can be found around at wavelengths of approximately $90m$ and $240m$. One should note that normalized motions for the case where no connections are used and the linear case both remain the same for whatever increase in amplitude. This is the result of the linearization and is the reason that a frequency domain solution is possible for these cases as explained in 3.2.1. For the nonlinear case however, this does not hold. Increasing the wave amplitude will result in larger deviation between both models. Still it is expected that the vessels will not operate in large wave amplitudes.

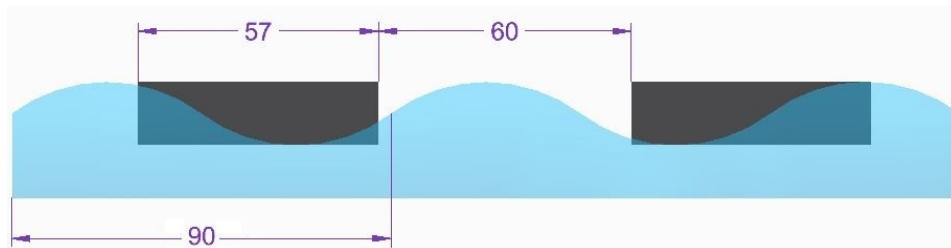
$\lambda = 60m$ AND $\lambda = 120m$

The peaks at $60m$ and $120m$ can be explained because the wavelength fits exactly in the distance between the barges, therefore exerting an in-phase roll force on both barges. In the nonlinear case a combination of sway forces and coupling between the roll and sway motion results in bigger roll motions.

Figure A.7: $\lambda = 120m$

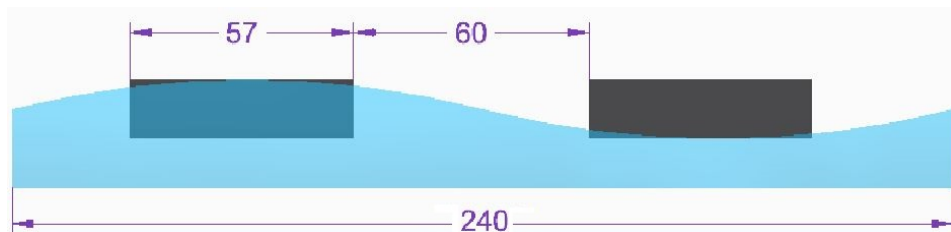
$\lambda = 90m$

The first drop in the roll motion happens at a wavelength of approximately three third times the distance between the centres of the barges. The roll motion is therefore out of phase: both roll motions cancel each other out.

Figure A.8: $\lambda = 90m$

$\lambda = 240m$

The second drop in the motions happens at a wavelength of approximately two times the distance between the centres of the barges. The roll motion is therefore again out of phase: both roll motions cancel each other out.

Figure A.9: $\lambda = 240m$

CONNECTION STRESSES

In Figure A.10 the stresses in the connections are shown. These are calculated for a cross-sectional area of the connection of $0.5m^2$ and a Young's module of the material of $210 \cdot 10^9 \frac{N}{m^2}$. This is merely to show that the stresses in the connections are of reasonable proportions. Increasing the moment arm of the connections or the amount of connections will decrease these stresses even further.

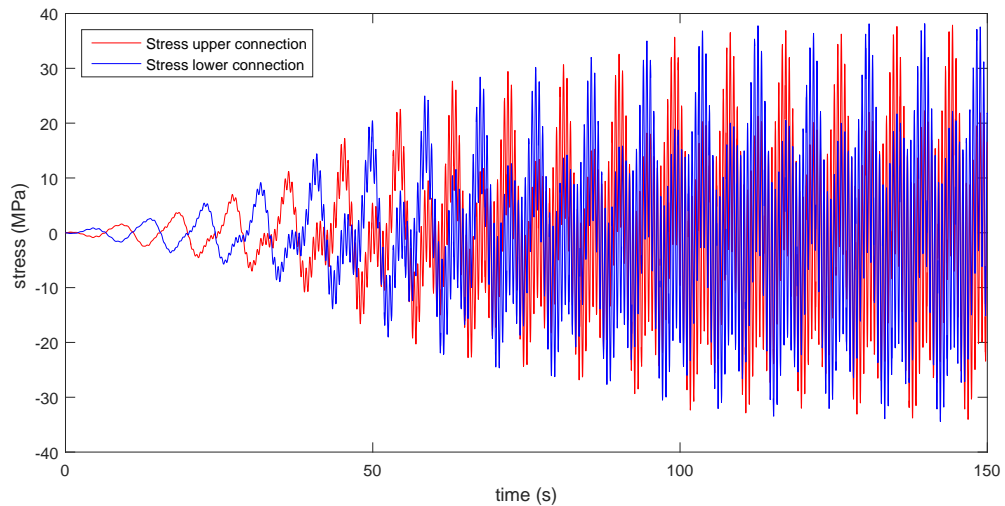


Figure A.10: Stresses in connections for a wave amplitude of 1 m, a distance of 60 m and a period of 9 s

A.1.6. DISCUSSION

The previous results show that the barges are successfully coupled mechanically. For certain dimensions this results in an improved hydro dynamical behaviour. Most of the time the differences between the linear and nonlinear model are not significant at all. For certain dimensions, wavelengths and wave heights however, the difference does become significant. The question arises if these differences will still be significant when determining the motions of the system for a complete sea state. Will the inclusion of frequency dependent added-mass and potential damping enlarge these differences, or will it rather bring both models closer together?

Additionally the shape of the graph of the normalized vessel motions is the same for both the linear and nonlinear case: maximum and minimum motions are occurring at the same wave frequencies. When the goal of this model is to determine what the most optimal dimensions of the system are, the conclusion might be very well the same for both the linear and the nonlinear case, although the maximum and minimum motions still can be different. If this is really the case should be investigated.

B | Potential theory and ANSYS Aqwa

Potential theory in essence simplifies real flow by making certain assumptions. It can be used in hydrodynamics by picturing the hull of a floating body to be in a potential flow field. When this flow field is known the forces on the body due to this flow field can be calculated.

B.1. EQUATIONS OF MOTION

The equations of motion of a floating body are given by:

$$\sum_{i=1}^6 \left\{ -\omega^2(m_{ki} + a_{ki}) - i\omega b_{ki} + c_{ki} \right\} \cdot X_i = F_k \quad \text{for } k = 1, \dots, 6 \quad (\text{B.1})$$

where:

m = mass/inertia matrix

a = added mass/inertia matrix

b = damping matrix

c = stiffness matrix

X = body motion for each degree of freedom

F = wave force on the floating body

The added mass, damping and wave force are unknown in this equation and have to be determined for each frequency. To do this the principle of potential theory is used. Potential theory uses Green's Theorem to calculate this flow. Therefore first, a closer look is given at Green's theorem.

B.2. GREEN'S THEOREM

If there exists an arbitrary area R in a 2D vector field F, then the rotation of the fluid flow represented by the vector field is given by the line integral around the curve C. This is illustrated in Figure B.1.

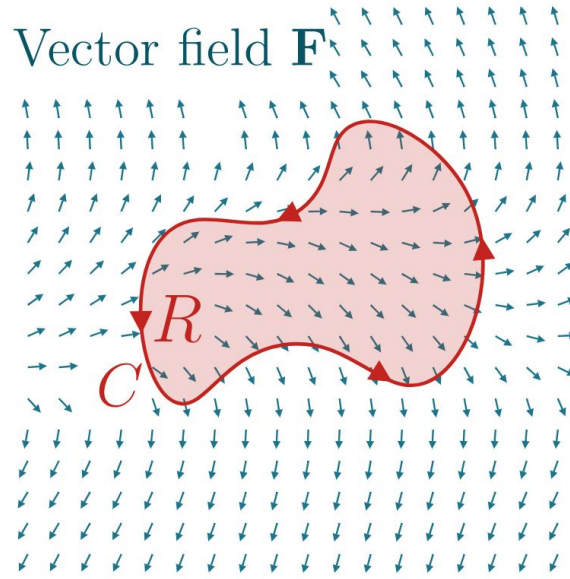


Figure B.1: Vector field illustration [Courtesy of Khan Academy]

Each vector in the vector field F consists of an x and an y component. The vectors can therefore be written as:

$$dr = dx \cdot \tilde{i} + dy \cdot \tilde{j} \quad (\text{B.2})$$

With the line integral being:

$$\oint_C F dr \quad (\text{B.3})$$

If the minimum and maximum x coordinates of the line over which the integral is taken are now $[a, b]$, the line can be split up in two parts. The upper line between point a and b , $y_2(x)$, and the lower line between b and a , $y_1(x)$. The line integral for a vector field P with only x -components can now be written as:

$$\oint_C P(x, y) dx = \int_a^b P(x, y_1(x)) dx + \int_b^a P(x, y_2(x)) dx \quad (\text{B.4})$$

Which can be rewritten as:

$$\oint_C P(x, y) dx = \int_a^b P(x, y_1(x)) - \int_a^b P(x, y_2(x)) dx \quad (\text{B.5})$$

Which results in:

$$\oint_C P(x, y) dx = \int_a^b \left(P(x, y_1(x)) - P(x, y_2(x)) \right) dx \quad (\text{B.6})$$

The integral can then be evaluated as:

$$\begin{aligned} \oint_C P(x, y) dx &= - \int_b^a P(x, y) \Big|_{y_1(x)}^{y_2(x)} dx \\ &= - \int_b^a \int_{y_2(x)}^{y_1(x)} \frac{\partial P}{\partial y} dy dx \end{aligned} \quad (\text{B.7})$$

This can be seen as the integral over the area/region R. So the line integral of F over C is the same as the integral over the whole area R:

$$\oint_C P(x, y) dx = - \iint_R \frac{\partial P}{\partial y} dy dx \tag{B.8}$$

If the same procedure is applied for a vector field Q that only has vectors in y- direction the result will be:

$$\oint_C Q(x, y) dx = \int_b^a \int_{x_1(x)}^{x_2(x)} \frac{\partial Q}{\partial x} dx dy \tag{B.9}$$

Depending on whether the line integral is taken clockwise or counter clockwise, the minus sign will change for the integrals of Q and P.

What this eventually means is that if there is a vector field with both x- and y- components, this vector field can be written as the summation of an x-vector and an y-vector field. The same will then hold for the line integral of a line crossing this vector field. This results in Green's Theorem [34, chapter 16.4]:

$$\oint_C F dr = \iint_R \left(\frac{\partial Q}{\partial x} - \frac{\partial P}{\partial y} \right) dA \tag{B.10}$$

It relates the line integral of a line C in a vector field F to the double integral over the area R covered by this same line. The same trick can now be performed if the area R is split up in multiple smaller areas. If the number of elements is increased to infinity two things will happen. The first is that the meaning of the line integral over such an element will represent the *curl* of such an element. The second is that across the boundaries between the elements the line integrals will cancel each other out. This can be seen in Figure B.2, where the arrows inside the total area C point in the opposite direction of the neighbouring arrow.

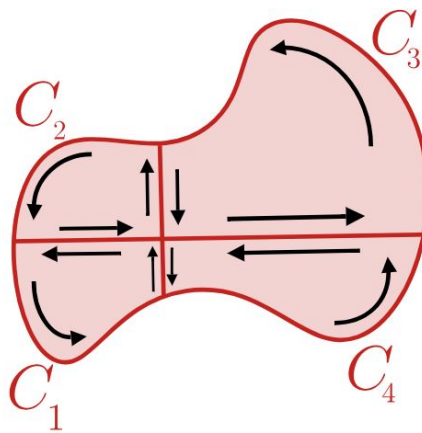


Figure B.2: Area R, divided in four areas [Courtesy of Khan Academy]

This means that the summation of the line integrals of all elements will be equal to the line integral of the total area. Therefore the summation of the curl of all areas will be represented by the line integral of the total area. This means:

$$Curl = \iint_R \left(\frac{\partial Q}{\partial x} - \frac{\partial P}{\partial y} \right) dA \tag{B.11}$$

In potential theory this equation is critical as it is assumed that the curl of the flow is zero. The underlying theory, although in another form, was already discovered by Joseph-Louis Lagrange in 1762 [23], see equation

B.12. The formula relates the divergence of a vector field to the surface integrals of the flux of this same vector field. The total integrated flow in an volume V is equal to the integration of the vectorfield alongside the boundary S of this volume. It was later rediscovered by Carl-Friedrich Gauss (1813) and Mikhail Vasilievich Ostrogradsky (1831). Therefore it also goes by the name of the theorem of Gauss, the theorem of Ostrogradsky, or simply the divergence theorem.

$$\iiint_V (\nabla \cdot \vec{F}) dV = \iint_S \vec{F} \cdot d\vec{S} \quad (\text{B.12})$$

The function also relates closely to Stokes' theorem (1854) and thus the theory of George Green (1825).

B.3. POTENTIAL THEORY

In potential theory the vector fields are now represented by velocity potentials of the fluid denoted with Φ . These are vector fields representing the gradient of the velocity potential. Potential flow is an approximation or simplification of a real flow. It is assumed that the flow is frictionless, irrotational ($\text{curl} = 0$) and incompressible. Using these assumptions, still valuable approximations can be made for many applications, such as ship hydrodynamics. Potential theory has been explained extensively in the past. Many different articles and books exist disclosing the thoughts behind potential theory. The main literature used to explain potential theory in this thesis is provided by [21], [15], [9], [28], [16] and [37].

LAPLACE EQUATION

Inside a differential fluid element the conservation of mass equation for potential flow is given as:

$$\frac{\partial u}{\partial x} + \frac{\partial v}{\partial y} + \frac{\partial w}{\partial z} = 0 \quad (\text{B.13})$$

Meaning that the total in and outward flow in a given boundary is always equal to zero. No mass is added to or subtracted of the given boundary, as the flow is incompressible (the fluid density is a constant ρ). The velocity of the flow in a certain direction can be calculated by taking the derivative of the potential in that direction. Using this characteristic and substituting it in Equation B.13 results in:

$$\frac{\partial^2 \Phi}{\partial x^2} + \frac{\partial^2 \Phi}{\partial y^2} + \frac{\partial^2 \Phi}{\partial z^2} = \Phi_{xx} + \Phi_{yy} + \Phi_{zz} = \nabla^2 \Phi = 0 \quad (\text{B.14})$$

This is known as the Laplace equation which has to be satisfied for a potential flow.

EULER EQUATIONS

When Newton's second law is applied to non-viscous and incompressible fluids, the Euler equations can be derived, named after Leonard Euler who performed this exercise. The equations are given by:

$$\begin{aligned} \frac{\partial u}{\partial t} + u \frac{\partial u}{\partial x} + v \frac{\partial u}{\partial y} + w \frac{\partial u}{\partial z} &= -\frac{1}{\rho} \cdot \frac{\partial p}{\partial x} && \text{in x-direction} \\ \frac{\partial v}{\partial t} + u \frac{\partial v}{\partial x} + v \frac{\partial v}{\partial y} + w \frac{\partial v}{\partial z} &= -\frac{1}{\rho} \cdot \frac{\partial p}{\partial y} && \text{in y-direction} \\ \frac{\partial w}{\partial t} + u \frac{\partial w}{\partial x} + v \frac{\partial w}{\partial y} + w \frac{\partial w}{\partial z} &= -\frac{1}{\rho} \cdot \frac{\partial p}{\partial z} && \text{in z-direction} \end{aligned} \quad (\text{B.15})$$

BERNOULLI EQUATION

Daniel Bernoulli, another great mathematician, used the Euler equations to come up with an energy relation. The velocity terms in the Euler equation can be expressed in term of the velocity potential as follows:

$$u \frac{\partial u}{\partial x} = \frac{\partial \Phi}{\partial x} \cdot \frac{\partial^2 \Phi}{\partial x^2} = \frac{1}{2} \cdot \frac{\partial}{\partial x} \left(\frac{\partial \Phi}{\partial x} \right)^2 \quad (\text{B.16})$$

The same can be done for the velocities in y- and z-direction. Substituting these velocities into the Euler equations results in the Bernoulli equation for an instationary flow:

$$\frac{\partial \Phi}{\partial t} + \frac{1}{2} V^2 + \frac{p}{\rho} + gz = C(t) \quad (\text{B.17})$$

in which:

$$V^2 = \left(\frac{\partial \Phi}{\partial x} \right)^2 + \left(\frac{\partial \Phi}{\partial y} \right)^2 + \left(\frac{\partial \Phi}{\partial z} \right)^2 \quad (\text{B.18})$$

This equation is later on used as a boundary condition.

VESSEL DOMAIN

Now consider two separate potential functions, Φ_j and Φ_k , and consider a floating body in a cylindrical tank with diameter R as is illustrated in Figure B.3.

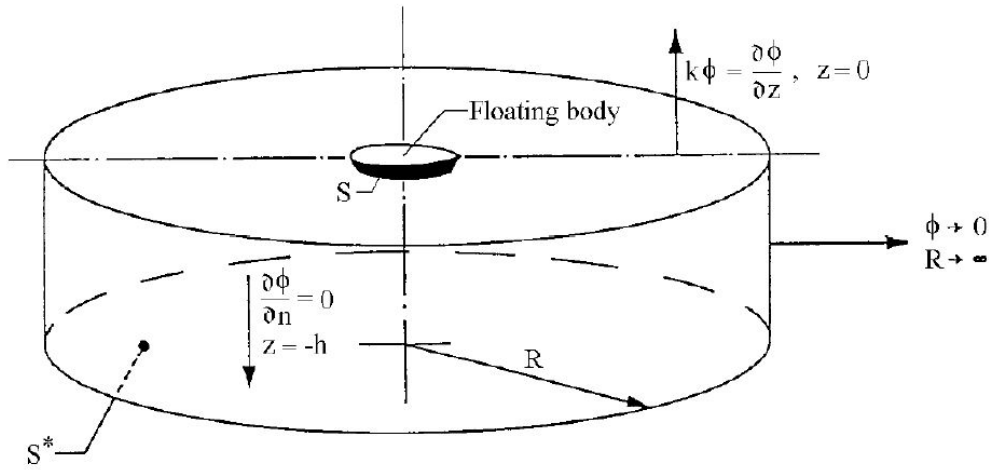


Figure B.3: Boundaries of the vessel domain [21]

Using the divergence theorem from equation B.12, the following holds:

$$\iiint_V (\Phi_j \nabla^2 \Phi_k - \Phi_k \nabla^2 \Phi_j) dV = \iint_{S^*} \left(\Phi_j \cdot \frac{\partial \Phi_k}{\partial n} - \Phi_k \cdot \frac{\partial \Phi_j}{\partial n} \right) \quad (\text{B.19})$$

Satisfying the Laplace equation:

$$\Phi_j \nabla^2 = \Phi_k \nabla^2 = 0 \quad (\text{B.20})$$

Equation B.19 now becomes:

$$\iint_{S^*} \left(\Phi_j \cdot \frac{\partial \Phi_k}{\partial n} \right) = \iint_{S^*} \left(\Phi_k \cdot \frac{\partial \Phi_j}{\partial n} \right) \quad (\text{B.21})$$

Where S^* is the surface enclosed by:

1. Vertical wall of the cylinder with radius R.
2. Sea bottom.

3. Water surface.
4. Wetted surface of the floating body.

B.3.1. BOUNDARY CONDITIONS

The flow inside the domain should comply with certain boundary conditions. At the free surface two boundary conditions apply; the kinematic and the dynamic boundary condition.

KINEMATIC BOUNDARY CONDITION

The kinematic boundary condition states that the particle at the free surface will follow the free surface. Particles will not 'jump' out of the fluid.

DYNAMIC BOUNDARY CONDITION

The dynamic boundary condition states that the air pressure at the water surface changes only a small bit due to the change in wave height. This change in pressure is neglected and therefore the pressure has to be constant. For inviscous flows such as potential flows, the Bernoulli equation describes the pressure:

$$\frac{\partial \Phi}{\partial t} + \frac{\rho_{air}}{\rho} + \frac{1}{2}(u^2 + v^2 + w^2) + gz = C \quad (B.22)$$

FREE SURFACE BOUNDARY CONDITION

This boundary condition states that the potential at the free surface far away from the floating body is not influenced anymore by the floating body. It will therefore be equal to the incoming wave potential:

$$-\omega^2 \Phi + g \frac{\partial \Phi}{\partial z} = 0 \quad \text{for } z = 0 \quad (B.23)$$

BOTTOM BOUNDARY CONDITION

The boundary at the seabed simply states that no flow will go through the seabed.

$$\frac{\partial \Phi}{\partial n} = 0 \quad \text{at } z = -h \quad (B.24)$$

RADIATION BOUNDARY CONDITION

The waves radiated by the floating body will slowly lose energy as they propagate further away from the body. When radius R of the domain becomes larger the following holds at R:

$$\lim_{R \rightarrow \infty} \Phi = 0, \quad (B.25)$$

NORMAL VELOCITY BOUNDARY CONDITION

The normal velocity boundary condition, also sometimes called the no-leakage condition, states that the velocity of the fluid at the surface of the floating body is equal to the normal velocity of this floating body.

$$\frac{\partial \Phi_i}{\partial n} = n_i \quad (B.26)$$

Applying the free surface, the bottom and the radiation boundary condition to Equation B.21 now simplifies the equation to:

$$\iint_S \left(\Phi_j \cdot \frac{\partial \Phi_k}{\partial n} \right) = \iint_S \left(\Phi_k \cdot \frac{\partial \Phi_j}{\partial n} \right) \quad (B.27)$$

The integral over the total surface S^* reduces to the integral over the surface S, where S is the wetted surface of the hull only. This is only valid for deep water, and Φ_j and Φ_k still have to be evaluated.

B.3.2. LOADS

An important step in using potential theory, to assess the hydrodynamical coefficients of a floating body, is to split up the problem in two separate cases.

- Wave and diffraction forces on a restrained body.
- Waves radiated by an harmonically moving body.

The principle of linearity allows to assess both cases separately. First consider a fixed body and two wave potentials representing the incoming and the diffracted wave; Φ_w and Φ_d . On the surface S the following now has to hold for zero forward speed:

$$\frac{\partial \Phi_n}{\partial n} = \frac{\partial \Phi_w}{\partial n} + \frac{\partial \Phi_d}{\partial n} = 0 \quad (\text{B.28})$$

$$\frac{\partial \Phi_w}{\partial n} = -\frac{\partial \Phi_d}{\partial n} \quad (\text{B.29})$$

The wave forces and moments can now be expressed with:

$$\begin{aligned} X_{w_k} &= -i\rho e^{-i\omega t} \iint_S (\Phi_w + \Phi_d) f_k \cdot dS \\ &= -i\rho e^{-i\omega t} \iint_S (\Phi_w + \Phi_d) \frac{\partial \Phi_k}{\partial n} \cdot dS \quad \text{for: } k = 1, \dots, 6 \end{aligned} \quad (\text{B.30})$$

in which Φ_k is now the radiation potential in direction k . The wave potential is a known function; it is the input for which the hydrodynamic coefficients and the forces are calculated. The diffraction potential still has to be determined. Again using Green's Theorem Equation B.27 we can express the diffraction potential in terms of the radiation potential.

$$\iint_S \left(\Phi_d \cdot \frac{\partial \Phi_k}{\partial n} \right) = \iint_S \left(\Phi_k \cdot \frac{\partial \Phi_d}{\partial n} \right) \quad (\text{B.31})$$

Substituting Equation B.28 into this equation results in:

$$\iint_S \left(\Phi_d \cdot \frac{\partial \Phi_k}{\partial n} \right) = -\iint_S \left(\Phi_k \cdot \frac{\partial \Phi_w}{\partial n} \right) \quad (\text{B.32})$$

Substituting this term into Equation B.30 results in the so called **Haskind relations**:

$$X_{w_k} = -i\rho e^{-i\omega t} \iint_S \left(\Phi_w \frac{\partial \Phi_k}{\partial n} + \Phi_k \frac{\partial \Phi_w}{\partial n} \right) \cdot dS \quad \text{for } k = 1, \dots, 6 \quad (\text{B.33})$$

This relation is of high importance as it states that the wave force depends only on the wave potential and the radiation potential. The diffraction potential is eliminated of the equation. The wave forces can now be determined for each degree of freedom. Now only the radiation potentials have to be evaluated. This is the second step of the method.

If Φ_i is the potential due to a motion of the body in the i_{th} mode, the total radiation potential can be given as:

$$\Phi_r = \sum_{i=1}^6 \Phi_i \quad \text{for all 6 degrees of freedom.} \quad (\text{B.34})$$

The potentials can be imitated by a continuous distribution of single sources on the body surface. These can be imagined as pulsating nodes, influencing the flow at the body surface. All these pulsating nodes combined will represent again a potential. This potential has to satisfy the boundary conditions. If the sources are

known, the potential can be calculated. How these sources influence the flow can be calculated with the use of Green's functions:

$$\Phi_i(x, y, z) = \frac{1}{4\pi} \iint_S \sigma_i(\tilde{x}, \tilde{y}, \tilde{z}) \cdot G(x, y, z, \tilde{x}, \tilde{y}, \tilde{z}) \cdot dS \quad \text{for } i = 1, \dots, 7 \quad (\text{B.35})$$

where:

- $\sigma_i(\tilde{x}, \tilde{y}, \tilde{z})$ represents the source strength in a point $(\tilde{x}, \tilde{y}, \tilde{z})$ on the mean wetted surface due to a motion of the body in the i_{th} mode.
- $G(x, y, z, \tilde{x}, \tilde{y}, \tilde{z})$ is called the Green's function of the pulsating sources on the potential $\Phi_i(x, y, z)$. This function satisfies the Laplace equation and the bottom, free surface and radiation boundary conditions.

The unknown source strengths are determined based on the normal velocity boundary condition. Now that also the radiation potentials are known the added mass and damping can be calculated:

$$a_{ik} = -Re \left\{ \rho \iint_S \Phi_i n_k \cdot dS \right\} \quad (\text{B.36})$$

$$b_{ik} = -Im \left\{ \rho \iint_S \Phi_i n_k \cdot dS \right\} \quad (\text{B.37})$$

Every component of the equations of motion has now been determined. The equations of motion can now be solved for each frequency.

B.4. ANSYS AQWA

The ANSYS Aqwa suite consists of a set of advanced hydrodynamic analysis programs. Depending on the goal of the analysis different programs apply. Aqwa-Line is used to perform calculations in frequency domain. It has the ability to calculate the linear equations of motion of a set of hydrodynamical interacting structures. To do this the frequency dependent added mass and damping are calculated for each structure at each given frequency. Additionally the excitation forces and corresponding phases are calculated for each frequency and each wave direction.

B.4.1. MESHING

Aqwa-line uses a .DAT file as input file. This is simply a text file containing all the locations of the nodes in the mesh, information on how the nodes are connected, structural properties of the system and the wave frequencies and directions for which the motions should be calculated. The proposed way of performing the parametric study is as follows. First the Aqwa environment is used to create a general input file for a configuration with the dimensions: L = 200 m, B = 50 m, T = 15 m and with a distance between the barges of 50 meters. To create an input file of a new configuration this general file will first be read out with Matlab. Next the locations of the nodes will be changed accordingly. For example, if the length of the new configuration is 1.5 times the length of the general configuration, all the x-coordinates of nodes will be multiplied with 1.5. The same applies for the width of the barge and the y-coordinates together with the depth of the barge and the z-coordinates. Finally the structural properties such as the mass and the mass moment of inertia are changed as well. The new input file can now be used as input for Aqwa.

C | Metocean data provided by Shell for the Brent Delta location



Data Source: Northern North Sea Composite Dataset {March 1973 to December 2006}

Significant Wave Height (m)		Wave Period (s)																									Sum	Cumulative Sum		
Lower Bound	Upper Bound	1	2	3	4	5	6	7	8	9	10	11	12	13	14	15	16	17	18	19	20	21	22	23	24	25				
14.5	15.0																											1	1	
14.0	14.5																												1	2
13.5	14.0																												1	3
13.0	13.5																												0	3
12.5	13.0																												2	5
12.0	12.5																												6	11
11.5	12.0																												6	17
11.0	11.5																												15	32
10.5	11.0																												28	58
10.0	10.5																												40	98
9.5	10.0																												58	156
9.0	9.5																												74	200
8.5	9.0																												144	374
8.0	8.5																												198	572
7.5	8.0																												290	862
7.0	7.5																												400	1342
6.5	7.0																												709	2051
6.0	6.5																												1074	3125
5.5	6.0																												1579	4704
5.0	5.5																												2267	6971
4.5	5.0																												3158	10129
4.0	4.5																												4223	14352
3.5	4.0																												5619	19971
3.0	3.5																												7222	27193
2.5	3.0																												9062	36255
2.0	2.5																												10551	46806
1.5	2.0																												12888	59714
1.0	1.5																												11288	70942
0.5	1.0																												4203	74725
0.0	0.5																												152	74877
		0	0	3	50	370	1790	3995	8433	1067	1352	1248	1024	6919	2433	2262	788	530	210	79	43	27	13	4	0	4		3		
		7	7	7	7	7	7	7	7	7	7	7	7	7	7	7	7	7	7	7	7	7	7	7	7	7	7		3	

Table S3 - Hs/Tp Scatter Diagram (All Year)

D | Iron Lady inclining test



Lloyd's Register EMEA

K.P. van der Mandelelaan 41A
3062 MB Rotterdam
P.O. Box 701
3000 AS Rotterdam
The Netherlands

Telephone +31 10 2248 592
Direct line +31 10 2018 411
Fax +31 10 2018 451
Email peter.vankessel@lr.org

www.lr.org

Fax message

To Attn. ZPMC Pieter Schelte Cargo Barge Project Team Fax

Cc Lloyd's Register Attn.Francesco.Ruisi@lr.org Fax Date 14 November 2014

From Alex Perez Page 1 of 1 Your ref e-mail from Mandy Lee

Subject Ship name " PIETER SCHELTE CARGO BARGE ", Yard no. ZPMC1043, IMO no.9665140 Inclining test Our ref RTS/STB/14.1855

Inclining

The inclining test (test carried out on 9th July 2014) report has been examined and found in order for the following particulars:

Lightship weight	24277	tonnes
Longitudinal centre of gravity (LCG)	94.814	meters from AP
Vertical centre of gravity (VCG)	7.123	meters above BL
Transversal centre of gravity (TCG)	-0.004	meters from CL

It is noted that during the test the ship has had excessive items to be deducted. Due attention should be paid to this in the future.

These lightship details are to be used in the final damage calculation and intact stability manual

This document should also be placed in the booklet.

Best regards,


 Alex Pérez
 Specialist
 Statutory Computational Department
 Rotterdam Technical Support Office
 Lloyd's Register EMEA


 Peter Vankessel
 Surveyor in Charge
 Statutory Computational Department
 Rotterdam Technical Support Office
 Lloyd's Register EMEA

E | Influence of topsides accelerations on the loads

E.1. TOPSIDES ACCELERATION FORCES

Additional to the relative pitch the loads in the legs due to the accelerations are calculated. To do so the heave, roll and pitch accelerations of one barge are calculated and translated to topsides accelerations. For the heave motion it is assumed that the accelerations of the barges result in the same accelerations in the topsides. For the roll and pitch motion the rotation of the barge results in an rotational acceleration as well as a translated acceleration in the centre of gravity in the topsides. These combined accelerations result in an overturning moment that is captured by the reaction forces in the legs. A free body diagram sketch of the situation is given in Figure E.1.

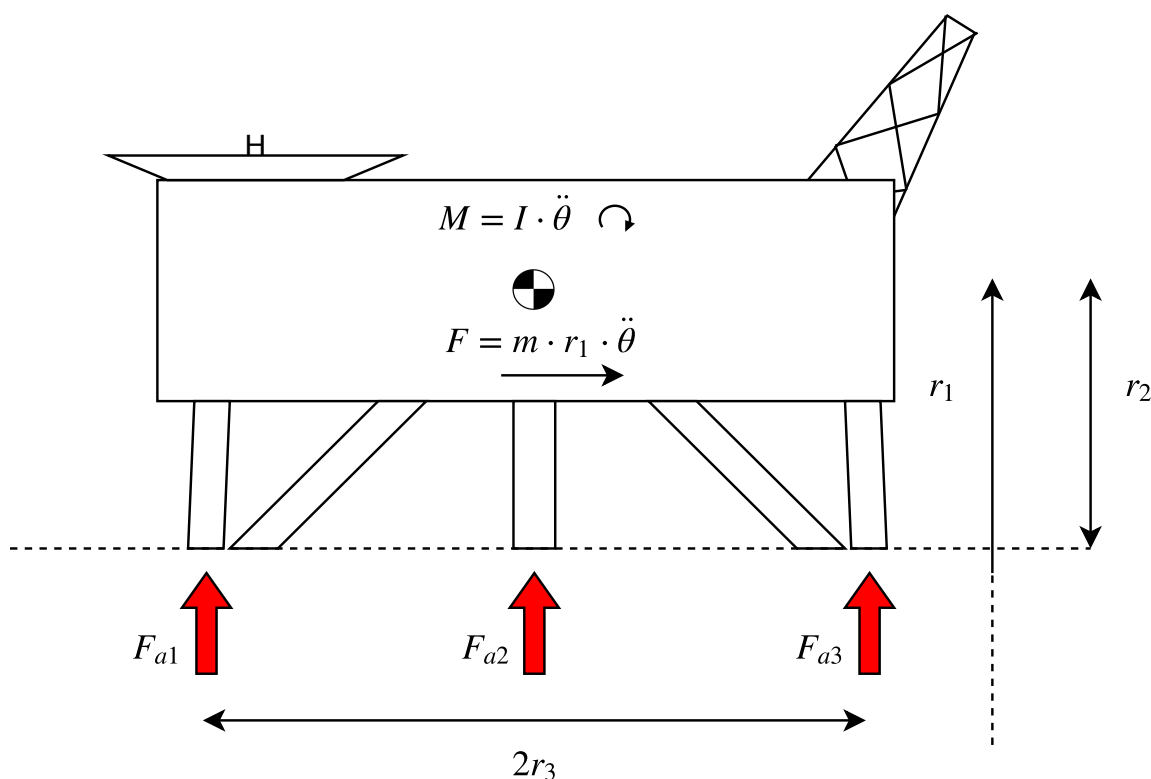


Figure E.1: Schematic side view drawing of the Brent Alpha platform

The figure shows the moment M and force F on the topsides centre of gravity due to the pitch acceleration $\ddot{\theta}$ of the barge. I represents the mass moment of inertia of the topsides, m represents the mass, r_1 represents the distance from the centre of gravity of the topsides to the centre of rotation of the barge. Additionally the vertical forces in legs A1 to A3 are shown. The vertical forces in all six legs for the static situation are given in Table E.1.

Table E.1: Brent Alpha static leg forces due to a opposite vertical displacement of the outside legs of 100mm.

	Portside legs			Starboard legs		
	Vertical leg forces					
	A1	A2	A3	B1	B2	B3
θ_{rel} (°)	(kN)	(kN)	(kN)	(kN)	(kN)	(kN)
0	26.000	30.000	39.000	23.000	31.000	27.000
0.38	56.000	28.000	11.000	-7.000	33.000	55.000

It can be seen that due to the relative pitch angle θ_{rel} a force of approximately 30.000 kN is added or subtracted from the corner legs, depending on the direction of the force. The force in the middle legs remains approximately the same.

The additional force in the legs due to the accelerations can be calculated by solving the moment equation of the moment around the A2 leg.

$$\sum M = (F_{a1} - F_{a3}) \cdot r_3 + (m \cdot r_1 r_2 + I) \cdot \ddot{\theta} = 0 \quad (E.1)$$

Additionally the vertical force balance should be satisfied. The vertical forces in the legs have to equal the weight of the topsides.

$$\sum F = F_{a1} + F_{a2} + F_{a3} - F_{a1-static} - F_{a2-static} - F_{a3-static} = 0 \quad (E.2)$$

By assuming that F_{a2} remains the same as in the static situation the additional force in the legs due to the accelerations can be calculated. This exercise can be repeated for the B-side legs. Additionally the same calculation can be performed for the roll motion. It has to be taken in mind that the roll motion of the vessel and the roll motion of the topsides are not one on one related as is the case for the pitch motion.

Table E.2 shows the vertical forces in the corner legs due to accelerations for different incoming wave angles with a significant wave height of 1m. Additionally the leg forces are given as a percentage of the leg force due to the relative pitch angle of 0.38°. It can be seen that this portion of the force is very small and thus it can be said that the accelerations do not have a significant influence on the limiting load case. The relative pitch itself, but also the impact velocity and connection forces, will result in the exceeding of a limit much sooner. Still, an extra safety factor of around 5 % to take into account the accelerations might be applied.

Table E.2: Brent Alpha leg forces due to accelerations for different incoming wave angles with $H_s = 1m$ and $T_p = 9s$.

	Portside legs				Starboard legs			
	Vertical leg forces							
	A1	A1	A3	A3	B1	B1	B3	B3
α (°)	(kN)	(%)	(kN)	(%)	(kN)	(%)	(kN)	(%)
90	560	2.05	860	2.19	590	2.52	680	2.42
120	140	0.45	200	0.51	140	0.58	150	0.56
150	75	0.29	120	0.31	75	0.32	90	0.34
180	25	0.05	30	0.08	20	0.06	20	0.07

